Title
Graphene-Plasmonic Hybrid Platform for Label-Free SERS Biomedical Detection

Author
Wang, Pu

Publication Date
2015

UNIVERSITY OF CALIFORNIA

Los Angeles

Graphene-Plasmonic Hybrid Platform for Label-Free SERS Biomedical Detection

A dissertation submitted in partial satisfaction of the
requirements for the degree Doctor of Philosophy
in Materials Science and Engineering

by

Pu Wang

2015

ABSTRACT OF THE DISSERTATION

Graphene-Plasmonic Hybrid Platform for Label-Free SERS Biomedical Detection

By

Pu Wang

Doctor of Philosophy in Materials Science and Engineering
University of California, Los Angeles, 2015
Professor Ya-Hong Xie, Chair

Surface Enhanced Raman Scattering (SERS) has attracted explosive interest for the wealth of vibrational information it provides with minimal invasive effects to target analyte. Nanotechnology, especially in the form of noble metal nanoparticles exhibit unique electromagnetic and chemical characteristics that are explored to realize ultra-sensitive SERS detection in chemical and biological analysis. Graphene, atom-thick carbon monolayer, exhibits superior chemical stability and bio-compatibility. A combination of SERS-active metal nanostructures and graphene will create various synergies in SERS.

The main objective of this research was to exploit the applications of the graphene-Au tip hybrid platform in SERS. The hybrid platform consists of a periodic Au nano-pyramid substrate to provide reproducible plasmonic enhancement, and the superimposed monolayer graphene sheet, serving as “built-in” Raman marker.

Extensive theoretical and experimental studies were conducted to determine the potentials of the hybrid platform as SERS substrate. Results from both Finite-Domain Time-Domain (FDTD) numerical simulation and Raman scattering of graphene suggested that the hybrid platform boosted a high density of hotspots yielding 1000 times SERS enhancement of graphene bands.

Ultra-high sensitivity of the hybrid platform was demonstrated by bio-molecules including dye, protein and neurotransmitters. Dopamine and serotonin can be detected and distinguished at 10^{-9} M concentration in the presence of human body fluid. Single molecule detection was obtained using a bi-analyte technique. Graphene supported a vibration mode dependent SERS chemical enhancement of ~10 to the analyte.

Quantitative evaluation of hotspots was presented using spatially resolved Raman mapping of graphene SERS enhancement. Graphene plays a crucial role in quantifying SERS hotspots and paves the path for defining SERS EF that could be universally applied to various SERS systems. A reproducible and statistically reliable SERS quantification approach using the hybrid platform was proposed. The SERS mapping based approach not only leverages the ultra-sensitivity but also minimizes the spot-to-spot variations.

Feasibility of biomedical diagnosis with the hybrid platform was exploited by colon cancer cell sensing and time-dependent SERS of amyloid β protein monomer. The capabilities of the platform are demonstrated by colon cancer cell detection in simulated body fluid background with cell concentration down to 50 cells /mL. Sensitivity of 95% was evidenced by Principle Components Analysis (PCA). Besides, a noticeable

evolution profile of the Aβ SERS peaks was observed and attributed to the Aβ configurational change. Taken together, the results suggested the graphene-plasmonic hybrid platform can potentially deliver a biomedical detection and diagnostic imaging platform with superior sensitivity and resolution.

The dissertation of Pu Wang is approved.

Brian C. Regan

Mark S. Goorsky

Ya-Hong Xie, Committee Chair

University of California, Los Angeles

2015

To mom and dad, who supported me
throughout this incredible journey, and without
whom it would not have been possible.

Contents

List of Tables

List of Figures

List of Abbreviations

SERS	Surface Enhanced Raman Scattering
SM-SERS	Single Molecule Surface Enhanced Raman Scattering
BiASERS	Bi-Analyte method for Surface Enhanced Raman Scattering
SERS EF	Surface Enhanced Raman Scattering Enhancement Factor
GERS	Graphene Enhanced Raman Scattering
NP	Nanoparticle
MNP	Metallic Nanoparticle
AuNP	Gold Nanoparticle
AgNP	Silver Nanoparticle
SP	Surface Plasmon
LSP	Localized Surface Plasmon
FDTD	Finite Domain Time Domain
PML	Perfectly Matched Layers
FWHM	Full-Width Half-Maximum
PMMA	Poly(methyl methacrylate)
KOH	Potassium hydroxide
$FeCl_3$	Iron(III) chloride
PCA	Principle Component Analysis
BAM	Brain Activity Mapping
Aβ	Amyloid beta protein
SBF	Simulated Body Fluid

Acknowledgments

First and foremost, I acknowledge and thank my advisor Dr. Ya-Hong Xie, without whom none of the accomplishments documented in this dissertation would have been possible. Working with Dr. Xie was truly a life-changing experience, which helped me to understand and appreciate what it takes to be a real scientist, and more importantly, to be a respectable and integrate person. I would like extend my gratitude for his support, enthusiasm and inspiring guidance. Through his mentorship, I have polished my skill set, and learned the proper scientific diligence and solid work ethic required for rigorous scientific research. Being Dr. Xie's student is one of the best things ever happened to me and words fail to express how lucky I have him as my mentor.

Additionally, I would like to thank Dr. Thomas Schroeder for his selfless and superb mentorship during my stay in IHP, Germany. I am grateful to Dr. Huinan Liu from UC Riverside, Dr. Istvan Mody and Dr. David Teplow, who are amazing collaborators to introduce us into the biomedical world.

I am grateful to my fellow graduate students in Xie Lab. I have to credit Ming Xia and Wei Zhang for providing me with samples. I am grateful to Owen Liang for coordinating me with optical measurement. I also have to mention Fan Yang, a very talented summer intern undergraduate from Physics School of Peking University, who

did a great job in PCA coding and did me a great favor. I felt privileged to work and interact with them in this innovative laboratory on a daily basis.

On a personal note, I would like to express my most sincere gratitude to my family whose love, sacrifice and dedication are the biggest reasons behind all my success. They will always be a source of great inspiration in my life. I will always keep to my heart my father’s advice. I would like to express my gratitude for my mother who has given me the strength to be myself. I would like to extend my deepest thanks to my best friends, Xuan Sun and Manqing Cao, amazing Aries people with great personalities, who have supported me through the period of my life and have given me the strength to carry on despite the challenges I faced.

I gratefully acknowledge funding from Function Accelerated nanoMaterial Engineering (FAME). I thank German Academic Exchange Service (DAAD) RISE fellowship that sponsored my stay in Germany, 2012. I would also like to express my deepest gratitude to China Scholarship Council for bestowing the Chinese Government Award for Outstanding Self-financed Student Abroad upon me.

VITA

2010	B.S. in Physics Peking University, Beijing, China
2012	M.S. in Materials Science and Engineering University of California at Los Angeles
2015	Ph.D. Candidate in Materials Science and Engineering University of California at Los Angeles

1

Introduction

1.1 Motivation and Innovation of Thesis

There has been a burgeoning interest in surface-enhanced Raman scattering (SERS) ever since its discovery 40 years ago [1]. The application of SERS *via* plasmonic nanostructures spans analytical chemistry, materials science to biological sensing and imaging [2-7]. Various metallic nanostructures with tunable plasmonic properties have been widely explored as excellent SERS active systems [8-14]. In spite of the tremendous boost in new SERS-active platforms and their applications reported in the literature [5], the SERS mechanisms are still under debated and few SERS based techniques have paved their way to clinical world [15-16].

In 2004, graphene, the very first two-dimensional (2D) carbon atomic crystal was discovered [17]. The extraordinary properties [18-20] and the 2D nature offer exciting opportunities for the development of a novel SERS system that could overcome the drawbacks of the traditional metallic nanostructure systems.

A combination of SERS-active metal nanostructures and bio-compatible monolayer graphene creates various synergies. The main thrust of this dissertation is to build upon graphene-plasmonic hybrid system to present a new system for investigation of SERS mechanisms; demonstrate a general platform for ultra-sensitive bio-molecular SERS detection; develop novel proof-of-principle technologies for biological diagnosis involving neurotransmitters, proteins and cells. Several novel and significant approaches and results will be presented in this work:

Graphene-Au tip Hybrid Platform: The platform has favorable characteristics such as chemical stability, reproducibility and ease for functionalization as well. The significant sensitivity of the platform is demonstrated both theoretically and experimentally.

Ultra-Sensitive Biomolecular detection: Single molecule level detection via bi-analyte SERS is demonstrated using the hybrid platform. We overcome the inherent spot-to-spot variations observed in conventional SERS systems and show statistically reproducible signal response at below picomolar concentration regime.

Reproducible SERS Quantification: Graphene plays a key role in the hybrid platform to not only precisely describe SERS hotspots distribution and localized enhancement, but also quantify the anaylte concentration in a statistically reliable way via Raman mapping. The integration of graphene into SERS systems will benefit research on SERS mechanisms, and may also lead to the development of SERS based technique for bioanalytical applications.

SERS Monitoring: The hybrid platform has been utilized in essential biological entities including neurotransmitters, disease-associated protein, and cancer cells. The potentials for monitoring configurational and compositional change at molecular level are shown, which opens up exciting opportunities for further exploitation of SERS.

Through the advances highlighted above, this thesis work establishes a solid foundation for realizing a novel graphene-Au nano-pyramid SERS platform that meet challenges not attainable with currently available SERS platforms.

This chapter introduces background on SERS in Chapter 1.2 and graphene in Chapter 1.3 that is required for appreciation of the research presented in this dissertation. Chapter 1.4 presents the outline of the dissertation.

1.2 Surface Enhanced Raman Spectroscopy (SERS)

Raman spectroscopy [21] is a valuable tool in many research fields. The technique extracts detailed vibrational information and provides unique Raman fingerprints from all kinds of samples. The ease to acquire Raman measurements, little need for sample preparation, non-destructive nature and minimal waste make Raman an attractive analytical technique. However, Raman signals are inherently weak [22] and therefore prohibit the investigation of substances in low concentrations. The challenge originates from the extremely small cross section of inelastic scattering event. In 1974 Fleischmann et al. [1] observed enhanced Raman signal of pyridine absorbed on rough silver surface and discovered SERS. This phenomenon has given Raman a tremendous boost in attention. Metal nanostructures are ideal SERS platforms due to the formation of hotspots, which are very small regions (usually nano-gaps) where local electromagnetic field are highly enhanced [23]. When target species are located in the vicinity of hotspots their Raman signals are significantly amplified. The local SERS enhancement at hotspots exceeds 10^{10} and thus makes the detection of a single molecule possible [6].

The ultra-high sensitivity demonstrated by single molecule surface-enhanced Raman scattering (SM-SERS) [24-25] elevated SERS to the very restrict group of analytical techniques capable of reaching ultimate detection limit [26]. One advantage that separates SERS from other single-molecule techniques such as fluorescence spectroscopy [27] is that Raman signals contain unique vibrational information from the analyte of interest and thus allow for much higher specificity in structure and configuration.

1.2.1 Nanotechnology for SERS

Gold, silver and copper support surface-plasmons excitation in the visible region and their nanostructures are verified to be effective SERS platforms [28]. Metallic nanostructure based SERS systems are designed such that the nano-features concentrate incident electromagnetic energy to yield a plasmonic response for either direct (label-free) sensing or indirect sensing [29-31]. The excitation of surface-plasmons contributes to enhancement in the localized EM field around the metallic nano-features [32] and thus surface-enhances both the excitation light and scattered radiation.

Research focus on SERS-active metallic nano-structrues is justified by the wide opportunities in optimizing nano-structrues to maximize the SERS output [33], since the enhancement is largely dependent on parameters like size, shape, and arrangements of nano-features. SERS-active platforms can be arbitrarily divided in two categories: (1) Metallic nanoparticles (MNPs) [34-36]; (2) Nano-structure arrays fabricated on solid substrates by lithography or template synthesis [37-39].

Synthesis strategies of MNPs have been exhaustively investigated with many well established techniques [40]. One easiest way to achieve SERS is using MNPs in suspension in the presence of analyte in a certain concentration. Another approach includes immobilizing MNPs on planar substrates as SERS platforms. The nano-gaps between MNPs when they aggregate in the solution serve as SERS hotspots where analyte molecules are trapped [41]. Au and Ag nanoparticles (NPs) [23, 38] are most widely used due to high SERS enhancement. In spite of good SERS performance and ease to use, reproducibility and sampling issues remain to be challenge.

Tunable nano-structrue morphology is required for SERS to reach a new level of applicability. Many SERS substrates are also developed by template, nanolithography and other techniques [42-44]. Such techniques allow for fine control over the size, shape and arrangement of the nano-features. Numerical simulations are often used for SERS substrate design [45, 46]. The control over geometric parameters opens up possibilities for creating SERS substrates with high reproducibility in SERS intensities. Periodic nano-structures and micro-arrays of MNPs have been prepared using electron beam lithography (EBL) and focused ion beam (FIB) techniques [47, 48]. Moreover, the use of template directed synthesis allows mass production of SERS substrates.

Though much efforts have been spent on improvement of techniques to fabricate nano-structured substrates in recent 20 years, there are still arguments that they are at rather rudimentary stages and techniques to produce highly reproducible substrates at relatively low cost are expected to come. The increasingly deepened understanding of SERS mechanisms, allied with the great advances in nano-fabrication as well as other synthetic techniques for metallic nano-structrue preparation, will facilitate the applications of SERS to a larger extent.

1.2.2 SERS Platforms for Biological Detection

Researchers have focused on the exploration of promising analytical applications of SERS for over 30 years and currently SERS has extensively been used in biomedical and environmental areas [49-5]. There are two main streams of SERS as an analytical tool in biological related research: (1) Fundamental research focuses on the structural, conformational and charge transfer properties of biomolecules [54]. SERS of various proteins [55-57] has been investigated to generate insights in the influence of complex structure, molecular orientations and charge transfer process; (2) Applied research focused on target detection (e.g. protein, DNA) [58] and biomedical diagnostics (e.g. cancer diagnostic) [59-61]. The super high sensitivity of SERS enables single molecule detection.

In typical SERS active systems using metallic nano-particles, these hot spots are sparse and randomly distributed, leading to the rarity of coincidence of molecules and hotspots in highly diluted solutions. Only a very small fraction of the molecules ends up within nanometers range to individual hot spots as is required for producing measurable

Raman signals. Successful detection of molecules is at the expense of long time of up to hours spent on searching for measurable signals making the technique prohibitive for practical applications, especially real-time measurements. The commonly used metallic nanoparticles suffer from the shortcomings of easy degradation, limited bio-compatibility and poor reproducibility. One of the labeling processes is typically introduced by covalently attaching extrinsic Raman labels to nanoparticles. The signals detected are from SERS probes *via* biomolecule-ligand recognition instead of biomolecules themselves. The label-based indirect SERS method suffers from false positive issue as well as synthetic challenges. In most cases of biomolecule SERS detection, a labelling process is needed. The SERS probe consists of MNPs hosting a molecule for spectroscopic signature. The MNPs are conjugated with recognition ligands to achieve molecular specificity. The MNPs are labelled with dye molecules that yield strong SERS signals which are referred as Raman reporter or SERS probe. SERS involving labelling process is referred as indirect SERS since the detected signals are from Raman reporter molecules instead of target analyte. Introducing SERS labels largely expands the application of SERS in biomolecules especially those that are relatively Raman inactive. Those dye molecules that are commonly used as Raman reporter are highly Raman active and generate very strong SERS feedback. SERS processes with signals from analyte directly without Raman reporter molecule involved are referred to as label-free SERS. Label-free SERS enables extraction of SERS signals directly from target analyte molecules and reveals more information.

1.2.3 SERS Quantification

One biggest challenge that prevents SERS from widespread applications is the poor capability to achieve precise quantitative understanding mainly due to the controversial SERS mechanism. Although various SERS systems have been successfully developed, SERS based quantification remains to be problematic.

The SERS enhancement factor is subdivided into two components originated from electromagnetic mechanism (EM) [62,63] and chemical mechanism (CM) [64,65] separately. EM accounts for majority of the contribution by surface plasmonic enhancement while CM makes additional 10-100 times enhancement induced by the charge transfer process [66] from interaction between analyte molecule and SERS surface. The technical difficulties in separating CM enhancement from EM enhancement prevent researchers from building relationships between the SERS signal and the number of analyte molecules in detected regime, and further quantifying the analyte concentration in a reliable way.

Current quantification method is based on SERS internal reference, a Raman molecule attached to the nanoparticle to provide stable SERS response [67,68]. However, the random arrangement of SERS reference molecules and stability under measurement is one of the obstacles to SERS quantification. SERS is a complex process whose mechanisms are still under debate. Heterogeneity of the SERS active substrates leads to significant variation in the SERS peak. The degree of aggregation, instrumental factors as well as interaction between plasmonic structure and molecules also affect the SERS signals [69-71]. Consequently SERS quantification using conventional SERS systems suffer from short quantification range, poor reproducibility, serious spot-to-spot variation, and lack of universal adaptability.

1.3 Graphene

1.3.1 Unique Characteristics of Graphene

Graphene, a novel two-dimensional monolayer of sp^2-bonded carbon atoms, has shown great potentials in many fields and attracted tremendous attention owing to its unique electronic [72], optical [73,74], mechanical [75] and thermal [76-78] properties. The sp^2 hybridized carbon bonds lead to the extremely strong in-plane σ bond and the out-of-plane π bond. The π bond contributes to a delocalized network of electrons, which in graphene behave like massless 2D particles [19].

Intensive researches have revealed the fascinating properties of graphene including high specific surface area of 2630 m^2/g, mechanical strength (breaking strength ~42 N m^{-1} and Young's modulus ~1100GPa), thermal conductivity around 5000 W mK^{-1} at room temperature), high optical transparency (only ~2.3% absorption towards visible lights) together with exceptional electronic conductivity (room temperature charge carrier mobility of ~10,000 cm^{-2} s^{-1}) [79-81]. Besides, the intrinsic bio-compatible carbon surface, relatively low cost and scalable production, possibility of chemical and biological functionalization also make graphene and its derivatives ideal candidates for bio-applications [82,83].

Applications of graphene are initially driven by progress in scalable high-quality graphene production [84,85]. Multiple methods have been well developed to synthesize graphene for various purposes. The major methods are the followings: (1) Liquid phase exfoliation of graphite [86], which is based on splitting graphite into individual monolayer flakes using sonication and prolonged treatment. Liquid phase exfoliated graphene is used for energy storage, composites synthesis and drug carriers [87,88]; (2) Chemical vapor deposition (CVD) on copper foils [89], which is used to produce large-area uniform single layer graphene that can be transferred to arbitrary substrates. CVD graphene has been widely applied as transparent coating or conductive layer [90,91] for electronic and photonic applications; (3) Direct synthesis of high-quality graphene on SiC via high temperature annealing [92]. SiC grown graphene allows for high-frequency transistors and other electronic devices [93,94].

Applications of graphene in high-performance electronics are limited since graphene has no bandgap. At the same time lack of techniques to realize scalable production of high-quality graphene and efficient transfer process. Currently graphene holds promise in flexible electronics consisting of organic light-emitting diode (OLED) [95], electronic paper [96] and touch screen [97] as transparent conductive coating. Graphene has characteristics fit for controllable photonics [98]. Graphene based photodetectors [99-102] have potentially higher detecting spectral width and operating bandwidth than state-of-art photodetectors. Graphene’s role in energy generation and storage has also been extensively studied with solar cells, lithium-ion batteries and super-capacitors [103-105].

Beyond the well-studied electronic and optoelectronic applications of graphene, the biomedical applications of graphene [106,107] is a relatively new area with tremendous potential. Liu et al. reported the use of graphene oxide (GO) nanosheets as efficient carrier for drug delivery [108]. Antibody-conjugated nanographene could be specifically directed to tumor vasculature for *in vivo* imaging [109,110]. Chemically modified and functionalized graphene is promising in fast and sensitive devices to detect various biological species.

1.3.2 Raman Spectroscopy of Graphene

The discovery of graphene completes the carbon family. The 2D graphene serves as building block for carbon allotropes including zero-dimensional fullerene, 1D carbon nanotubes and 3D graphite. Raman spectroscopy is the ideal technique to identify carbon-based materials [111] in a fast and non-destructive fashion with maximum structural and electronic information provided. Raman spectroscopy has been a standard practice in graphene research since it can provide structural reference that could be used by different research groups to compare with.

The graphene Raman spectrum shows only a few prominent features, whose shape, intensity and position give information on structure, strain, defect, and electronic status [112]. The delocalized π electrons in graphene are the main reason why Raman spectroscopy in graphene is always resonant [113]. The two major features commonly existed for graphene at visible excitation Raman spectra are the so-called G and 2D peaks, which locate around 1580 cm^{-1} and 2700 cm^{-1} (incident laser wavelength 514 nm) separately [114]. The 2D peak is historically named G’ since it’s the second most prominent peak observed in graphite samples. The 2D peak is the overtone, or the second order of D peak. The D peak is assigned to the breathing modes of six-atom rings but it requires defects to be active [115-117]. D peak is accompanied with a D' peak when double resonance happens. There is a significant difference between the 2D peak of graphene and graphite. The Raman spectra of graphene only present peaks assigned to in-plane vibrations due to the monolayer nature, thus only have a single sharp 2D peak with much higher intensity than G peak. While for graphite the 2D peak actually consists a set of peaks also assigned to inter-layer shear modes and layer-breathing modes. Such modes scales with the number of graphene layers, thus make Raman of single layer graphene easily distinguishable from few layer graphene.

1.4 Outline of Thesis

The remainder of this thesis is divided into 5 chapters, which guide the reader through the flow of the research conducted over the author's Ph.D. career. As concisely summarized above, the first chapter discusses the context of the complex field of SERS and graphene which emerges as a promising building block of SERS platforms.

Chapter 2 describes the synthesis and characterization of the graphene-Au tip hybrid platform. The template based technique capable of synthesizing the Au tip substrate reproducibly is presented. Such technique has advantages in terms of large-scale production and freedom of tuning parameters of the Au tips. The CVD synthesis of monolayer graphene and PMMA transfer technique is presented. With the monolayer graphene integrated, the hybrid platform has better bio-compatibility and chemical inertness compared with metallic nanostructures.

Chapter 3 presents an investigation of theoretical simulation featuring three-dimensional finite difference time domain (FDTD). The study employs simulation of both near-field and far-field characteristics of the periodic Au tip substrate. The substrate was then modeled numerically to unravel plasmonic tunability of the substrate and the hotspot distribution in the visible region.

Chapter 4 describes the characterization of the hybrid platform using Raman spectroscopy. The first study discusses the SERS of graphene. The graphene Raman enhancement of up to 10^7 results from the cooperative plasmonic resonance of graphene and the Au tip surface. In addition, a rather prominent D-band appeared at localized hot spots from graphene on Au tipped surfaces that is nearly absent from the exactly same piece of graphene on the immediately adjacent flat Au surface indicates a new origin of D band from 1-D graphene folds. The second study presents experimental demonstration on plasmonic nature of the hybrid platform, which is in good agreement with the simulation presented in Chapter 3.

Chapter 5 details the ultra-high sensitivity of the hybrid platform in bio-molecule sensing. The single molecule detection capability of the platform is demonstrated using a bi-analyte SERS technique. The addition of graphene enables determination of chemical enhancement factor separately from electromagnetic enhancement factor. Graphene also serves as built-in hotspot markers to support quantifiable and reproducible SERS signal.

Chapter 6 describes the application of the graphene-plasmonic hybrid platform to realize SERS quantification. The statistically reliable SERS quantification using the hybrid platform not only leverages the ultra-sensitivity but also minimizes the spot-to-spot variations. Graphene plays a crucial role in quantifying SERS hotspots and paves the path for defining SERS EF that could be universally applied to various SERS systems.

Chapter 7 features the novel studies on the hybrid SERS platform, both studies on SERS quantification and biological diagnosis applications. The hybrid platform enables: first, detection of neurotransmitters, dopamine and serotonin, at nanomolar concentration with simulated body fluid background; second, monitoring configurational change of amyloid β 1-40 from monomer to β sheet; third, diagnosis of colon cancer cell at highly diluted solutions. The successful applications indicate that the hybrid platform holds great potentials in clinical transformation.

Chapter 8 concludes this thesis by providing the major results and contributions to the field together with a section that proposes future work that can build on the results presented herein.

2

Synthesis of Graphene-Au Tip SERS Hybrid Platform

2.1 Introduction

The graphene-Au tip hybrid platform consists of a periodically arranged Au nano-pyramid (referred to as tip) substrate and large-area single layer graphene superimposed on the tipped surface. The periodic Au tip structure with tunable size and sharpness can be fabricated by a wafer-scale bottom-up templating technology [119]. Periodic inverted silicon pyramidal pits, which are templated from non-close-packed monolayer colloidal polystyrene nanoparticles (PS spheres), are prepared by a simple spin-coating technology. The Si substrates with inverted pyramidal pits are employed as reusable structural templates to replicate arrays of gold nano-pyramids with nanoscale sharp apex. The specific fabrication approach of the Au nano-pyramids is amenable to engineering the SERS hotspots in terms of their density and location *via* lithography.

Large-area monolayer graphene has been achieved on copper foils by CVD [89]. This technique is in principle capable of mass production of graphene [94]. The commonly used poly(methylmethacrylate) (PMMA) based transfer technique [120] enables transfer of graphene from Cu films to arbitrary substrates and avoids transferred graphene to be broken into pieces. Various water-free and clean transfer techniques [121-129] were developed in recent years to minimize the detrimental effects on electronic properties of graphene during transfer. In this study monolayer CVD graphene is transferred to cover the Au tip surface using the PMMA method due to the fact that yield of direct transfer techniques is very low.

The hybrid platform combines the advantages of periodic Au tip substrate and graphene. The periodic Au tip substrate boosts strong plasmonic enhancement. The monolayer graphene not only serves as bio-compatible transparent coating, but opens up opportunities for surface functionalization. Graphene coating could protect refined metals from reactive environments. Graphene coating on Cu increases the resistance of metal to oxidation [130] and electrochemical degradation [131]. The wettability of graphene-coated surface could be tuned by modifying graphene [132,133]. The superior bio-compatibility of graphene is proved by the evidence that cell can directly survive on CVD graphene without any glial layer [134].

In this chapter, the detailed process flow of the sample preparation is presented together with experimental conditions. Chapter 2.2 briefly discusses the Au tip substrate fabrication, CVD graphene growth and transfer of graphene respectively. Chapter 2.3 presents the characterization of the hybrid platform by scanning electron microscope.

2.2 Experiment Procedures

2.2.1 Fabrication of Au Nano-pyramid Arrays

The periodic Au tip substrate, which is the critical contributor to the high local electromagnetic field enhancement, is fabricated using a template based technique that enables fabrication of nano-features fat beyond photolithography limit. The detailed fabrication process could be referred to from [135,136].

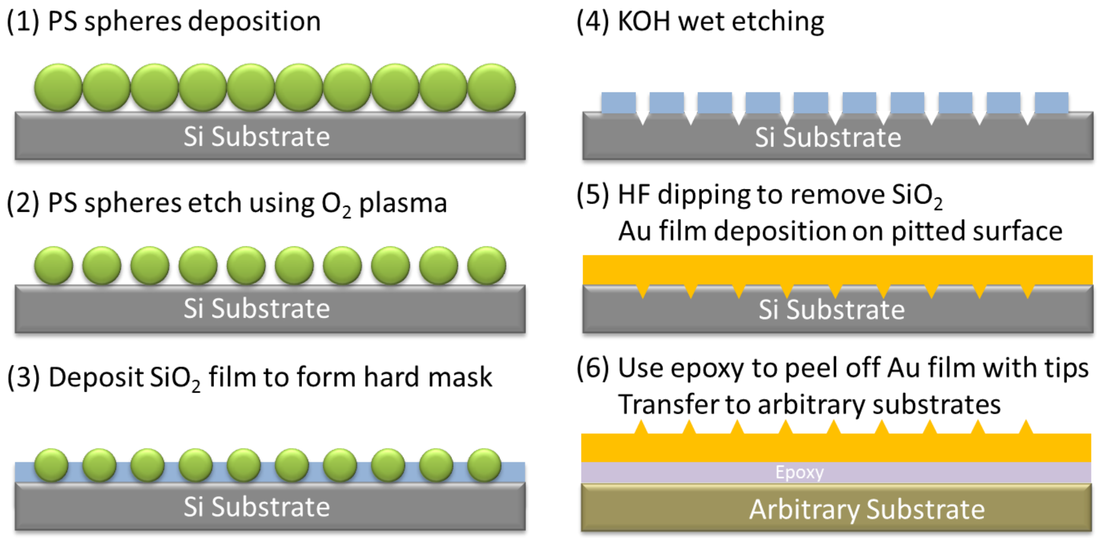

Figure 2.1: Process flow of the periodic Au tip substrate.

As shown in **Figure 2.1**, the fabrication process starts with polystyrene (PS) sphere self-assembly patterning on Si (100) surface, which is the origin of hexagonal periodicity. Size of PS spheres could range from sub-100 nm to over 500 nm. . Similar patterns of smaller pitch with size down to 20 nm can be produced using self-assembly of diblock copolymer. O_2 plasma etches the PS spheres to shrink their size. Then a thin layer of SiO_2 is deposited over the surface as hard mask for the following KOH etching. KOH etches Si anisotropically with etching rate of single crystal Si along <100> two orders higher than that along <111> direction. After etching each pit has an inverted pyramidal shape with an atomically sharp apex at the bottom of four (111) facets. Both the size and separation of the pit can be controlled by tuning the PS sphere size, O_2 plasma etching duration, or KOH wet etching duration. **Figure 2.2a** shows the plan-view SEM image of the hexagonally arranged nano-pit array on the template surface. Each pit shows a square-shape boundary. The substrates commonly used in this study have a pit size of ~200 nm and 200 nm separation.

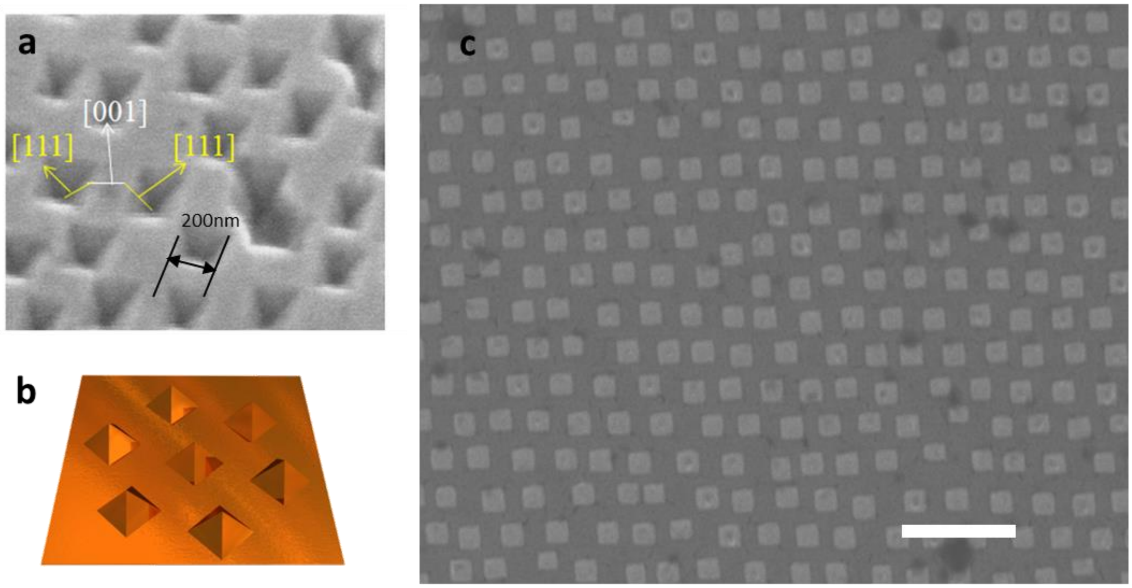

Figure 2.2: (a), SEM of the inverted pyramidal shape pit on the Si substrate. Each pit has a size of 200 nm. **(b),** Illustration of the hexagonally arranged Au tip substrate. **(c),** Top view of the Au hexagonally arranged Au tip substrate. Scale bar 1μm.

200 nm thick Au films are deposited over the pitted surface, bond to a handle substrate using epoxy, and then lifted off of the surface thereby completing the nano-casting process. SEM image of the Au nanopyramids demonstrates the 6-fold symmetry preserved from the self-organized PS sphere pattern. The identical shape, the precise orientation, and the non-negligible variation in Au pyramids are clearly visible from **Figure 2.2c**. Once a template is prepared it can be reused for multiple times to produce uniform Au tip substrates of desired area.

2.2.2 Growth and Transfer of CVD Single Layer Graphene

CVD has been widely used to synthesize mono- and few- layer graphene sheets on metal surfaces like Ni and Cu by surface segregation of carbon atoms from hydrocarbon decomposition [137,138]. Few-layer graphene sheets were grown on Ni films using CVD of methane by controlling the cool-down rate to suppress carbon precipitation. While in the case of Cu, graphene growth terminated once the Cu surface was fully covered [139]. Aside from rather low solubility of C in Cu, the surface-mediated process and the self-limiting nature contribute to >95% coverage of monolayer graphene on Cu foils [140]. Continuous single-crystal graphene free of broken carbon bonds and disorders covers the substrate for even wafer-scale [141].

25 micron-thick copper foil from Alfa Aesar (#13382) is cut into a 2x2 inch square. The copper foil is loaded onto the center of a quartz CVD chamber, the furnace is heated up to ~1025 ℃ under the flow of H_2 (~1000 sccm). After 30 minute annealing, the CVD growth was carried out with 20 Torr total pressure with CH_4 (~20 sccm) and H_2 (~1000 sccm) for 15 minutes. Then the chamber was cooled down to room temperature.

Poly(methylmethacrylate) (PMMA) is utilized for graphene transfer. A ~500 nm-thick PMMA layer was uniformly spin coated on the synthesized graphene sample. The metal catalyst Cu was removed in an etching solution of $FeCl_3$: H_2O (1:5 vol.%). Then the floating PMMA-graphene structure was transferred onto the surface of de-ionized water. Subsequently the sample was transferred onto a target substrate and left to dry. Finally the PMMA supporting layer was removed by acetone. Advanced transfer approaches [123,124] can be employed to improve the quality of transferred graphene and prevent cracks and tears.

Raman spectroscopy is applied to test the quality of as-grown graphene. Graphene generates strong Raman signal when transferred on 300 nm SiO_2 /Si substrate with excitation laser wavelength 514 nm. As shown in **Figure 2.3a**, Raman spectrum of high-quality CVD graphene shows high 2D to G peak intensity ratio, which is often linked to the monolayer nature, and barely existing D band, whose absence indicates the graphene free of defects. It can also be confirmed as single layer graphene by color contrast of optical microscope and Raman spectroscopy [142]. **Figure 2.3b** shows the optical microscope image of PMMA transferred graphene on the 300 nm SiO_2/Si substrate. The residuals from transparent PMMA and $FeCl_3$ solution lead to detrimental influences on electronic properties of graphene. However, in this study graphene plays the role of transparent coating thus the PMMA transfer method is fair enough in terms of quality. The relatively low light absorption of monolayer graphene (constant absorption of 2.3% for infrared and visible light) makes it a superior transparent coating in visible range.

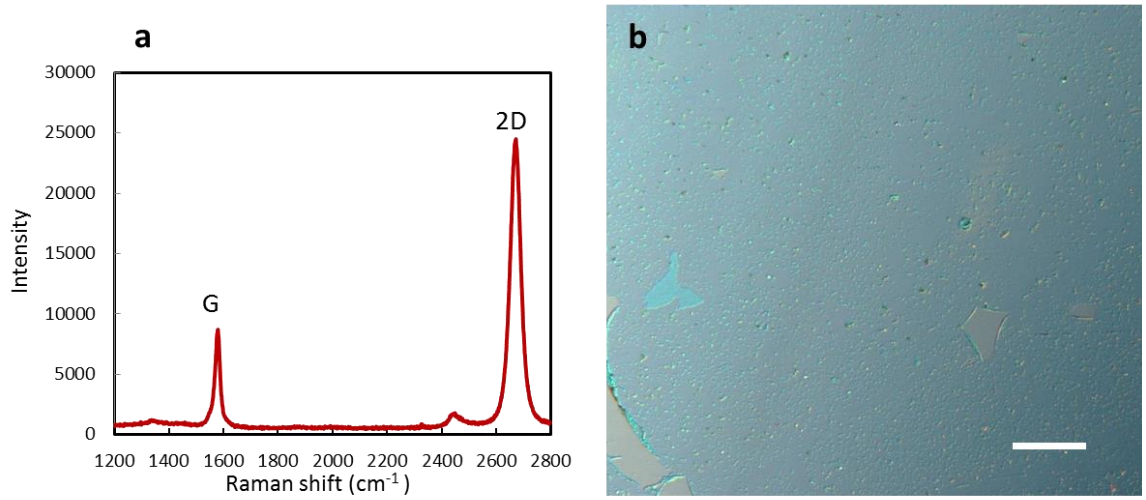

Figure 2.3: (a), Raman spectrum and **(b),** Optical microscope image of CVD monolayer graphene transferred onto 300 nm SiO_2 /Si substrate. Scale bar 50 μm

2.3 Results and discussion

The hybrid platform is fabricated by superimposing monolayer graphene on the Au tip substrates. As illustrated in **Figure 2.4a**, uniform monolayer graphene is grown on Cu foil using CVD and subsequently transferred to the Au tip substrate by PMMA. **Figure 2.4b** shows the plan-view scanning electron microscopy (SEM) image of the hybrid platform. The robust graphene sheet conforms closely to the tipped surface without

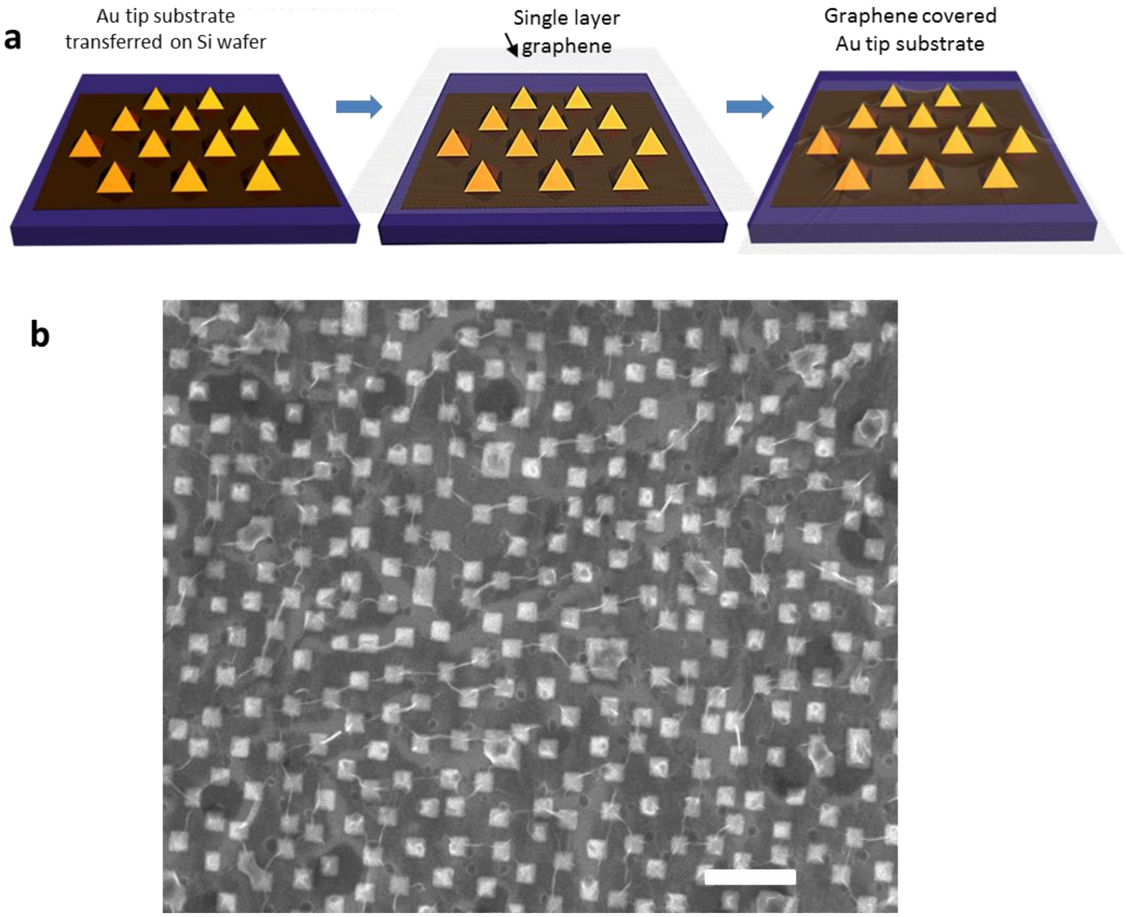

Figure 2.4: (a), Schematic process showing the synthesis of the hybrid platform. The CVD monolayer graphene is transferred onto the Au tip substrate. **(b),** SEM of hybrid platform. Scale bar 1 μm.

breaking into pieces. The intrinsically high strength of graphene keeps it from being stretched broken between neighboring sharp tips. The non-planar topology of the Au tipped surface necessitates folds in graphene as it interacts with its surrounding *via* van der Waals force. The van de Waals force clamps graphene to the substrate, leading to spatially inhomogeneous curvatures around the graphene folds at nano-features when it attempts to conform very well to the nano-pyramid morphology. Parallel long hanging graphene folds with atomic apex are observed along the nanopyramid arrays in **Figure 2.4b**. As will be discussed later in Chapter 4, these graphene folds are believed to be the origin of a new set of D-band in graphene Raman spectrum.

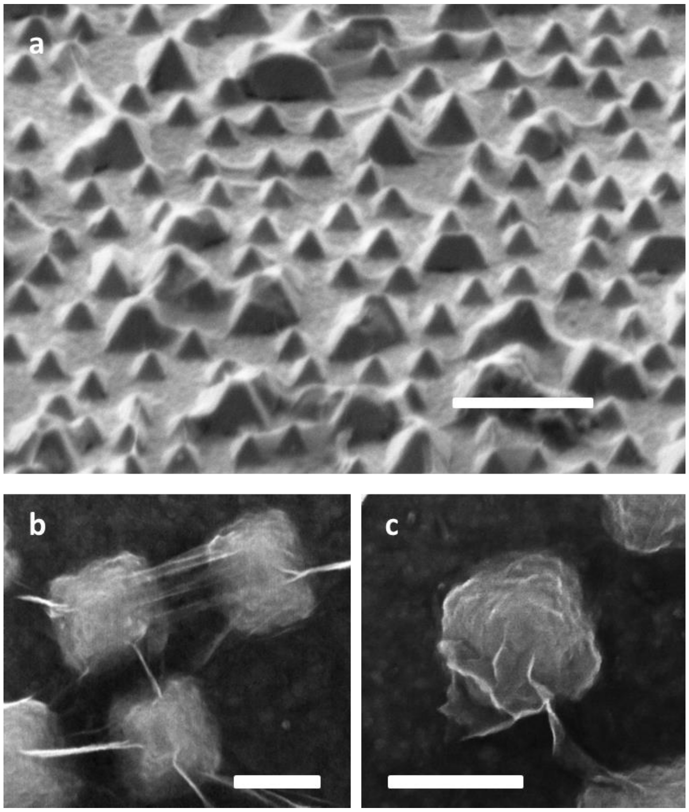

Figure 2.5: (a),Tilt SEM image of the graphene covered Au tips. Scale bar 1 μm. **(b),** Graphene features in between tips. Scale bar 200 nm. **(c),** Graphene features formed on a tip. Scale bar 200 nm.

Figure 2.5a shows a tilt SEM image of the hybrid platform. The tips are very sharp with radius of curvature at the apex as small as 1 nm in previous study [119]. Such sharp apex serves as hotspot with extremely strong localized enhancement. When graphene sheet is transferred to the Au tip surface, one-dimensional folds form in between individual tips. Aside from folds, suspended strained graphene is shown in **Figure 2.5b**. Graphene also forms flower-like features when it covers the 200 nm tip. The existence of such delicate graphene features indicates the possibility of near-field optical confinement of graphene cooperated with nanopyramid substrate. All those graphene features, which can be carefully tailored, are of great interest not only in spectral study, but also biological applications with regard to interaction between graphene.

2.4 Conclusion

In this chapter, we have demonstrated the synthesis of the hybrid platform including fabrication of the periodic Au tip substrate together with CVD growth and PMMA transfer of monolayer graphene. The template based approach for Au tip substrate fabrication enables producing highly and uniformly enhancing substrates with various opportunities of further optimization. The remarkable mechanical, electronic and photonic properties of graphene make it a promising candidate in applications in biosensing. The plasmonic oscillations induced by incident field in Au tips leads to large enhancement of the local electric field as well as the Raman intensity of graphene. The high reproducibility and spectral quality of the hybrid platform, which is clearly distinguishable from nanoparticle based conventional SERS systems, suggests the possibility of developing a robust platform for SERS. The combination of the Au tip substrate and graphene will give rise to unique phenomena that have never been brought to light.

3

FDTD Simulations of Periodic Au Tip Substrate

3.1 Introduction

3.1.1 Surface Plasmon (SP)

Plasmonics [143], an emerging field investigating the interesting optical properties of metallic nano-structures [144-146], has stimulated researches on photovoltaic devices [147], plasmonic waveguide [148], electro-optical modulation [149], SERS [150], light harvesting [151-153], biosensing [154-156] and so on [157-160]. The development of nanofabrication has made novel plasmonic phenomena to be revealed at sub-wavelength scale [161]. Nano-plasmonics is devoted to the optical phenomena at nanoscale in metal nano-structrued systems [162]. Such systems have a remarkable property to concentrate incident optical energy on the nanoscale due to the so-called surface plasmons (SPs). SPs are coherent delocalized electron oscillations existed at metal/dielectric. SPs are generated when electron-charged oscillations resonantly interact with the EM field of incident light. The decay length of SPs into the metal is short (~10 nm) thus SPs are likely bound to the metallic surface. The SPs originate from the negative real part of dielectric function. For the good plasmonic metals to support surface plasmon resonance their dielectric function also satisfies $\mathrm{Im}\,\varepsilon \ll -\mathrm{Re}\,\varepsilon$ that the losses are small. Surface plasmon quality factor $Q = -\mathrm{Re}\,\varepsilon / \mathrm{Im}\,\varepsilon$ is introduced to evaluate metals. The rates of excitation and emission intensity are both enhanced proportional to the local field intensity by a factor of Q^2. Such phenomenon is also referred to as nano-antenna effect [162]. Silver is usually perceived as a better plasmonic metal since its Q factor is several times larger than gold. Aside from commonly used Au [163-167] and Ag [168-170] based plasmonic structures, relatively cheap Cu [171-174] and Al [175-177] are also extensively explored in plasmonics.

The total plasmonic excitation, consisting of SP charge motion and SP-generated EM-fields, is referred to as localized surface plasmon (LSP) for the surface of nano-structures. LSP originated from the confinement of a SP in a metallic nanoparticle with size comparable or smaller than the excitation light wavelength [178, 179]. The plasmonic response of nano-structures plays a key role in an increasing number of applications including SERS [180,181]. When a molecule is situated in the vicinity of plasmonic metal nanostructures, it interacts not only with the external field but with the local EM field, which is orders-of-magnitude stronger at hotspots. Consequently the enhanced local field causes the enhancement of both radiative and non-radiative processes in which a molecule involves. LSPs are responsible for local SERS enhancements over 10^{10} in the hotspot of the nano-features.

The LSP has two prominent features: (1) The EM field enhancement is highly localized at the surface of nanoparticle [182]. The enhancement falls off significantly with the distance to the surface. (2) The optical excitation and EM enhancement has a maximum value at plasmon resonant frequency [183]. LSP at resonant frequency is referred to as Localized Surface Plasmon Resonance (LSPR). For nanoparticles of noble metals, the resonant frequency is usually in visible range [184].

Graphene plasmonics [185] is also rapidly emerging as potential technique for optoelectronic applications. Though nanoribbons of graphene show promise of plasmons in near infrared or even visible range, plasmons of extended graphene are currently observed in mid-infrared and long wavelength range [186,187]. It hasn't been reported of the interaction between graphene plasmons and SPs supported by nearby metallic nanostructures in visible range. Besides, graphene very weakly interact with light [188]. In this work we consider the Au tip substrate as the key contributor to EM enhancement and graphene as the origin of chemical enhancement.

3.1.2 Finite Difference Time Domain (FDTD) Method

The analysis of various plasmonic geometries requires numerical methods to solve Maxwell's equations using iterative procedures in the computational domain. Three-dimensional finite difference time domain (FDTD) method is extensively used in nano-plasmonic simulations [189]. FDTD not only serves as a powerful numerical tool for theoretical studies on EM enhancement, but more importantly provides with a platform for designs of plasmonic systems for various purposes [190].

FDTD is based on time and space discretization of the Maxwell differential equations. Space is divided into box-shaped Yee cells [191] and time is segmented into steps that each represent time required for the field to travel from one cell to the next one.

$$\nabla \times \vec{E} = -\frac{\partial \vec{B}}{\partial t} \tag{3.1}$$

$$\nabla \times \vec{H} = \vec{J} + \frac{\partial \vec{D}}{\partial t} \tag{3.2}$$

where $\vec{E}$, $\vec{B}$, $\vec{H}$, $\vec{J}$, $\vec{D}$ are the electric field, magnetic induction intensity, magnetic field, current density and electric displacement respectively.

When media (ε, μ, σ) is considered as isotropic, the physical quantities hold the relationship

$$\vec{D} = \varepsilon \vec{E}, \vec{B} = \mu \vec{H}, \vec{J} = \sigma \vec{E} \tag{3.3}$$

where ε, μ, σ are dielectric constant, magnetic permeability coefficient and electrical conductivity separately. Thus it’s possible to use a staggered mesh to replace the space and time derivatives by central differences. $\vec{E}$ and $\vec{H}$ field components are located at different points of the mesh. For instance, the time and space evolution of x component of $\vec{E}$ can be written as

$$E_x\Big|_{i,j,k}^{n} + \frac{\Delta t}{\varepsilon_{i,j,k}} \times \left[\frac{H_z\Big|_{i,j,k}^{n+1/2} - H_z\Big|_{i,j-1,k}^{n+1/2}}{\Delta y} - \frac{H_y\Big|_{i,j,k}^{n+1/2} - H_y\Big|_{i,j,k-1}^{n+1/2}}{\Delta z} - J_x\Big|_{i,j,k}^{n+1/2} \right] \tag{3.4}$$

where i, j, k, n are integers running on the space and time mesh, Δx , Δy , Δz are the space mesh steps while Δt is the time mesh step.

The whole simulation cell is usually restricted to a finite region due to limitation of computer memory. Perfectly Matched Layers (PML) boundary condition is normally applied to avoid the wide range of incident scattered fields at boundary [192,193]. PML absorbing boundary, constructed to absorb light waves (both propagating and evanescent) with minimal reflections, is the widely used absorbing boundary in much of computational electromagnetism. An ideal PML boundary should produce zero reflections. Periodic boundary condition, which allows for calculating the response of the entire system by only simulating one unit cell, is applied to periodic structures. The periodic boundary condition simply copies the electromagnetic fields which occur at one side of the simulation and inject them at the other side.

Stair effects on the surfaces of metallic features are impossible to avoid due to the cubic nature of FDTD mesh. In order to achieve accurate field distribution profile for the system under study, the size of Yee cell is expected to be much smaller than the excitation wavelength [194]. The cell size should also be carefully chosen to model the features of the object geometry in the system. Still, computational resources limit the further deduction of the Yee cell size. For SERS systems, the Yee cell size is around 1 nanometer. Drude model [195] is used in FDTD for dispersive materials since complex permittivity of metals is strongly frequency dependent in optical frequency range.

FDTD Solutions by Lumerical Inc. is a FDTD based numerical simulation package that allows for resolving of electromagnetics in the vicinity of complex three dimensional nano-structures. Lumerical FDTD Solutions has been extensively used to model the plasmonics of various 3-D nano-structures [196,197]. The accurate simulations are therefore of utmost importance for accurate characterization and design of plasmonic nano-structures.

This chapter presents the studies on 3-D FDTD simulations of the periodic Au tip substrate to elucidate its plasmonic behavior. Chapter 3.2 describes the model setup procedure for simulation. Chapter 3.3 discusses the simulation results on both near field EM distribution and the plasmonic resonance behavior of the Au tip substrate.

3.2 FDTD Simulation Model Setup

Figure 3.1 shows a simplest model setup of periodic Au substrate with the pair of Au pyramids as unit cell. An ideal situation that the substrate is homogeneously periodic on the infinite x-z plane is simulated when x and z boundary conditions are set periodic. The material, size, arrangement and separation of the nanp-pyramids, polarization pattern, the wavelength and direction of the incident beam are tunable. The optical constants of Au were taken from E. Palik [198] in the spectrum range of 200 nm to 1000 nm. PML boundary condition was applied for z-direction, while periodic boundary condition was set for x and y directions of the FDTD simulation region.

In the simulation, the size of the nano-pyramid is set as 200 nm and the distance between the edges of two pyramids is set as 200 nm as well. The Au film underneath Au pyramids has the thickness of 200 nm. Since over 95% of EM energy loses in the depth

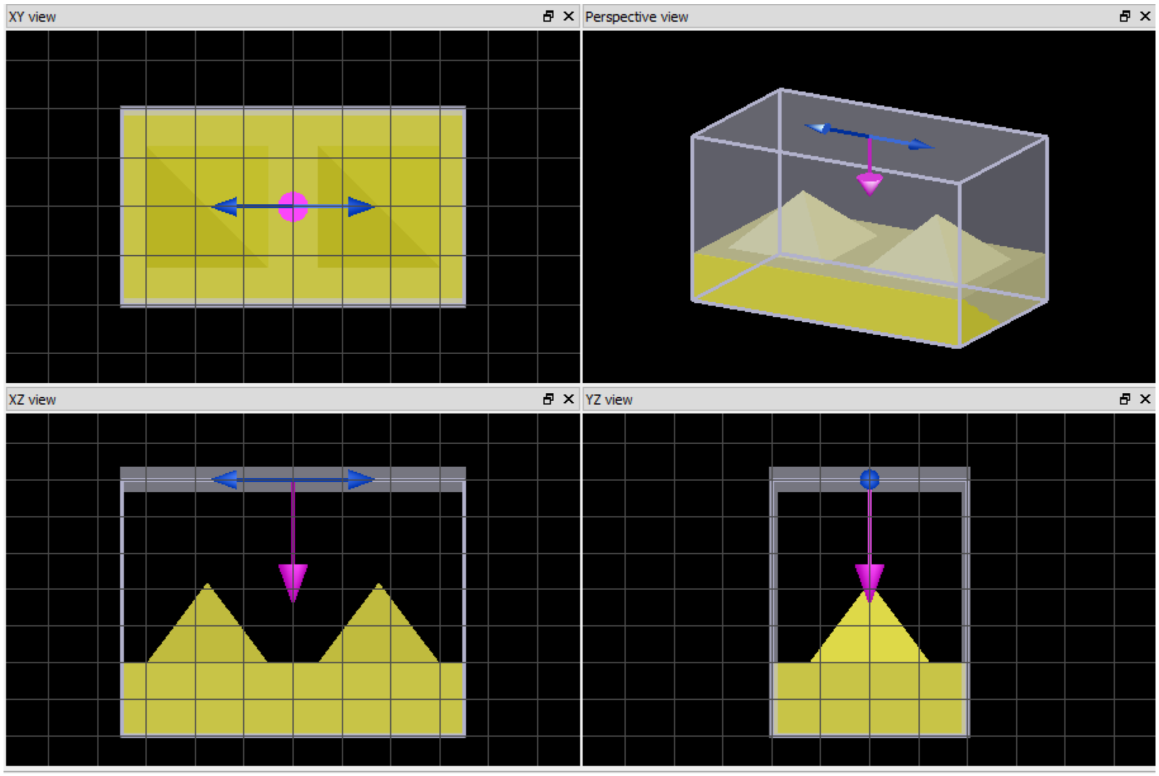

Figure 3.1: A simplest FDTD simulation model setup of periodic Au nano-pyramid substrate.

of about 15 nm into the Au film, the influence of layers under the Au tip substrate can be neglected. The smallest simulation cell has the size of 800 nm*400 nm*400 nm which includes two individual pyramids. The FDTD algorithm supports a graded mesh of Cartesian cells. The size of the mesh cells varies as a function of position over the simulation region. Such a non-uniform mesh makes FDTD calculations more accurate through reducing numerical dispersion and improving the interface resolution. The mesh size is not uniformly distributed in a conformal mesh with the mesh size as low as 0.8 nm at regions of interest (e.g. nano-pyramid apex). The linearly polarized light is vertically incident on the Au tip surface with tunable wavelength. Plane wave sources are used as incident light source to inject laterally-uniform EM energy from one side of the source region. The incident source is represented by a normalized y-polarized plane wave propagating in the z direction. Frequency-domain field monitors are used to collect steady state EM field data in the frequency domain from a simulation. The present data was assembled using Lumerical FDTD's in-house post-processing environment.

3.3 Results and Discussion

3.3.1 Electromagnetic Enhancement Distribution

3D FDTD simulation of electric field has been performed to the Au tip substrate (**Figure 3.2**). The precise location of the SERS hot spots relative to the location and the orientation of the nano-pyramids are investigated. **Figure 3.2a** illustrates the x-z view of two individual tips and the incident light. **Figure 3.2b-c** shows the x-z and x-y views of the electric field amplitude distribution for incident light wavelength 633nm respectively.

Strong field enhancement appears in between two individual tips as well as at the apex regime. In **Figure 3.3**, the amplification of the apex region is presented, indicating that the sharp apex boosts highest enhancement of $|E|$over 100 times. However, the volume of the high enhancemnt region in between the tips is approximately one order of magnitude larger compared to that at the apex and is expected to be the dominant contributor for Raman spectroscopic studies. In SERS, the chance of an analyte molecule trapped in between two tips is much higher than the chance when it is captured at the

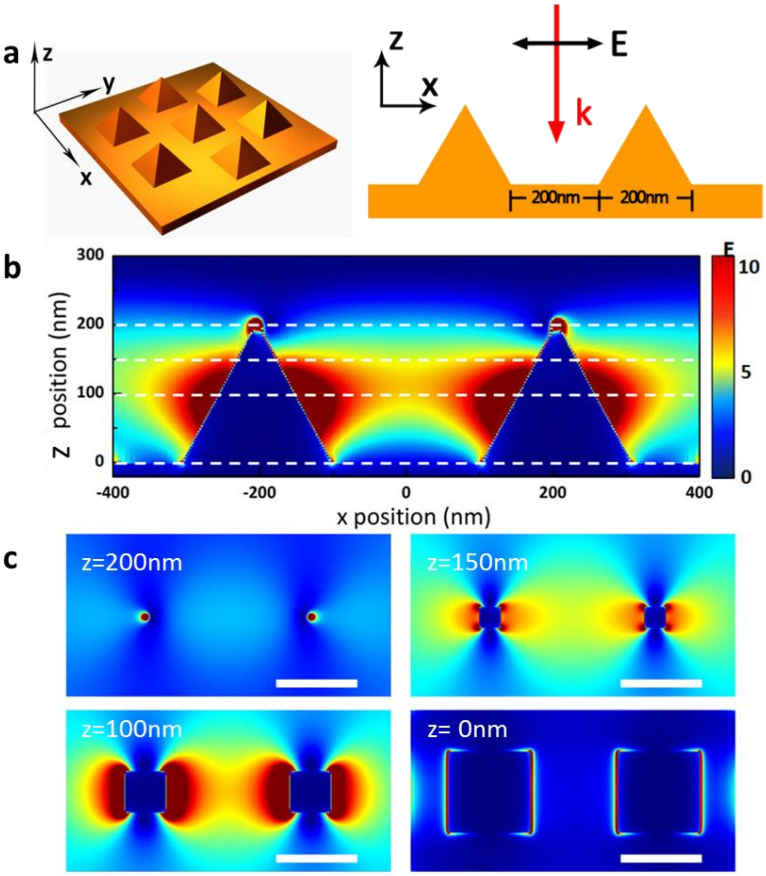

Figure 3.2: (a), Illustration of Au tip substrate under simulation. **(b),** x-z view of the electric field amplitude distribution between two tips. **(c),** x-y view of the electric field amplitude distribution at z=0, 100, 150, 200 nm separately. Incident light wavelength: 633nm.

vicinity of the apex. The regions of strong fields represent evanescent (non-propagating) modes of the plasmonic structure with only near-field coupling capability.

The electric field distribution is highly dependent on the incident light polarization direction (**Figure 3.4**). The hotspots always locate in between two individual tips with regard to the incident light polarization direction. The density of hotspots is expected to be high due to the periodicity and reproducibility of the Au tip structure. The incident light dependent hotspots distribution is evidence that two-dimensional periodic nature leads to incident-laser-polarization-dependent hotspots, adding one more degree of freedom than the randomly dispersed nanostructures.

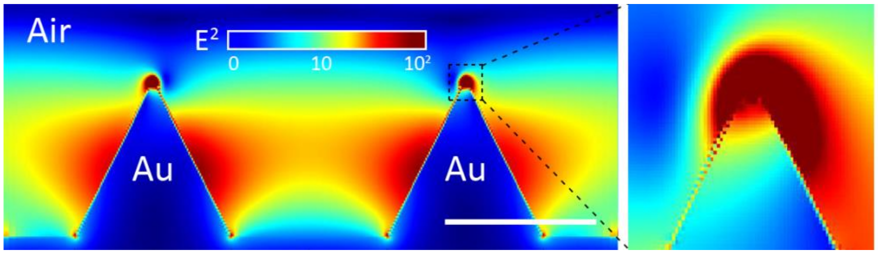

Figure 3.3: Left: x-z view of the electric field intensity distribution between two tips. Right: Amplification of electric field intensity distribution at the sharp apex.

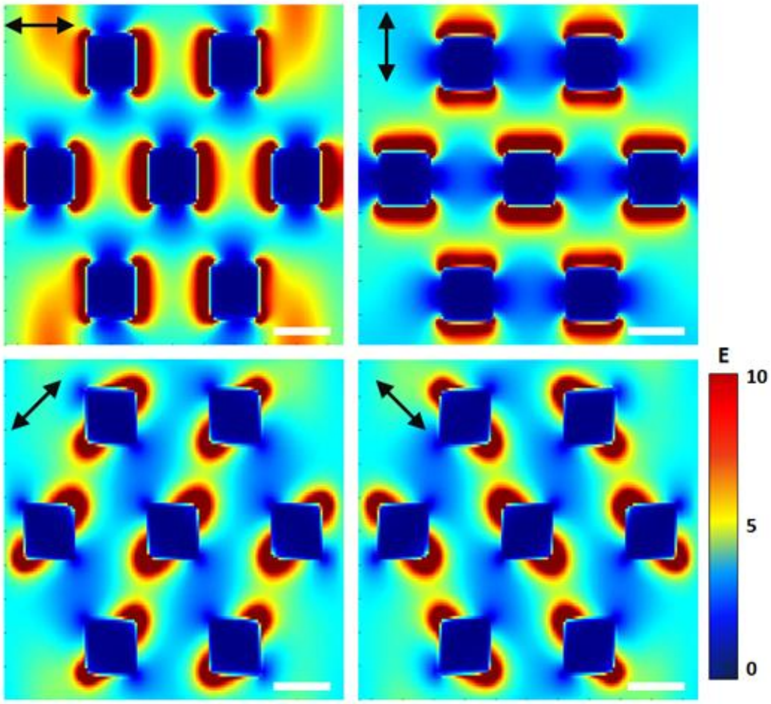

Figure 3.4: Electric field amplitude distribution at various incident light polarization. The black arrow indicates the direction of incident EM field. Scale bar: 200 nm.

3.3.2 Plasmonic Resonance of Au Tip Substrate

To obtain a consistent picture of plasmonic resonance, both near field as well as far field optical responses are needed. The hexagonally arranged 200nm Au nano-pyramids geometry representative of the actual sample structure (**Figure 3.5a**) was used to investigate the plasmon resonance tunability by varying incident wavelength. The extinction cross-section is the sum of the absorption and scattering cross-sections

$$\sigma_E(\omega) = \sigma_S(\omega) + \sigma_A(\omega) \tag{3.5}$$

The scattering cross-section is defined as

$$\sigma_S(\omega) = \frac{P_S(\omega)}{I_{Inc}(\omega)} \tag{3.6}$$

where P_s is the total scattered power (W) and I_{Inc} is the incident intensity (W/m^2). The absorption cross-section is similarly defined as

$$\sigma_A(\omega) = \frac{P_A(\omega)}{I_{Inc}(\omega)} \tag{3.7}$$

where P_A is the total power absorbed by the Au tip substrate.

Figure 3.5b shows the simulated far field extinction spectra as well as near field electric field distribution of the tip substrate. The extinction cross-section, which can be decomposed into absorption and scattering contributions, is simulated in the spectrum range of 200 nm to 1000 nm. The hexagonally arranged Au tip substrate exhibits an extinction peak at ≈600 nm, with FWHM ≈100 nm. The figure clearly depicts the incident light wavelength of around 600 nm to excite localized plasmon resonance of the Au tips.

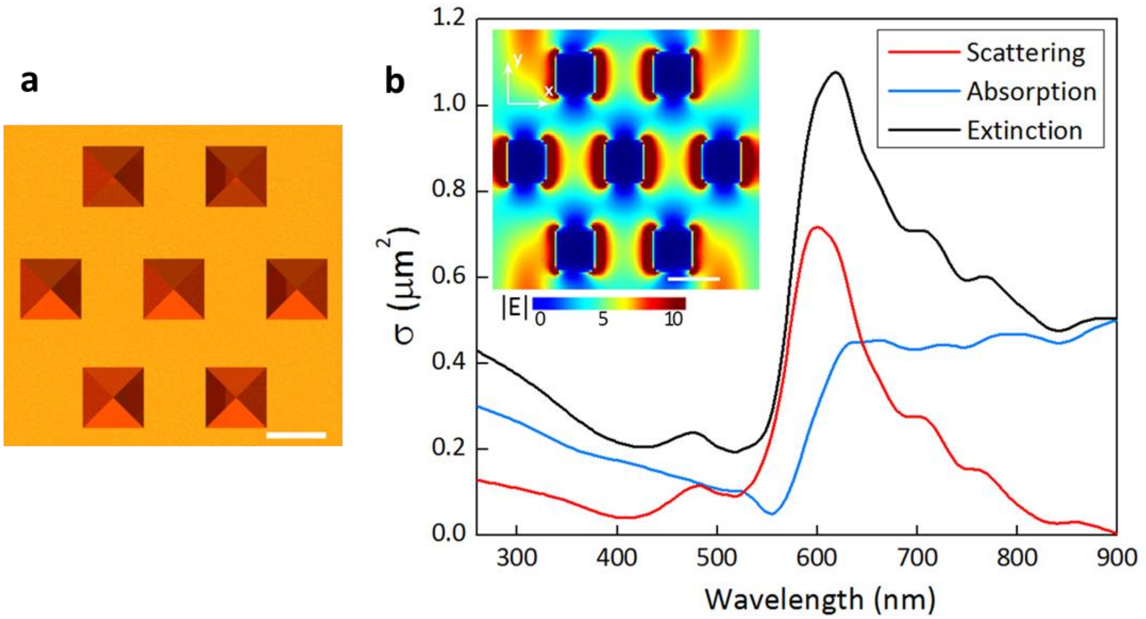

Figure 3.5: (a), Illustration of Au tip substrate under simulation. **(b),** FDTD-simulated extinction (black line), absorption (blue line) and scattering (red line) cross-sections and electric field distribution of periodic hexagonally arranged Au tips. Scale bar 200 nm.

The simulated field intensity maps at three wavelengths (514 nm, 600 nm and 633 nm) in **Figure 3.6** also show the wavelength dependence with a clear peak characteristic of resonant behavior in accordance to the extinction result. 514 nm and 633 nm are the two most commonly used laser wavelengths in Raman spectroscopy. It could be noted that the E-field enhancement is the strongest at resonant wavelength 600 nm. However, at 633 nm excitation the E-field enhancement is comparable to the enhancement at 600 nm while at 514 nm the enhancement is much weaker. The result is in agreement with the extinction data.

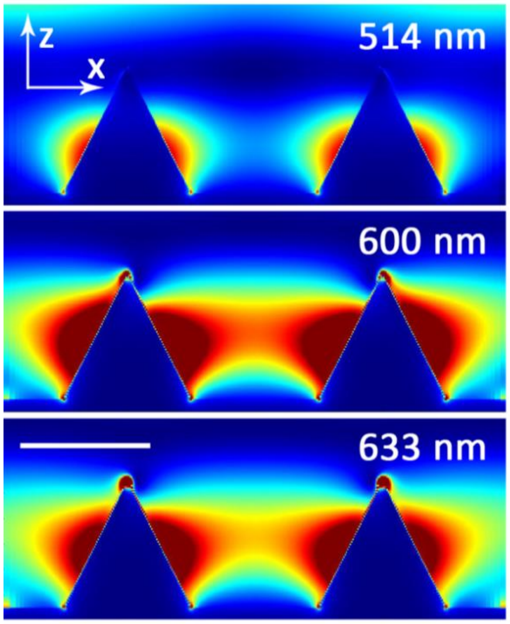

Figure 3.6: x-z view of simulated field intensity profile at three incident wavelengths (514 nm, 600 nm, 633 nm).

3.4 Conclusion

This chapter comprehensively investigates the behavior of the EM fields around the periodic Au tip structure using the numerical simulation method FDTD. FDTD is of utmost importance for precise characterization as well as design and optimization of the nano-structures for SERS applications. Considering that the synthesis and intricate control of the Au tip configuration has been achieved, it is of importance to model the geometry accurately to identify its plasmonic behaviors. The numerical simulation package Lumerical FDTD Solutions is a versatile tool that can be used to describe nanoscale electromagnetics of 3-D geometries precisely.

In summary, 3-D FDTD method has been used to study the near-field electromagnetic intensity distribution upon the Au tip substrate together with the far-field optical response to incident light of different wavelength. The simulation results obtained with the Au tip substrate indicate that hotspots with average 10 times enhancement of |E| are identified in between tips using computational electrodynamics modelled 3-D EM field distribution. It is also noteworthy to emphasize that the wavelength-dependence of the enhancement is of crucial importance, especially when dealing with SERS. The numerical simulation indicates that the periodic Au tip substrate has plasmon resonance when the wavelength incident light is at 600 nm. To this end the 633 nm He-Ne laser is expected to generate stronger optical excitation of the substrate in Raman spectroscopy.

The obtained results, as a function of wavelength and space, enables one to investigate the plasmonic behavior of the periodic Au tip substrate, which then can be reconciled with experimental analysis. In the following section Raman spectroscopy is utilized to characterize the substrate experimentally.

4

SERS of Graphene-Au Tip SERS Platform

4.1 Introduction

The graphene Raman spectrum is very sensitive to the number of layers, doping, strain, edges, disorders and other modifications due to the resonance Raman scattering process involved [199]. On certain substrates including the most commonly used 300nm-thick SiO_2 on Si, graphene Raman signal can be enhanced by a fair amount [112]. It has been reported that graphene Raman intensity can be enhanced by 20 times when plasmonic gold nano-disk arrays are deposited on the flat graphene surface [200]. In the recent past, the combination of graphene with plasmonic nanostructures has led to significant success in graphene based photodetectors due to the strong enhancement of graphene-light interaction [201-203].

The giant plasmonic enhancement of Au tip substrate has been evidenced by FDTD simulation. For the graphene-Au tip hybrid platform, we expect to observe significant enhancement of graphene Raman signals. Moreover, we hope to extract plasmon resonance information of the Au tip substrate by analyzing graphene SERS. By means of Raman spectroscopy equipped with multiple lasers and a highly versatile motor stage, we were able to explore the novel properties of the hybrid platform. We show that using the hybrid platform the graphene Raman signal can be dramatically increased by up to 1000 times. As a mechanically strong two-dimensional membrane, graphene combined with Au nanopyramid structure in a synergistic way that sheds new light on the graphene D band origin. We observed strong D and D' bands pair in graphene Raman from the cooperative structure with experimental evidence inferring that the D-band pair is not originated from defects related to broken carbon bonds or impurity atoms, but from the mechanical deformation of graphene among nanopyramid features instead. The unique mechanical effect from graphene folding provides a channel for gaining insights into the polarization detection.

Plasmonic behaviors of the Au tip substrate were investigated as well. Plasmonic resonance of the tip structure was apparent from optical reflectivity and is further proved by evidence that graphene SERS intensity is a function of excitation laser wavelength. Furthermore, by Raman intensity mapping of graphene on the Au tip structure, the Raman enhancement profile of the cooperative structure can be obtained, due to long-range stability of graphene Raman spectrum. Both the far and near field plasmonic characteristics of the Au tip substrate demonstrated by graphene SERS are in very good agreement with FDTD simulation results. The significant cooperative plasmonic enhancement and the probing of hotspot profile are essential for biosensing to push the sensitivity to single molecule limit, as well as a promising application in the graphene-based optoelectronic applications.

In this chapter, the SERS of graphene and the plasmonic resonant behavior of the hybrid platform are presented in detail. Chapter 4.2 discusses the experimental procedures including spatially resolved Raman mapping and polarization dependent Raman measurement. Chapter 4.3 demonstrates the results and discussion consist of the remarkable enhancement of graphene Raman, plasmonic properties of the platform, and the D peak assigned to one-dimensional graphene folds free of broken carbon bonds. The work in Chapter 4 can be found in [216].

4.2 Experiment Procedures

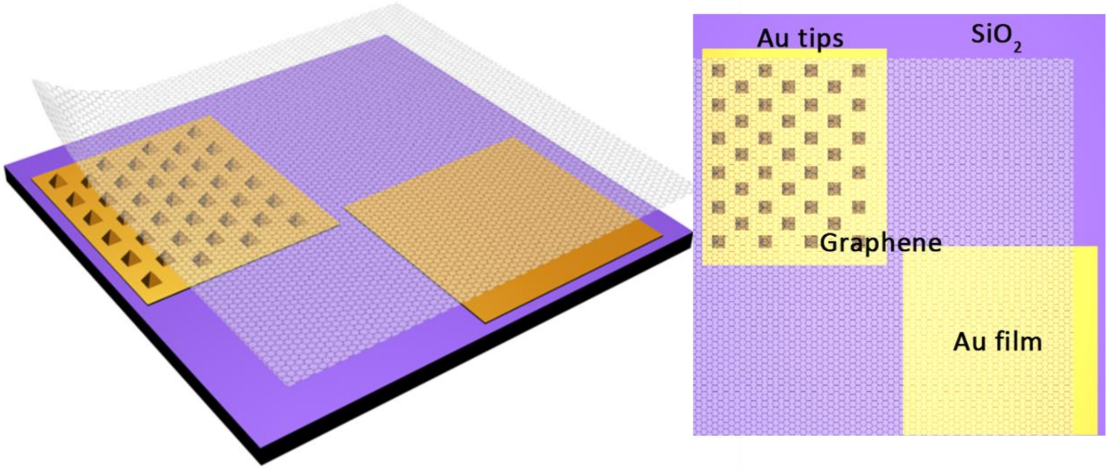

Figure 4.1: Graphene-Au tip structure. Scheme of typical samples used in this session: the same monolayer graphene is transferred to cover substrates consisting three geometries: Au tip, Au film and 300nm-thick SiO_2 on Si.

As shown in **Figure 4.1**, samples used in this study consist of three regions immediately next to one another, namely, Au tipped surface, flat Au surface, and the surface of flat SiO_2 of 300 nm thickness. The Au tipped surface is the hexagonally arranged periodic Au tips with size of 200 nm fabricated using the template approach. Flat Au surface, as a reference to the Au tip surface, is 200 nm-thick Au film deposited on the substrate. Uniform single layer CVD graphene is transferred to cover all three regions. The region with graphene over 300 nm SiO_2/Si serves as the reference of the quality of the transferred graphene by optical microscope. The region with graphene over flat Au is used for comparison with graphene over tipped surface in terms of Raman enhancement. The graphene-Au tip regime allows for the extraction of the novel vibrational features using Raman spectroscopy due to the unique graphene-Au tips combination.

4.2.1 Micro-Raman Spectra and Mapping

Micro-Raman spectra and mapping of graphene, as well as the D band polarization dependence test were carried out using a Renishaw inVia Micro-Raman Spectroscope under ambient conditions. The laser excitation wavelengths for selection are 488 nm, 514 nm and 633 nm from a diode-pumped solid-state laser and a He-Ne laser respectively. The power of the laser was kept around 1.5mW to avoid noticeable sample heating. The laser spot size was ~0.5 μm. We used a ×100 objective (numerical aperture 0.90) and spectral analysis was accomplished with a 1800 lines per mm grating. The spectroscope is equipped with a High Speed Encoded Stage that enables shift of samples in XYZ directions at nanometer steps. Very high spatial resolution of ~100 nm can be achieved from the inVia Raman micro stage. The spatially-resolved Raman mapping data is achieved by Raman imaging with step ~0.2 μm in X and Y direction. The Raman imaging data is processed by WiRE 3.2 Raman software.

With the micro-Raman spectroscope, we located and collected the Raman mapping data of graphene on tipped regions with areas on the scale of over 100 microns. Renishaw WiRE 3.2 software enables us to process the mapping data and to do data arithmetic for obtaining the I(D)/I(G) ratio. The SEM images were obtained from Zeiss NVision 40 Dual Focused Ion Beam – Scanning Electron Microscope. We superimposed the Raman intensity mapping image (obtained with a ×100 objective from the Renishaw inVia micro-Raman spectroscope) on the SEM image of exactly the same region to further understand the profile of hotspots. The error of the superimposing is < 10 nm.

4.2.2 Polarization Dependent SERS

The setup for incident light polarization dependence measurement is shown in **Figure 4.2.** The polarization dependence measurement is mainly performed to elucidate the characteristics of the 1-D graphene folds. Renishaw inVia micro-Raman spectroscope equipped with a rotatable sample stage was employed for collecting Raman spectra of parallel folds in graphene sheet with different polarization configurations. The ×100 objective was employed and the backscattered radiation is collected through the same

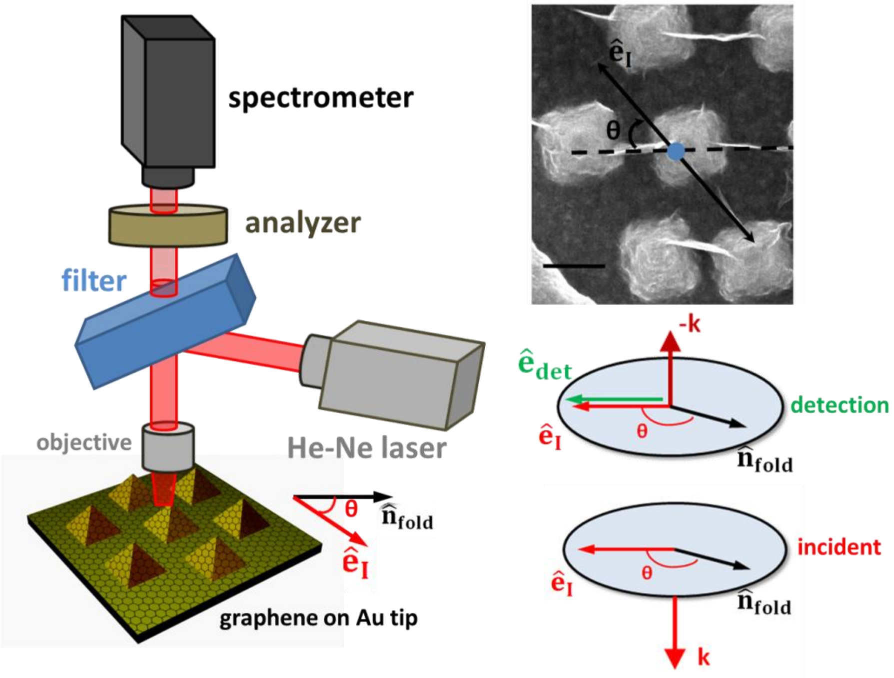

Figure 4.2: Sketch of the setup for polarization dependence measurement. The laser excitation at 633nm is linearly polarized, and is focused on the graphene-Au tip with a ×100 objective. The incident electric field field $\hat{e}_I$ (red arrow) is linearly polarized at an angle θ with respect to the direction of parallel graphene folds $\hat{n}_{fold}$ (black arrow). The sample can be rotated underneath the objective to change θ. The polarization analyzer is adjusted with the optical axis (green arrow) parallel to the incident electric field . **k** is the wave vector of incident light. –**k** is the wave vector of detected light. Scale bar 200 nm.

objective. The laser excitation at 633nm is linearly polarized, and is focused on the desired graphene-Au tip region.

The incident electric field $\hat{e}_I$ is linearly polarized at an angle θ with respect to the direction of parallel graphene folds $\hat{n}_{fold}$. The sample can be rotated underneath the objective to change θ. The polarization analyzer is adjusted with the optical axis parallel to the incident electric field. When the graphene fold is parallel to the polarization direction of incident beam, θ equals to zero degree. A series of graphene fold spectra from exactly the same region were recorded at different θ.

4.3 Results and Discussion

4.3.1 SERS Enhancement of Graphene in Hybrid Platform

Micro-Raman spectra of graphene were obtained from the three different regions using various excitation wavelengths (488nm, 514nm, 633nm) under normally incident light (**Figure 4.3a-c**). Here the Raman enhancement factor is defined as ratio of monolayer graphene Raman intensity (G or 2D band) measured on Au tip substrate to the intensity measured on the Au film region to emphasize the influence of Au tip arrays. For all three wavelengths, remarkable Raman enhancement of graphene can be achieved from the graphene-Au tip platform. The intensity enhancement of graphene Raman peaks of up to a factor of 1000 (with 633 nm excitation laser) is present from graphene on Au tips comparing to that on flat Au provides evidence of plasmonic resonant nature of Au tips.

Figure 4.3d plots the Raman enhancement of D, G and 2D band enhancement (intensity ratios on Au tip to Au film) as a function of excitation wavelength. It clearly indicates that at 633 nm excitation the enhancement is two order-of-magnitudes higher than that at 488 nm and 514 nm. Two observations in **Figure 4.3d** are of paramount interest with regard to the graphene D band: first, the prominent D-band and D’-band pair that is barely visible from graphene on flat Au and SiO_2 region appear in Raman spectra

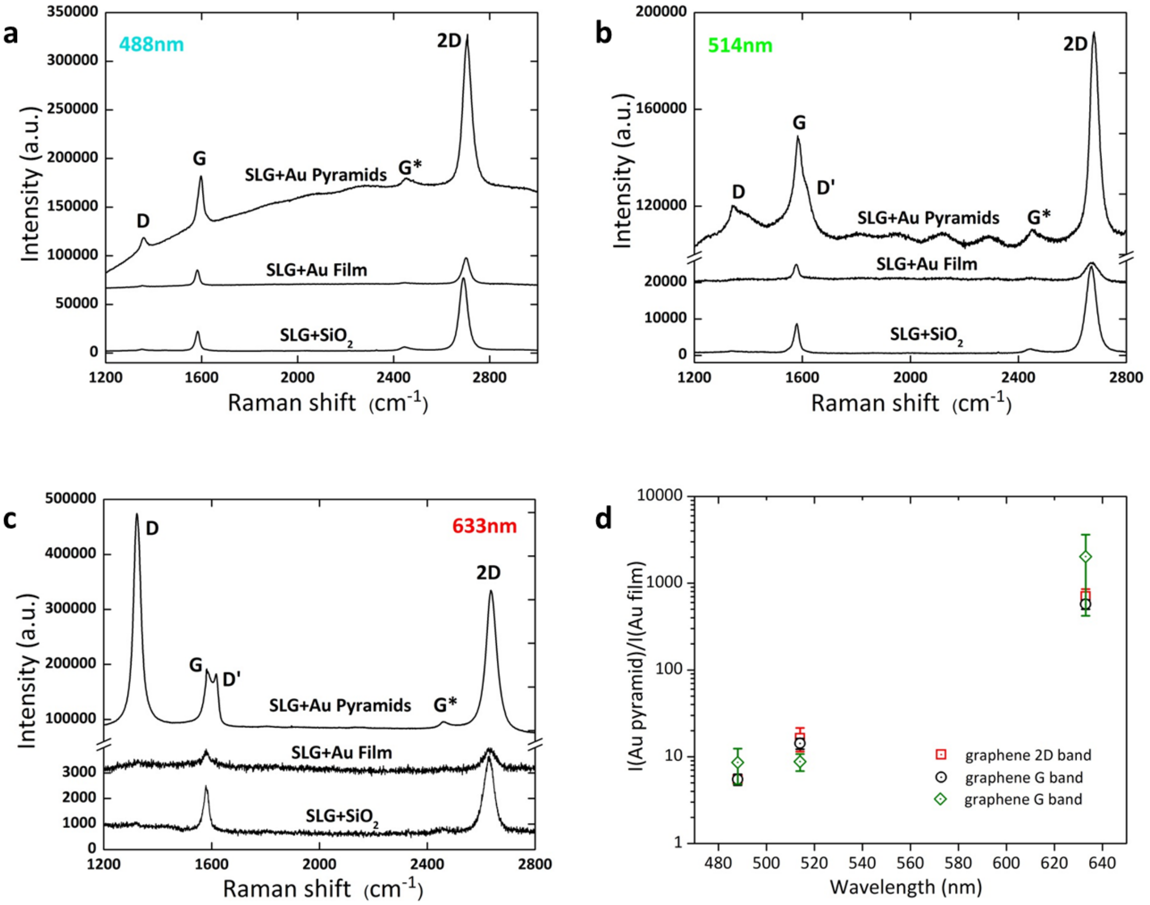

Figure 4.3: Raman spectra of graphene on Au tip structure and the wavelength selectivity. (a-c), Graphene Raman spectra measured from various surfaces (Au tips, flat Au, and SiO_2) with 3 different excitation wavelengths. **(a),** 488nm. **(b),** 514nm. **(c),** 633nm. **(d),** Ratios of intensity of graphene D, G and 2D peaks measured on the Au tip regions to those measured on flat Au regions, as a function of the excitation wavelength, in semi-log scale.

of graphene on Au tip region for all wavelengths. This may indicate that the non-planar geometry of the Au tip surface may be one of the causes; secondly, the enhancement of D band on Au tip surface is not proportional to the enhancement of G and 2D bands. The I(D) to I(G) ratio varies spot-to-spot, evidenced by a very broad range of D band enhancement in **Figure 4.3d**. It could also be noted that the D band intensity increases greatly with excitation light wavelength. The considerable increase of I(D) to I(G) ratio with excitation wavelength is due to the well-known feature for sp^2 carbon materials' Raman scattering [204,205]. We attribute the D-band and D'-band pair to the sharp graphene folds as supported by the polarization dependent studies to be presented below in Chapter 4.3.3.

It should be noted that although the apparent Raman enhancement factor is on the order of 1000, the actual enhancement factor at hotspots may be orders of magnitude higher due to the diffraction limit. While the signal of conventional Raman spectra being derived from an area comparable to the excitation wavelength, Raman signals from plasmonic enhancement comes predominantly from electromagnetic field concentration that is extremely localized to typically nanometer region [206] leading to the actual enhancement factor of up to 10^7 times. The detailed discussion on determination of SERS enhancement factor can be found in Chapter 6.

4.3.2 Plasmonic Characteristics of the Platform

The near and far field property of the Au tip substrate has been demonstrated theoretically in Chapter 3 using FDTD simulation. In **Figure 4.4**, the measured extinction data is in good agreement with the FDTD simulated data. The experimental extinction spectrum of bare Au tipped region shows a maximum in extinction centered around 600 nm with a FWHM of about 100 nm, indicating the fact that at around 600 nm excitation the Au tip substrate is expected to boost highest enhancement due to plasmonic resonance, which is in full agreement with the theoretical results by FDTD.

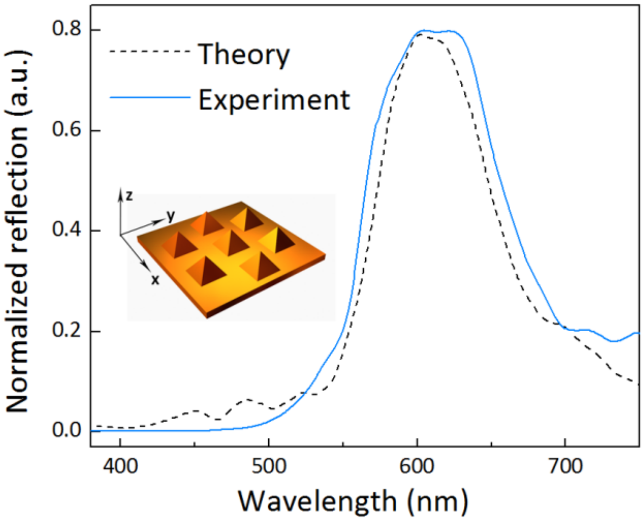

Figure 4.4: The extinction spectrum of Au tips (Blue line) and FDTD simulated extinction (black dashed line)

Here we measured the extinction spectrum [207] of the Au tip substrate in the wavelength range of 300-900 nm. In **Figure 4.5a**, the measured normalized extinction curve is shown with four wavelengths (488, 514, 633 and 785 nm) marked. Considering the extinction, the enhancement is anticipated to be highest for 633 nm and to be lowest for 488 nm. The remarkable Raman enhancement for graphene at 633nm excitation wavelength likely arises because 633nm is closer to the plasmon resonance wavelength of 600 nm. **Figure 4.5b** shows the enhancement of graphene bands as well as the extinction at 4 wavelengths. A strong correlation has been observed between the optical extinction

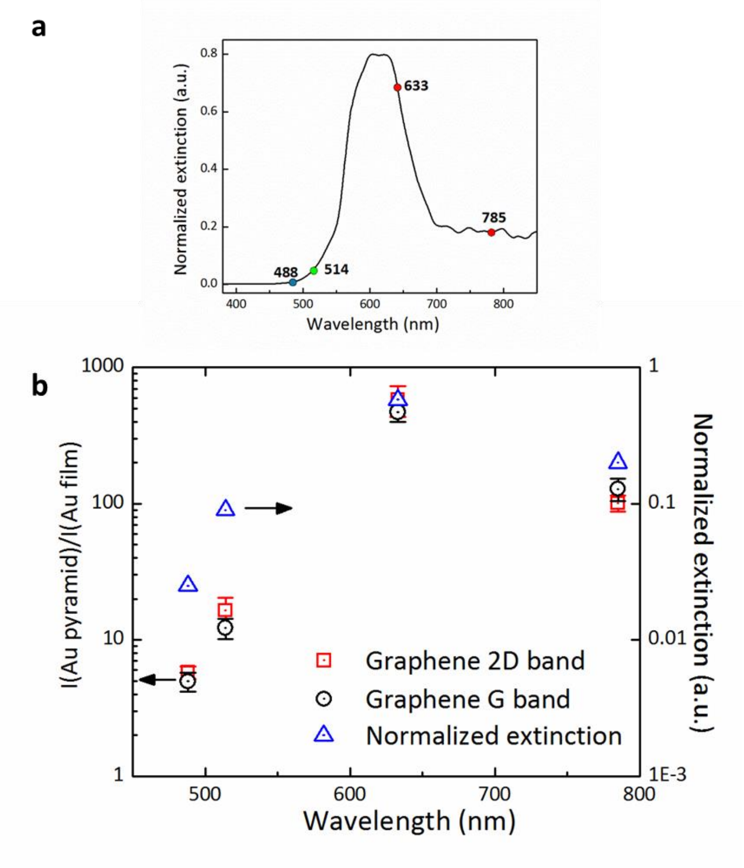

Figure 4.5: (a), the three excitation wavelengths of 488nm, 514nm and 633nm are marked with blue, green and red dotted lines, respectively. **(b),** The normalized extinction at 488nm, 514nm and 633nm wavelengths contrasted to the G and 2D intensity ratio.

and the Raman enhancement as a function of excitation wavelength. The strong spectral dependence of Raman enhancement suggests the significant role of the plasmonic resonances in our cooperative structure. There is a difference in the enhancement factors by about a factor of 10 between Raman intensities and extinction magnitude with the former being larger. This is interpreted as an evidence of cooperative nature in electromagnetic field enhancement [208-210] of graphene on Au tips as the extinction spectrum was measured without graphene coverage.

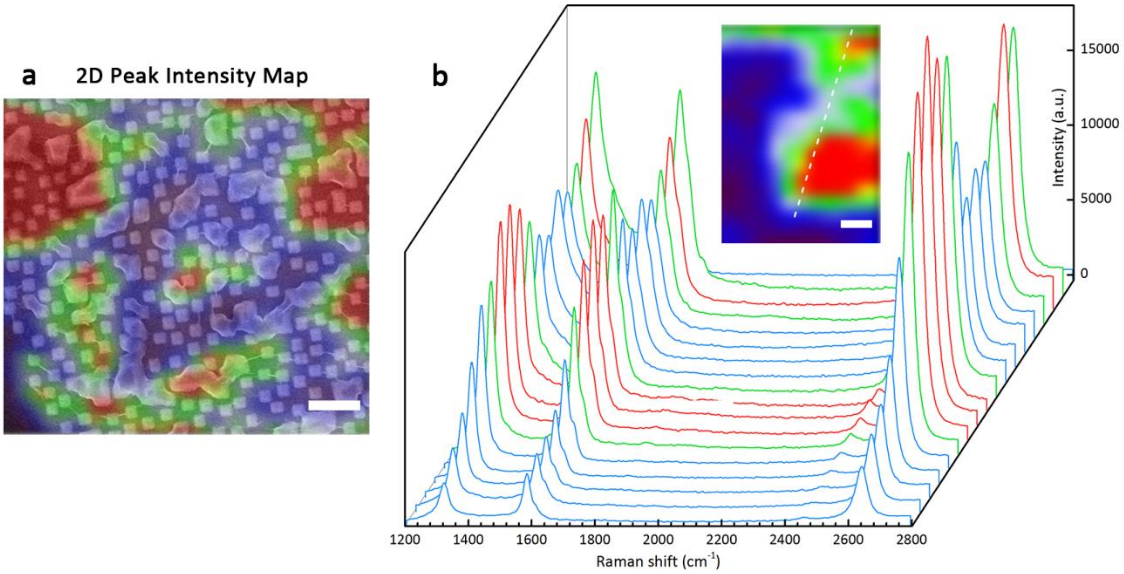

Figure 4.6: (a), Graphene 2D band intensity micro-Raman (633nm) mapping data superimposed on the SEM image of the same region. Scale bar, 1 μm. **(b),** A series of Raman spectra from a line scan across a graphene SERS hotspot. The spectral interval is 200 nm. Scale bar, 500 nm.

We employ spatially resolved Raman to examine the distribution of hot spots. The intensity of graphene SERS bands relates directly the local enhancement factor in the EM field. The distribution of hot spots measured using spatially resolved graphene Raman mapping is shown in **Figure 4.6**. To this end, the hotspots where EM field is significantly increased could be precisely located using graphene SERS intensity mappings over the entire surface prior to performing measurements, leading to significant reduction in the time required. The 2-D nature of graphene makes it an ideal built-in marker for plasmonic structure. The enhancement of graphene Raman bands is a manifestation of the local E-field enhancement since peak intensity is proportional to local E-field in SERS. **Figure 4.7** presents FDTD simulated E-field distribution of ideal periodic Au tip and 2D band intensity distribution of graphene on Au tips. The presence of hot spots in between tips with lateral extent comparable to the pitch of Au tips has been predicted by FDTD simulation results.

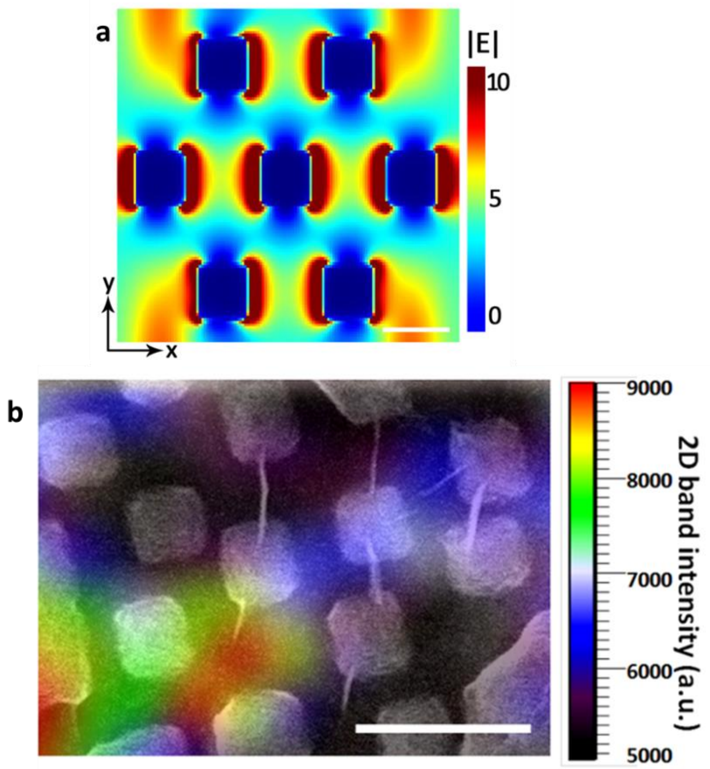

Figure 4.7: (a), the three excitation wavelengths of 488nm, 514nm and 633nm are marked with blue, green and red dotted lines, respectively. **(b),** The normalized extinction at 488nm, 514nm and 633nm wavelengths contrasted to the G and 2D intensity ratio.

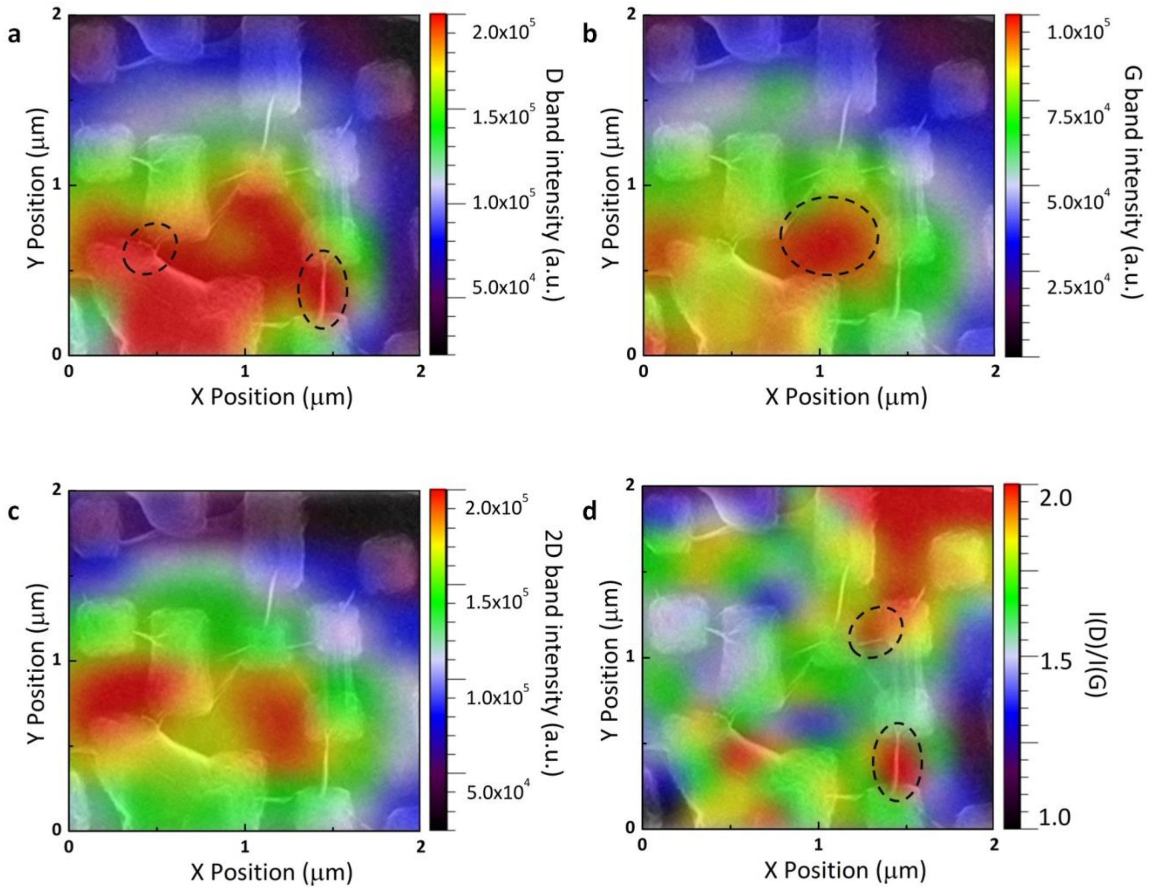

Figure 4.8: SEM and spatially resolved Raman spectra of graphene on Au tipped surfaces. Two-dimensional graphene micro-Raman(633nm) mapping superimposed over SEM images of the measured regions over a 2 μm×2 μm area of **(a),** D band intensity. **(b),** G band intensity, and **(c),** 2D band intensity. **(d),** D/G intensity ratio.

The important role of the Au tips to the formation of hot spots is evident as the location of hot spots for D-band, G-band, as well as 2D-band are all within the same proximity (**Figure 4.8**). However, the exact location of the three bands reveals clear differences provoking in depth examination. Within the diffraction limited spatial resolution of the 633 nm wavelength laser, the G-band and 2D-band hot spots coincide with one another. They are clearly located in between neighboring Au tips away from graphene folds (**Figure 4.8b-c**). Being located over a region of flat Au of ~200 nm in length, such hot spots are not expected on bare Au tip arrays based on well-established understanding from FDTD electromagnetic field modeling. However, the FDTD-predicted hotspots at apex of Au tips are absent. We thus attribute it as an evidence of cooperative behavior between the semi-metallic graphene (with its presence altering the spatial distribution of electromagnetic field and thus the location of the observed hot spots) and the underlying Au tips [211,212]. In contrast, additional hot spots of D-bands are observed coinciding with sharp graphene folds as highlighted by dotted circles in **Figure 4.8a**. These new D-band hot spots possess strong polarization dependence pointing to their plausible physical origin as will be discussed in the following section. **Figure 4.8d** shows the mapping of the ratio of D-band to G-band. It illustrates a clear trend of stronger D-band where graphene folds are. It also shows an anomalous increase in D-band intensity across the entire sample area studied in comparison to graphene on SiO_2 where I(D):I(G)<<1.

4.3.3 Graphene Folds as Broken-Bond Free D-Band Origin

We have observed for the first time (to our knowledge) evidence of D-band origin from sharp folds in graphene away from graphene edges and disorders. As can be seen from **Figure 4.9a**, D'-band intensity (the shoulder of the G-band) varies as a pair with that of D-band as functions of the polarization angle. **Figure 4.9b** shows that the D band intensity can be fitted with a $\cos^2\theta$ function, where θ is the angle between the polarization of incident light and the folding direction in graphene sheets (**Figure 4.2**).

The characteristic $\cos^2\theta$ dependence of D-band intensity as shown in **Figure4.9b** originates from both photon absorption and emission [213,214].

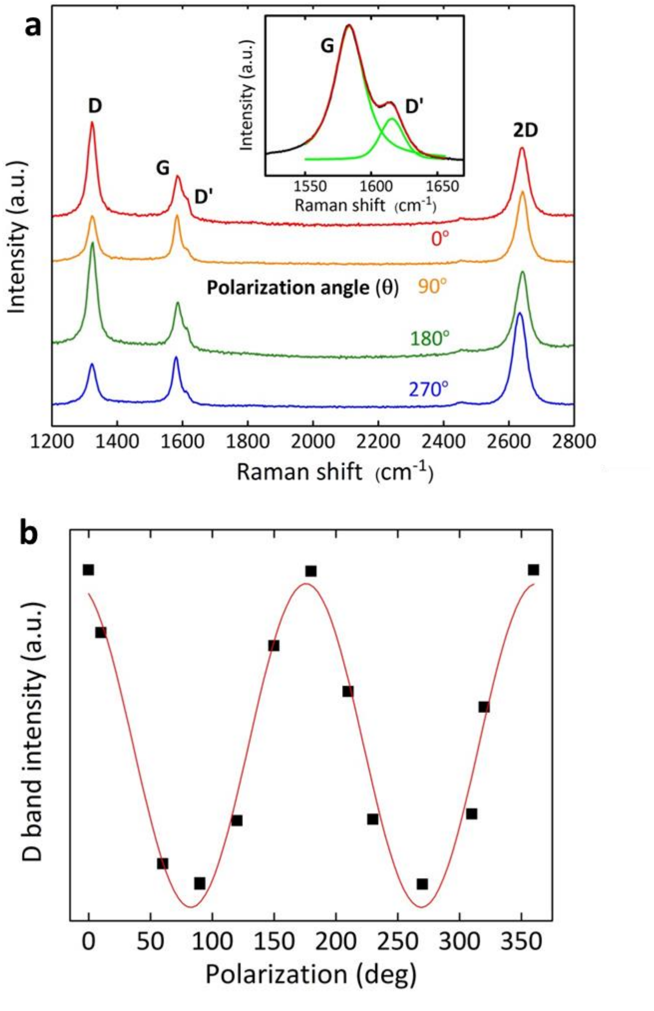

Figure 4.9: (a), Raman spectra obtained with polarization angle θ of 0, 90, 180 and 270 degrees; inset: the curve fitting of G and D’ bands. **(b),** Polarization-dependent D-band intensity of graphene folds. Black squares: measured data; red line: $\cos^2\theta$ fit.

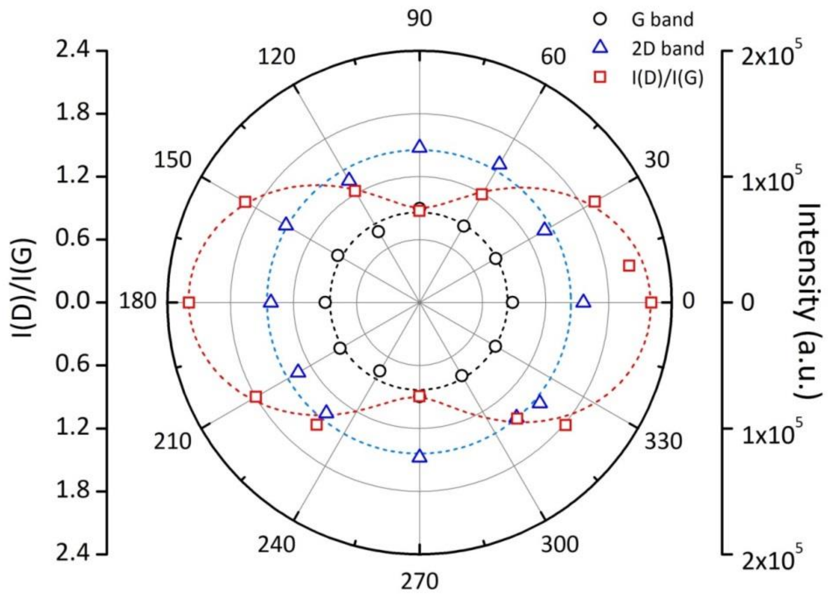

Figure 4.10: D band polarization dependence from Raman (633nm) spectra of graphene on Au tip region. Polar plot of the I(D)/I(G) ratio, G band and 2D band intensity of graphene folds as a function of polarization angle θ. Measured data: black circles, G band intensity; blue triangles, 2D band intensity; red squares, I(D)/I(G) ratio. Red dotted line: $\cos^2\theta$ fit.

Figure 4.10 presents the polar plot of polarization dependence of graphene D, G and 2D bands. The strong polarization dependence as well as the two-fold symmetry of the D-bands is in clear contrast to that of G-band and 2D-band with no observable polarization dependence. The prominent polarization sensitivity of the D-band combined with their location coinciding with the graphene folds are clear evidence that the graphene folds function as one-dimensional defects giving rise to double-resonance D-band scattering. There is no physical reason why randomly located broken carbon bonds could lead to dependence with the observed 2-fold symmetry. Large curvature sharp folds in graphene have been predicted by theory to lead to D-band providing further support to the hypothesis. One important implication of this finding can be traced to the physical origin of D-bands with the associated electrostatic potential fluctuations at the irregularities in graphene, in this case graphene folds. The atomically smooth linear shape of the potential fluctuation (as opposed to randomly placed point defects along the edge of lithographically defined graphene) should function as specular boundary (as opposed to diffuse boundry) ensuring the preservation of momentum and phase of electrons [215].

4.4 Conclusion

In this chapter, the hybrid platform is characterized using micro-Raman spectroscopy. We demonstrate a remarkable graphene Raman enhancement of up to 1000 from what we believe is the cooperative plasmonic resonance of graphene on the uniquely engineered Au tip surface. The plasmonic characteristics of the platform have been emphasized by wavelength dependent graphene SERS enhancement and the graphene hotspots profile illustrated by Raman mappings, which are in good agreement with the FDTD simulation results in Chapter 3. The strong dependence of Raman enhancement factor of graphene on the wavelength of the excitation laser (with the largest enhancement detected at 633nm) lend itself to an evidence of the resonant nature of the Au tipped surface. Graphene Raman intensity mapping places the hotspots in between the neighboring pyramids instead of apex with atomic sharpness indicating the cooperative nature of the resonance.

In addition, a rather prominent D-band appeared at localized hot spots from graphene on Au tipped surfaces that is nearly absent from the exactly same piece of graphene on the immediately adjacent flat Au surface. Polarization dependent Raman spectroscopy shows a strong 2-fold symmetry unique to the new D-band in contrast to the G-band and 2D-band that have no observable polarization dependence. These experimental observations serve as clear evidence for the origin of the D-band being the sharp graphene folds near the apex of Au pyramids.

In summary we demonstrated experimental observation of a giant enhancement of graphene Raman signals from the hybrid platform with clear spectral selectivity, which could potentially benefit the study of biomolecules SERS detection. We present experimental evidence pointing to a new origin of graphene D-band from spatial inhomogeneity in graphene sheets, opening a new pathway to tailoring phonon and potentially electronic band structures of graphene for device applications such as biosensing and photodetecting together with drastically enhanced performance. As is evident, the interests in graphene - plasmonic surface interaction go way beyond simple enhancement of graphene Raman signal. Orders of magnitude increase in local electromagnetic field intensity with the new nano-structured plasmonic surface could make the anticipated SERS of biomolecules a reality. The possibility of placing graphene over nano-structured metal surfaces makes it possible to tailor the bio-chemical properties of a plasmonic surface from the conventional metallic nanostructures to the bio-compatible carbon (graphitic) surfaces. The particular method of fabrication renders the particular plasmonic surfaces amenable to matching the contour of biological cells opening the possibility of spatial-temporal mapping of biological processes that are necessary for understanding cell signaling. Finally, spatially resolved Raman mapping of graphene band intensity opens up new opportunities for precisely locating hotspots in a plasmonic system.

5

Ultrahigh Sensitivity of the Hybrid Platform in Biological Detection

5.1 Introduction

5.1.1 Single Molecule SERS (SM-SERS)

The observation of a single molecule and its structural transformation opens up many opportunities for scientists in various disciplines. Laser-induced fluorescence with far-field, near-field, and evanescent wave excitation has been reported as a single molecule detection tool [217]. However, under ambient conditions the molecular information that can be extracted *via* fluorescence is very limited. SERS, capable of providing highly resolved molecular fingerprints, is ideal for characterizing a single molecule [218]. To achieve single molecule SERS (SM-SERS) it means to enhance the intrinsically small

Raman cross-section (~10^{-30} – 10^{-25} cm^2) by about 10^{15} times (to match the fluorescence cross section ~10^{-16} cm^2) [219]. Consequently extremely high SERS enhancement factor is an important prerequisite for SM-SERS, and the capability of SM-SERS is a criterion of sensitivity for SERS-active systems. Silver colloidal nanoparticle solution [220] has been proved very successful in SM-SERS but the real applications are limited due to toxicity and oxidation. Gold nanostructures, which are chemically stable, bio-compatible and SERS-active, hold great promise in SM-SERS of biomolecules.

5.1.2 Bi-Analyte Method for SM-SERS

Initial SM-SERS reports are based on the combination of extremely low concentrations and very small sample volume of analyte. Though at the concentration of picomolar (10^{-12} M) there will be less than one molecule per μm^2, there is no certainty that the SERS spectrum originates from only one molecule. In many reports [221-223] the fluctuation in molecular SERS was attributed to single molecule event, however, strong fluctuations in both spectral position and intensity happened at high molecular concentrations as well. Among the strategies devised to overcome the issue bi-analyte SERS (BiASERS) technique [224], based on a contrast method, is widely accepted for SM-SERS.

The BiASERS method [225] is a contrast based spectroscopy technique using two different molecules at the same time. This approach facilitates reliable statistics based on a large spectral sample size for single molecule SERS detection. Bi-analyte SERS methodology is aimed to derive reliable statistics for single molecule detection. In BiASERS, SERS measurements are carried out using solutions as a mixture of two different analytes [226]. BiASERS doesn’t rely on the solutions of extremely low concentrations to detect the rare single molecule events. The simultaneous use of two molecules eliminates the uncertainty associated with low-concentration criteria. Due to the nature of a mixture of two molecules, the SERS signals detected are in principle a mixture of two sets of molecular SERS spectra. Thus observation of a SERS spectrum purely originated from one analyte is statistically favorable to be from one single molecule. BiASERS can be applied to a variety of SERS systems [227,228] with ease and it conveys much more convincing and reliable SM-SERS evidence.

5.1.3 SERS Chemical Mechanism (CM)

It is generally agreed that there are two SERS enhancement mechanisms, electromagnetic mechanism (EM) [229] and chemical enhancement (CM) [230], which act multiplicatively. Unlike EM based enhancement, which is a non-selective amplifier for all molecules trapped in the same location, CM based enhancement is analyte-specific [231]. The simplest view of CM is the resonance Raman scattering *via* new electronic states of the analyte molecule (that serves as resonant intermediate states) when it interacts with the surface. In the case when Fermi level of the metal surface is disposed between highest occupied molecular orbital (HOMO) and lowest unoccupied molecular orbital (LUMO) of the analyte molecule, charge transfer excitations from the molecule to metal or vice versa occurs [232]. The excitation of the charge transfer induced state is in an analogous to what observed in resonance Raman scattering, and provides a pathway for resonant excitation to increase the probability of a Raman event.

The distinctive features of graphene in Raman spectroscopy open up opportunities for using graphene as a novel SERS platform to investigate CM independently from EM. It has been discussed in Chapter 4 that E-field enhancement distribution could be derived from SERS intensity mapping of graphene on plasmonic substrate. Besides, molecular charge transfer between molecules and graphene has been shown to be significant for selected vibrations of molecules [233]. To this end, graphene provides a unique platform where both EM and CM of SERS can be explored in detail. Ling et al. [234] proposed Graphene-enhanced Raman Scattering (GERS) and focused on the chemical enhancement *via* molecule-graphene interaction. The highly molecule-selective and vibration mode-specific GERS is usually associated with EF values ranging from 1 to 100. Strong coupling and effective charge transfer between the molecules and graphene are the two favorable indicators of remarkable GERS EFs. To maximize GERS EFs there are two pre-requisitions: (1) The HOMO and LUMO energies of the analyte molecule should be within certain range with respect to graphene Fermi level at a given incident wavelength. Using perturbation theory of Raman scattering, Barros et al. [235] suggested that remarkable SERS occurs when the phonon energy is close to the energy difference between the graphene Fermi level and the molecular HOMO/LUMO levels. (2) Molecules with symmetry and substituents similar to those of the graphene structure prone to generate higher GERS [236]. Such molecular selectivity can be theoretically explained by group theory and the resonant effect between molecule and graphene [237]. The findings indicate the possibilities of modulating SERS chemical enhancement by functionalizing graphene surface [238-240].

5.1.4 Neurotransmitter Sensing

The Brain Activity Mapping (BAM) project has set goals in developing tools to not only measure the activity of neurons in brain circuits but also to analyze and model the brain circuits [241]. Tools capable of providing spatial and temporal profiles of neurotransmitters *in vivo* will be ultimately required. Sensitive detection of neurotransmitters is the cornerstone for advancing the understanding of neurological processes [242]. Dopamine and serotonin, which regulate numerous biological processes, are the most humanly important neurotransmitters [243-246]. Dopamine deficiency causes major clinical symptoms of Parkinson's disease (PD) [247]. Recent research indicates that serotonin also plays a crucial role in PD, especially in PD treatment [248,249].

The detection of these two neurotransmitters especially serotonin remains challenging mainly due to their low basal concentrations in the vicinity of neuronal junctions (10^{-9}M-10^{-6}M) [250]. Voltammetric method gains its popularity in detecting oxidizable biogenic amines [251]. However, its application is restricted in two aspects: (1) It has been difficult to monitor more than one neurotransmitter at a time; (2) The detection of certain neurotransmitter in the presence of other components of body fluid (ascorbic acid etc.) is hard to achieve due to overlapping voltammetric responses [252,253]. SERS has been shown to be one of the most effective alternatives in neurotransmitter sensing with high sensitivity ($<10^{-9}$M) [254-256].

In this chapter we demonstrate single molecule sensitivity of the hybrid platform. The graphene hybrid system boosts a high density of hot spots and enables label-free sensing. The coincidence of molecular precipitation region with SERS hot spots makes detection of a few or a single molecule possible.[32-34] Single molecule SERS detection of Rhodamine 6G (R6G a dye molecule commonly used as the standard in the study of bio-molecules) and lysozyme (a type of simple proteins), is demonstrated experimentally using a bi-analyte approach.[35-37] The high resolution vibrational information provided by SERS enables us to better understand the chemical mechanism, and explore the interaction between molecules and graphene.

Furthermore, we present that the hybrid platform is capable of detecting dopamine and serotonin at 10^{-9} M level in simulated body fluids supplemented with background serum proteins. For dopamine and serotonin in deionized water, the detection limits reaching 10^{-10} M with single molecule sensitivity. The ultra-high sensitivity and the spatially resolving imaging capability boosted by the hybrid platform set the stage for not only *in vitro* applications but potentially *in vivo* monitoring of neurological processes including brain activities.

Chapter 5.2 discusses the experimental procedures for label free molecular SERS measurements and the BiASERS for single molecule detection. Chapter 5.3 demonstrates the ultra-high sensitivity of the hybrid platform evidenced by single molecule detection of dye R6G, protein lysozyme as well as neurotransmitters (dopamine and serotonin), and presents the graphene-based chemical enhancement observed for R6G and lysozyme. Part of the work in Chapter 5 can be found in [257].

5.2 Experiment Procedures

5.2.1 Label-Free Biomolecule SERS Detection

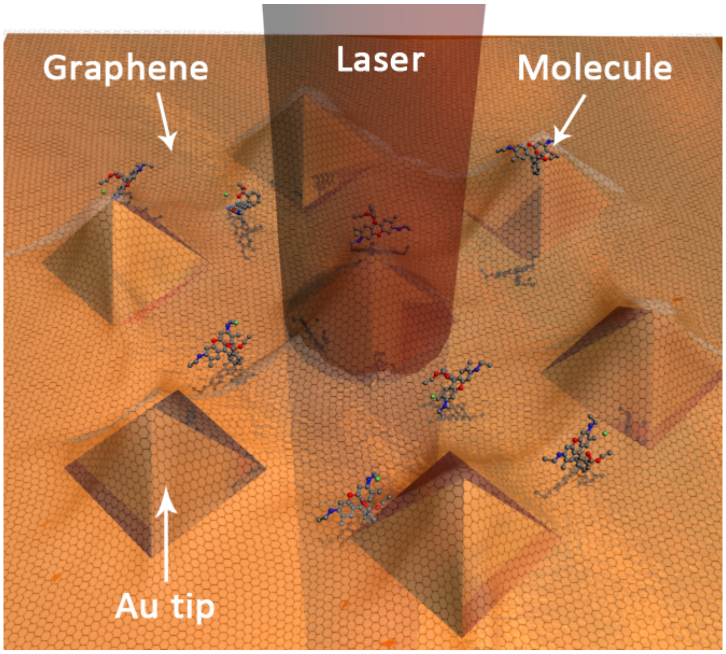

Figure 5.1: Schematic illustration of Raman experiments of molecules on the graphene-Au nano-pyramid (tip) hybrid structure.

The hybrid platform is exposed to analyte molecules at various concentrations for SERS detection (**Figure 5.1**). The coincidence of analyte molecule precipitation with SERS hotspots makes detection of SERS fingerprints from a few or a single molecule possible. Using the graphene-Au tip hybrid system, the detection efficiency can be markedly enhanced due to the presence of graphene as built-in hotspot marker (**Figure 5.2**). The local electrical field enhancement is reflected by the enhanced Raman intensities of graphene characteristic G and 2D bands. Thus from Raman intensity

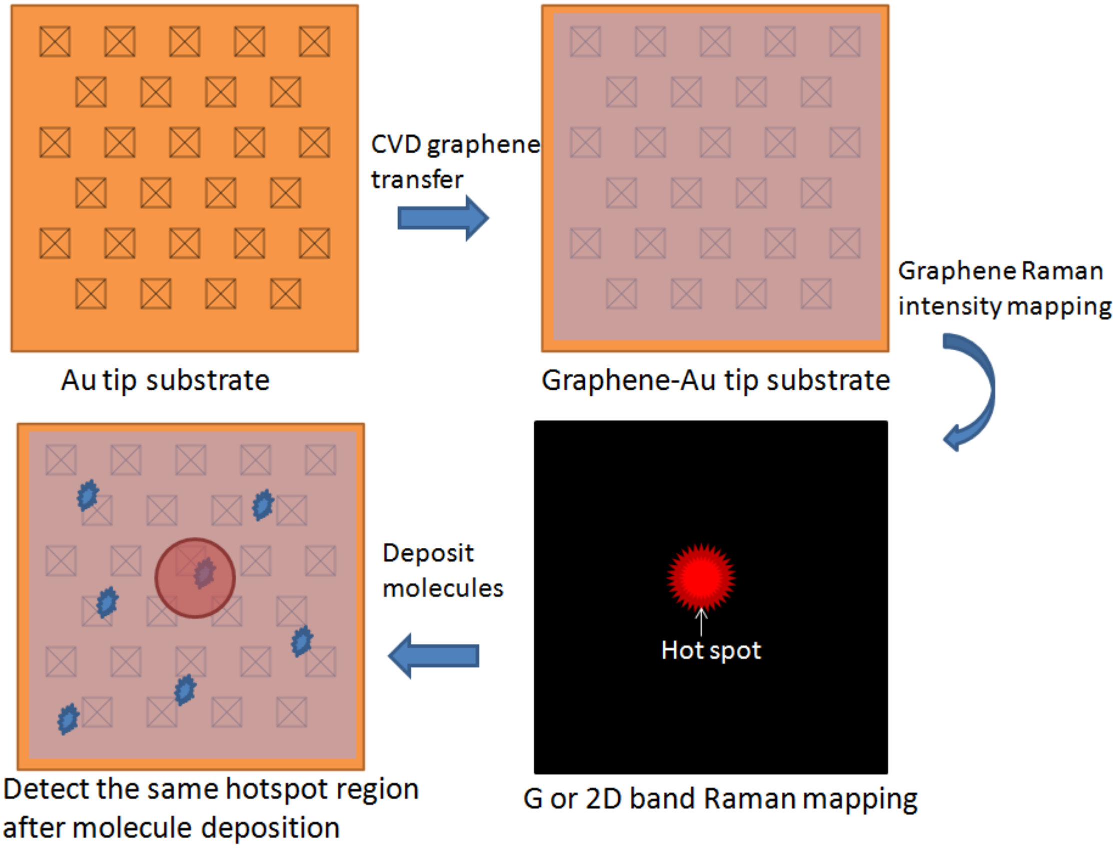

Figure 5.2: Illustration of hot-spot labeling using the graphene hybrid system.

imaging of characteristic peaks of graphene superimposed on the Au tip substrate, the hot spot profile of the structure can be achieved accordingly, since the SERS intensity of graphene characteristic bands that significantly enhanced (with $I(G)_{\text{graphene on Au tip}}/I(G)_{\text{graphene on Au film}}$ larger than 1000) at hotspots is proportional to the local E-field intensity. The locations of hot spots where graphene characteristic G and 2D band intensity can be increased about 1000-fold will be recorded before further experiments. After depositing molecules on the structure, we would start Raman imaging measurements from the pre-located hot spots. It turned out the hot spots for graphene also worked for molecules. Averagely speaking, at one out of ten hotspots pre-located, detectable molecular Raman signal can be achieved from the hybrid system for 10^{-14} M molecular solutions by Raman mappings. With the graphene hybrid system that enables hot spot-labeling, the average accumulation time for effective single molecular detection will be shortened.

Analyte solutions at various concentrations (ranging from 10^{-6} to 10^{-15} M) are prepared for measuring the SERS of analyte molecules. Droplets (of size~2mm) of aqueous molecular solutions (lysozyme (molecular weight 14.388kDa), R6G, dopamine and serotonin are from Sigma Aldrich) are dropped on the sample, and then samples were dried in ambient condition for 1 hour to immobilize the molecules on the substrate surface. Raman mappings were performed at pre-located hotspots. Considering the surface fluctuation of the Au tip surface, we estimated the average molecular coverage being about 15 molecules per μm^2 of the surface geometric area when the solution concentration is 10^{-10} M.

Renishaw inVia micro-Raman Spectroscope features a High Speed Encoded Stage that enables shift of samples in XYZ directions with nominal spatial resolution of ~100 nm. Stable and ultrafast Raman mapping mode is capable of catching the easily missed hot spots in the probed regions. Large-area mappings (~30μm*30μm) with step size of 1 μm and 1s acquisition time are measured to screen the tip surface to identify spots in the first place. Then the laser beam is focused on those spots to acquire SERS spectra of analyte molecules. The acquisition time is set as 10s for a single spectrum acquisition to increase signal-to-noise level. Data are assembled by WiRE 3.2 software and presented as background removed averages of such a data set.

5.2.2 Bi-Analyte Method for SM-SERS

Bi-analyte SERS was performed at 633 nm excitation wavelength for both R6G and lysozyme mixture, as well as dopamine and lysozyme mixture. Here we will use R6G and lysozyme pair as an example since the approach is the same for any bi-analyte systems. First mixture solutions of the R6G molecule in combination with lysozyme as a partner are prepared. The concentrations of the two analyte molecules are identical to each other in the mixtures. Solutions as a mixture of R6G and lysozyme of exactly the same concentration ranging from 10^{-8} M to 10^{-12} M are used for the measurements. Spatially resolved Raman mapping is utilized to simultaneously study SERS of R6G and lysozyme as dilution of molecular solution proceeds. Solutions of concentrations 10^{-8}, 10^{-10} and 10^{-12} M have been used for SERS of the analyte molecules. At each concentration, large-area intensity mappings will be conducted on the platform.

The same bi-analyte SERS was performed to dopamine and serotonin as well. Solutions as a mixture of dopamine and serotonin of exactly the same concentration are used for the measurements with concentrations 10^{-8}, 10^{-9} and 10^{-10} M used for SERS of the analyte molecules. Intensity mappings of SERS peaks purely assigned to one analyte molecule will be obtained to locate the spots where only shows SERS spectrum of one analyte in WiRE 3.2 after measurements.

5.3 Results and discussion

5.3.1 Single Molecule SERS of R6G and Lysozyme

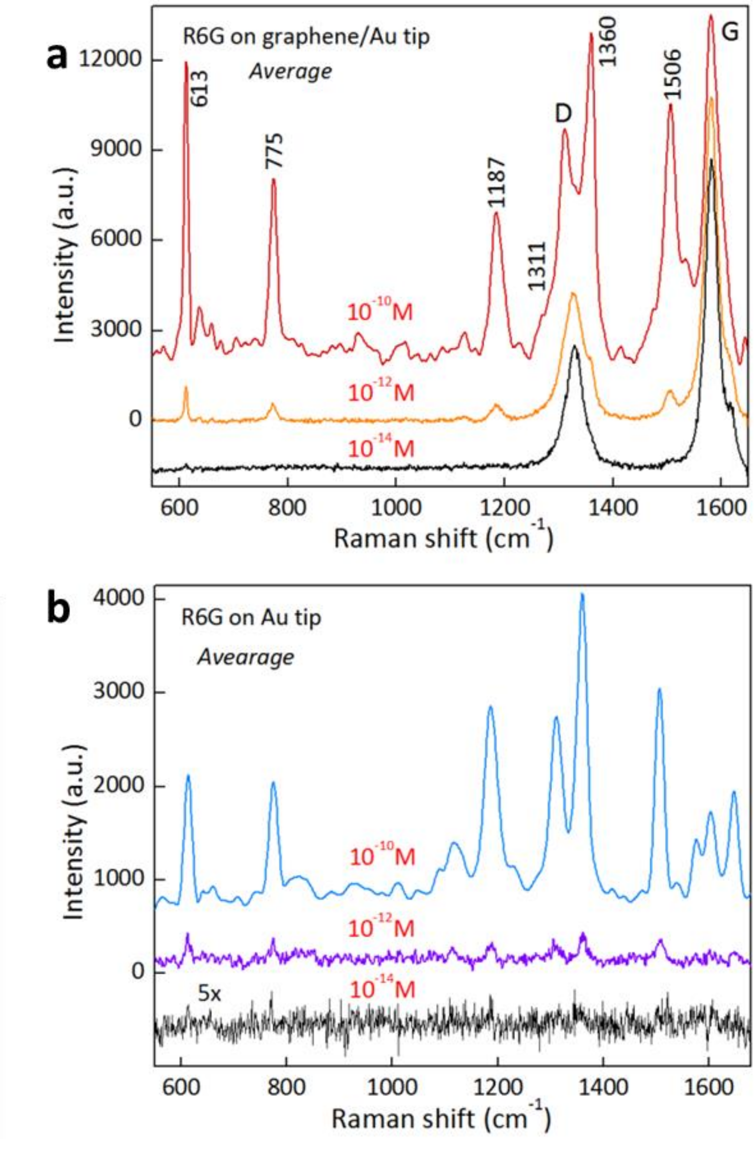

Figure 5.3: (a), Raman spectra of R6G on graphene hybrid structure with 3 different concentrations (10^{-10} M, ~15 molecules / µm^2 10^{-12} M, ~0.15 molecules / µm^2 , 10^{-14} M, ~0.0015 molecules / µm^2) **(b),** Raman spectra of R6G on Au tips with 3 different concentrations. The laser excitation wavelength is 633 nm.)

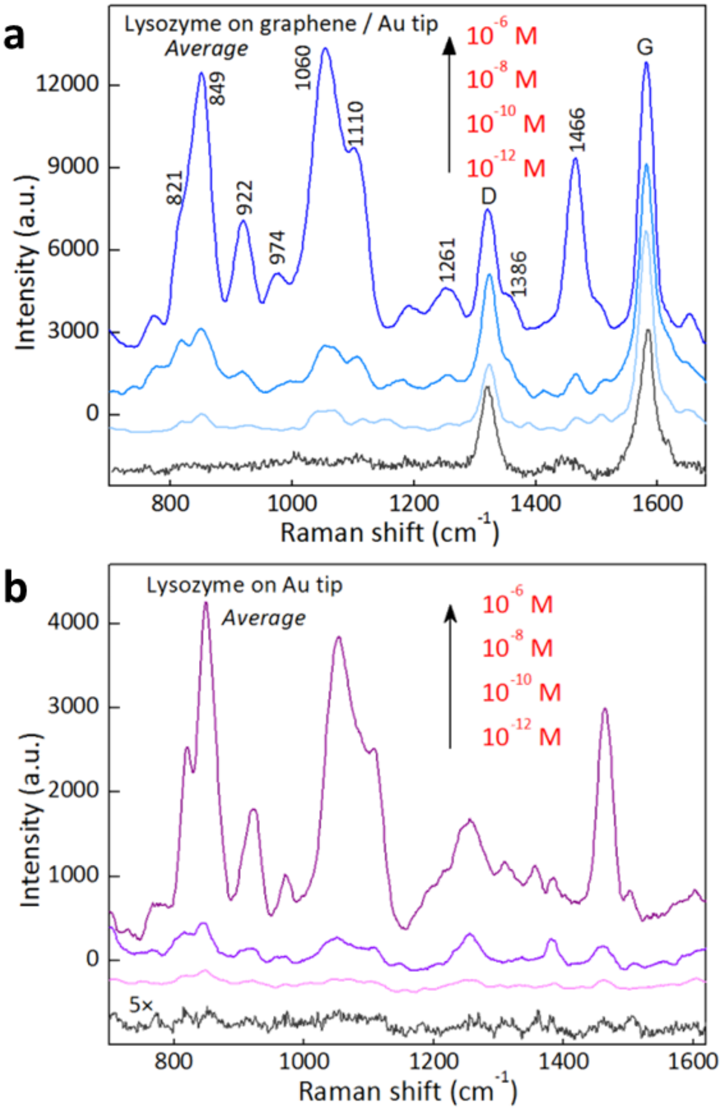

Figure 5.4: (a), Raman spectra of lysozyme on graphene hybrid structure with 4 different concentrations (10^{-6} M, 10^{-8} M, 10^{-10} M, 10^{-12} M,). **(b),** Raman spectra of lysozyme on Au tips with 4 different concentrations. The laser excitation wavelength is 633 nm.)

We demonstrated SERS of R6G and lysozyme separately using the graphene based hybrid system. **Figure 5.3** and **Figure 5.4** show the average Raman intensities of R6G and lysozyme deposited on the graphene-based hybrid platform at various molecular concentrations. We achieved ultra-sensitive detection of R6G with concentration down to 10^{-14}M (equivalent to 0.0015 molecules per μm^2 on average of the surface area) as well as lysozyme with concentration as low as 10^{-12}M (~0.15 molecules per μm^2 of the surface area). The same experiments performed with Au tip surfaces free of graphene also resulted in substantial enhancement of similar orders of magnitude, indicating the crucial role of the periodic Au tip surface for the single molecule sensitivity. The average Raman intensities of both R6G and lysozyme are further enhanced (by approximately a factor of 10) by covering the Au tipped surfaces with graphene, and the enhancement factors vary for the different Raman vibrational modes. The extra chemical enhancement induced by graphene is discussed in the following Chapter 5.3.2.

Single molecule detection was demonstrated with bi-analyte SERS method. An aqueous solution of R6G and lysozyme of the same concentration was dispensed on the hybrid platform for SM-SERS under 633nm excitation. The significant difference between R6G and lysozyme's Raman fingerprints makes them highly distinguishable. Spatially resolved Raman mappings of R6G and lysozyme were measured for three progressively diluted analyte solutions (10^{-8} M, 10^{-10} M, 10^{-12} M). In **Figure 5.5** and **Figure 5.6**, Raman mappings of selected molecular vibration modes at different concentrations are shown. The intensity of R6G band at 613 cm^{-1} is in red and that of lysozyme band at 821 cm^{-1} is mapped in blue. In **Figure 5.5a**, strong signals of both R6G and lysozyme are observed at concentration of 10^{-8} M. The slight difference in signal distribution of 2 maps can be explained by difference in distribution of R6G and lysozyme molecules. The spectrum took from the mapping (**Figure 5.5b**) indicates ensemble averaging, namely, composition of Raman fingerprints from 2 different analyte molecules.

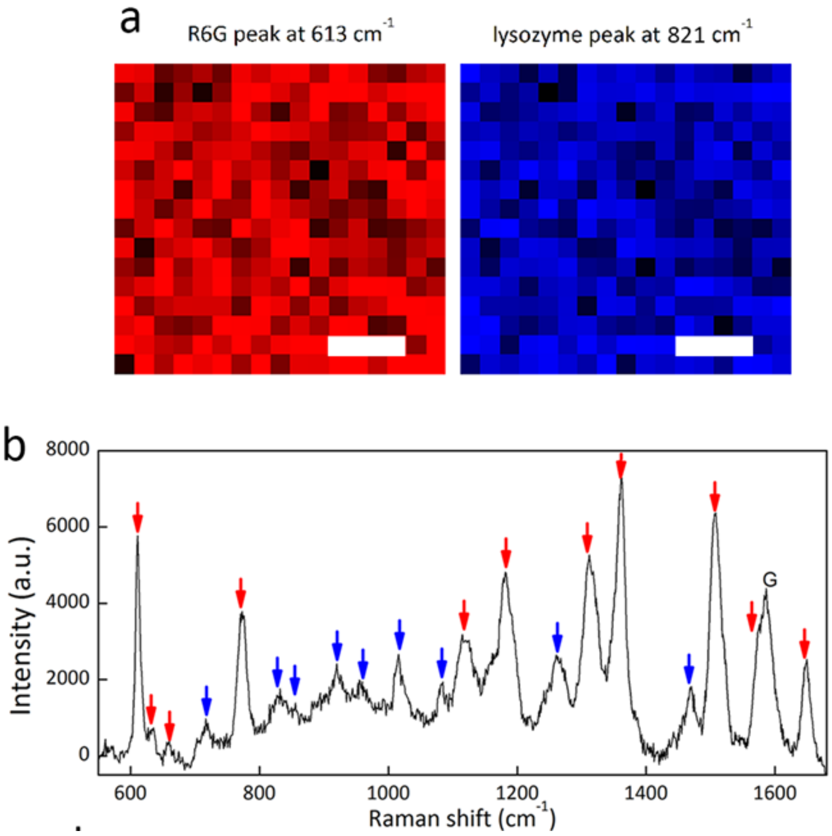

Figure 5.5: Spatial resolved Raman intensity mapping and selected spectra of R6G and lysozyme bianalyte mixture solutions on hybrid platform at 10^{-8} M concentration. **(a),** The R6G peak at 613 cm^{-1}(red) and lysozyme peak at 821 cm^{-1}(blue) are mapped respectively. **(b),** In the spectrum the Raman vibration modes assigned to R6G are marked with red arrows and those assigned to lysozyme are marked with blue arrows. Scale bar: 8μm.

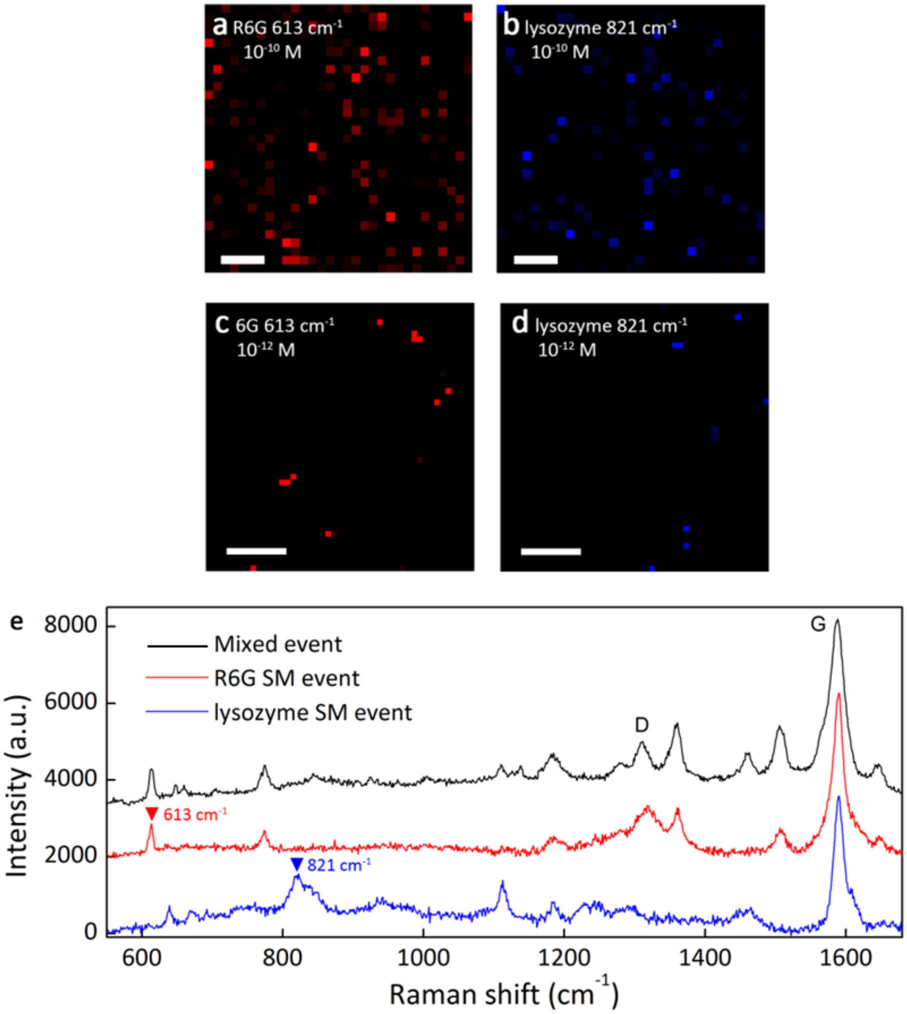

Figure 5.6: Spatial resolved Raman intensity mapping and selected spectra of R6G and lysozyme bianalyte mixture solutions on hybrid platform at 10^{-8} M concentration. **(a),** The R6G peak at 613 cm^{-1}(red) and lysozyme peak at 821 cm^{-1}(blue) are mapped respectively. **(b),** In the spectrum the Raman vibration modes assigned to R6G are marked with red arrows and those assigned to lysozyme are marked with blue arrows. Scale bar: 8μm.

Raman intensity mappings of R6G band at 613 cm^{-1} and lysozyme band at 821 cm^{-1} at 10^{-10} M and 10^{-12} M concentrations are shown in **Figure 5.6a-d**. When solution concentration is further reduced, percentage of overlapping R6G-lysozyme signal significantly decreases, and breakdown of ensemble averaging spectra occurs when single molecule regime has been reached (**Figure 5.6e**). We observed signal purely composed of SERS spectrum of one type of molecule, shown as a rather isolated pixel in the mapping. At extreme dilution, the spatial coincidence of an analyte molecule with the hot spots of the hybrid platform will be the key to detect molecular signal. Following the argument of Le Ru and Etchegoin [225], the bi-analyte nature of target molecules serves as strong evidence that the spectrum of one certain analyte from an individual pixel is attributed to single molecule.

5.3.2 EM and CM for R6G and Lysozyme SERS

We analyzed different vibrational modes of R6G and lysozyme deposited on Au tip substrate with and without graphene. The assignments of R6G and lysozyme SERS peaks can be found in **Table 5.1** and **Table 5.2** separately. Comparing the SERS spectra of R6G on graphene/Au tip structure and Au tips at molecular concentrations 10^{-10} M and 10^{-12} M in **Figure 5.7**, we observed discrepancy in the graphene induced enhancement to R6G peaks. Such discrepancy in enhancement becomes more significant at 10^{-12} M concentration that the 613cm^{-1} peak is enhanced by over four times while the 613cm^{-1} peak is enhanced by less than two times.

Table 5.1. Vibration mode dependent enhancement and assignment of Raman peaks in SERS spectra for R6G [259]

SERS Peaks	Tentative	Average enhancement

(cm^{-1})	**assignment**	**($I_{G/Tip}/I_{Tip}$)**
613	δ(C-C-C)ip	10
775	δ(C-H)op	5
1187	δ(C-H)ip	2
1311	ν(C-C)$^+$, ν(C-N)	6
1360	ν(C-C)$^+$, ν(C-N)	6
1506	ν(C-C)	4
1577	ν(C-O-C)	8
1645	ν(C-C)	4

Table 5.2. Vibration mode dependent enhancement and assignment of Raman peaks in SERS spectra for lysozyme [261]

SERS Peaks (cm^{-1})	**Tentative assignment**	**Average enhancement ($I_{G/Tip}/I_{Tip}$)**
821	tyrosine	3
849	tyrosine	3
922	ν(C_α-C-N)	5
974	tyrosine	4
1060	ν(C-N)	9
1110	ν(C-N)	8
1261	Amide III	3

1432	$\delta(CH_2)$	2
1466	$\delta(CH_2)$	2

* The ν(X-Y) is a vibration mode assigned to an X-Y bond stretching vibration, δ denotes deformation coordinate, ip denotes in-plane and op denotes out-of-plane.

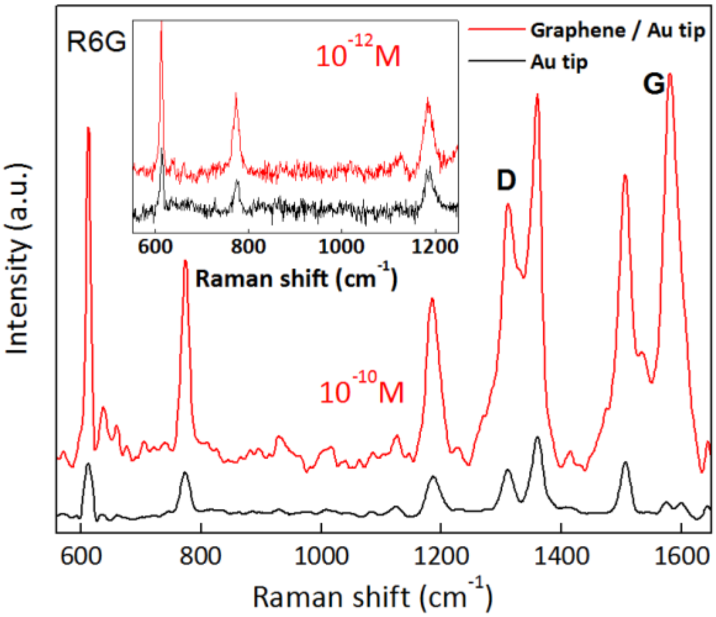

Figure 5.7: Raman spectra of R6G on graphene hybrid structure and Au tips at molecular concentrations 10^{-10} M and 10^{-12} M.

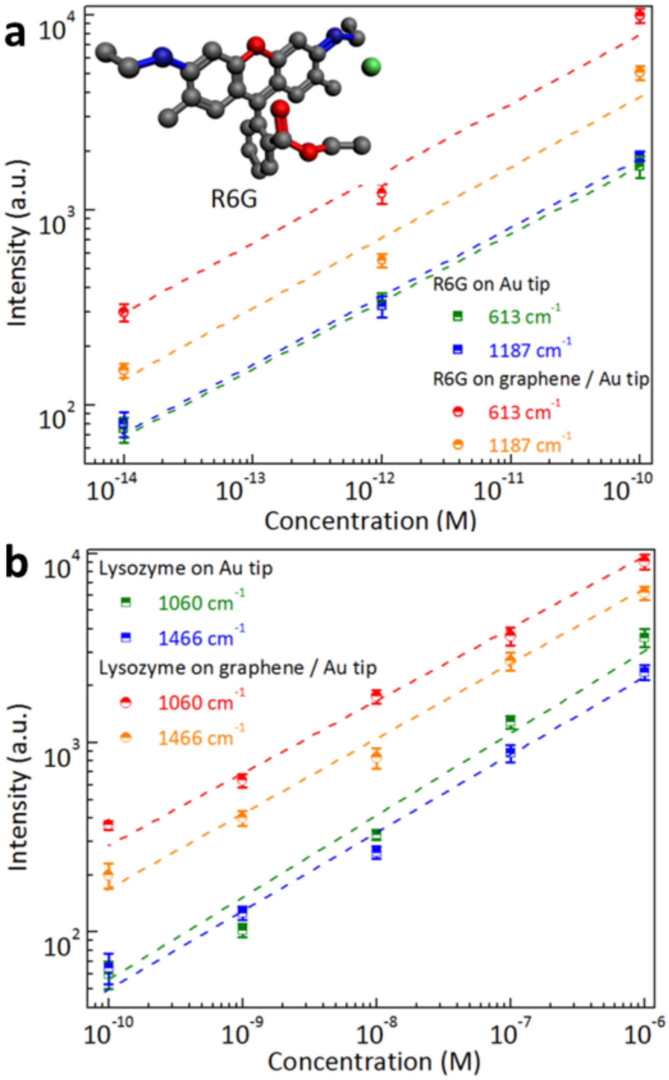

Figure 5.8: (a), The Raman intensity of R6G peaks at 613 cm^{-1}and 1087 cm^{-1} on graphene hybrid structure and Au tips separately, as a function of the molecular concentration, in log scale. **(b),** Raman intensity of lysozyme peaks at 1060 cm^{-1} and 1466 cm^{-1} on graphene hybrid structure and Au tips separately, as a function of the molecular concentration, in log scale.

Figure 5.8a shows a comparison of the R6G peaks at 613cm^{-1} and 1187cm^{-1} on graphene/Au tip and Au tip substrate respectively at various concentrations. The peak at

613cm^{-1} is assigned to the C-C-C deformation in-plane vibration and the peak at 1187cm^{-1} is assigned to the in-plane vibration of deformed C-H bonds [258,259]. They are slightly shifted from the typical 612cm^{-1} and 1185cm^{-1} position due presumably to the extremely high local electric field associated with the plasmonic resonance [260]. The 613cm^{-1} peak intensity is enhanced by a factor of 10, while the 1187cm^{-1} peak intensity is only enhanced by a factor of about 5 for a R6G concentration of 10^{-10} M. Similar behavior exists for lysozyme [261]. As shown in **Figure 5.8b**, the band at 1060cm^{-1} is enhanced more than the peak observed at 1466 cm^{-1}.

The dependence of the enhancement factor for the various vibrational modes is shown quantitatively in **Table 5.1** and **5.2**. The peak at 613cm^{-1} together with the 1577 cm^{-1} peak assigned to C-O-C bond stretching vibration show the highest enhancement ($I_{G/Tip}/I_{Tip}$ ~8). The peaks at 1311, 1360, 1506 and 1645 cm^{-1} assigned to C-C stretching modes show 4-6 fold enhancement. The peak at 775 cm^{-1} assigned to the out-of-plane vibration of deformed C-H bonds shows an average enhancement of 4-6 times. Among all peaks, the peak at 1187 cm-1 exhibits the lowest enhancement(~1-3 times). For lysozyme, the band at 1060 cm^{-1} assigned to the vibrations of ν(C-N) is about 3-fold more enhanced than the δ(CH_2) vibration mode [262] observed at 1466 cm^{-1}.

These observations allow us to propose the following possible mechanisms for the SERS chemical enhancement attributed to graphene-molecule interaction. Firstly, the 2-10 times enhancement for all vibration modes partly result from charge transfer between molecules and graphene. Charge transfer occurs when graphene Fermi level being located in between the HOMO and LUMO of molecules including R6G [234] (**Figure 5.9a-b**). Secondly, aromatic molecules prefer to stack in parallel to the π-bonds of graphene due to the preferred π-π stacking leading to enhanced resonant energy transfer [263]. In our experiments of lysozyme, the absence of peaks assigned to the symmetric ring-breathing vibration mode (exist only when benzene rings stand up or at least being tilted with respect to the surface) [261] reflects the flat orientation of aromatic amino acid residues in lysozyme. Both charge transfer and resonant energy transfer effects will be stronger when molecules are closer to the surface. In the case of charge transfer, the increased separation between negative and positive charges leads to an increase in molecular polarizability that has been associated with larger Raman scattering cross-sections [264].

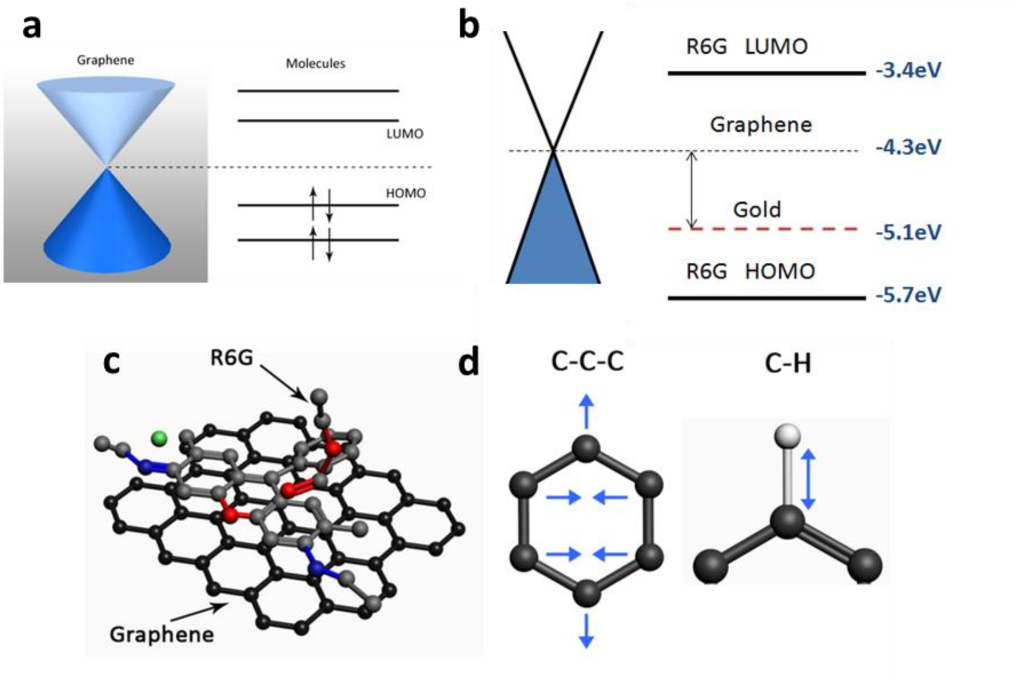

Figure 5.9: (a), Energy level diagram of graphene – molecule interface: charge transfer occurs when graphene Fermi level locates in between the HOMO and LUMO of molecules. **(b),** Illustration of the Fermi level of the system in R6G detection. **(c),** Schematic of a R6G molecule lying parallel to graphene surface. **(d),** Schematic of in-plane deformation C-C-C vibration mode and in-plane deformation C-H vibration mode of R6G molecules.

Furthermore, the basic chemical structures of R6G are similar to that of graphene, thus the in-plane deformation C-C-C vibrational mode will be further enhanced due to the vibrational coupling between the molecules and graphene. In contrast, such effects are absent for the deformed C-H in-plane vibrational mode (**Figure 5.9c-d**). This explains the more pronounced enhancement of the 613cm^{-1} peak assigned to the in-plane deformation C-C-C vibration. The behavior of the enhancement factors being dependent on the geometry of the molecules is a distinct characteristic of chemical mechanisms of SERS.

Then we present spatially resolved Raman data to assess the relative importance of EM enhancement to the overall SERS enhancement (**Figure 5.10**). Comparing the Raman intensity mapping of R6G 613cm^{-1} peak with that of the graphene G peak (**Figure 5.10a inset**), we find that the hotspots coincide. **Figure 5.10a** shows the Raman spectra of R6G at three spots on the graphene hybrid platform, two of them are from the hotspots in the mapping. **Figure 5.10b** shows the Raman intensities of R6G 613cm^{-1} peak and 1187cm^{-1} peak as a function of graphene G peak intensity. The intensities of the R6G characteristic peaks correspond linearly to the graphene G band intensity.

The lysozyme – graphene peak intensities from a series of spectra of a line scan over one of the hotspots are shown in **Figure 5.11**, which also shows the same linear dependence. The linear dependence spans significantly over 3 orders of magnitude. The observations of synchronized enhancement of the molecular and the graphene Raman peaks serve as strong evidence that the significant local EM field enhancement from the Au nanostructures is the major contribution to the dramatically enhanced Raman signals, in agreement with other SERS studies.

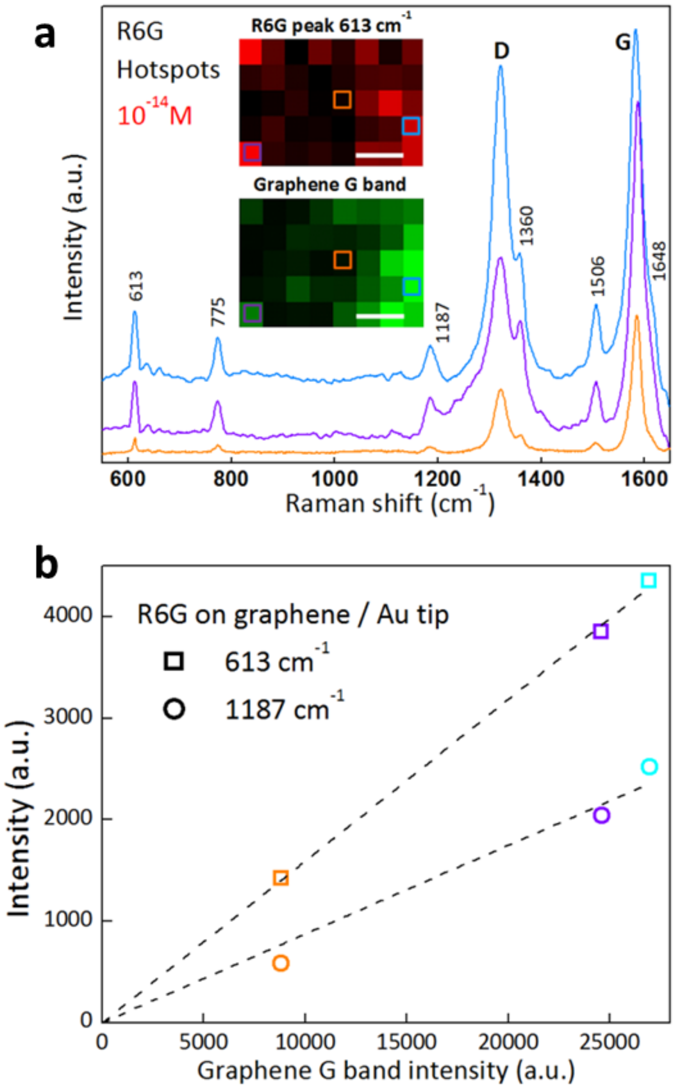

Figure 5.10: (a), SERS spectra for 10^{-14} M R6G on graphene hybrid system taken from three spots from the inset Raman mappings in the same color squares. The inset of a is composed of Raman intensity mapping of R6G peak at 613 cm^{-1}(red) and Raman intensity mapping of graphene G band (green), scale bar, 2 μm. **(b),** Raman intensities of R6G peaks at 613 cm^{-1} and 1187 cm^{-1} separately as a function of graphene G band from the three spectra shown in **(a).**

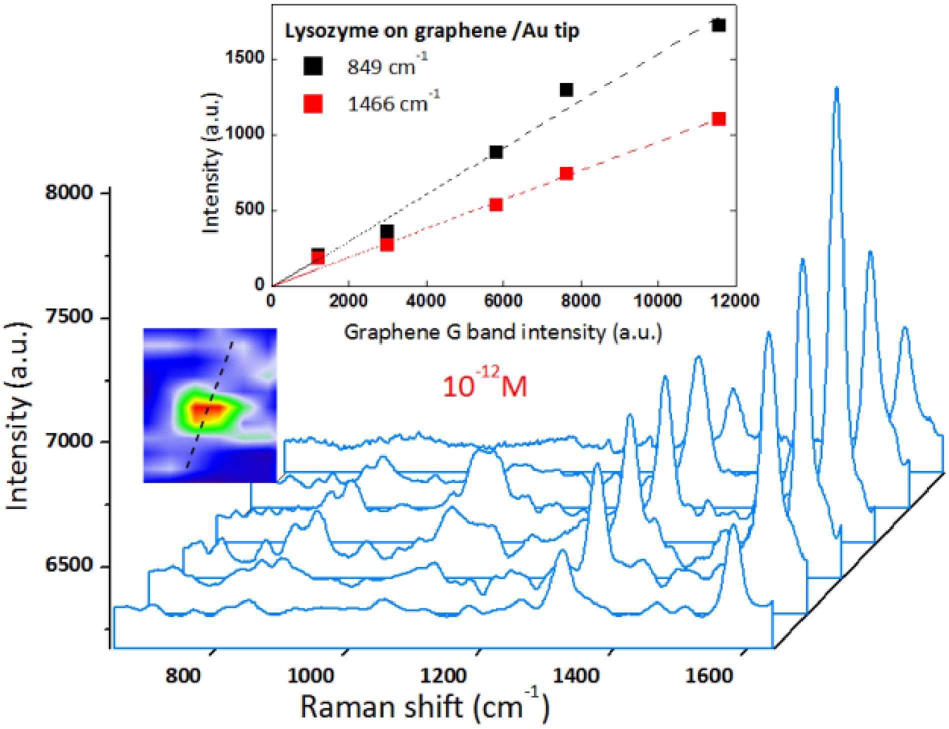

Figure 5.11: A series of Raman spectra from a line scan across a lysozyme SERS hotspot. The spectral interval is 500 nm. Inset: Raman intensities of lysozyme peaks at 849 cm^{-1} and 1466 cm^{-1} separately as a function of graphene G band from the spectra shown in Figure 5.11.

5.3.3 SM-SERS of Neurotransmitters

Both SERS of dopamine and serotonin was achieved of concentration levels down to 10^{-10} M setting records in the label-free detection of the two important neurotransmitters. **Figure 5.12a** and **Figure 5.12b** show the average Raman intensities of dopamine and serotonin deposited on graphene-Au tip heterostructure at various molecular concentrations. The lowest concentration at which spectra can be unambiguously resolved is 10^{-10}M for both dopamine and serotonin. This value is the highest sensitivity ever reported in the literature to our knowledge.

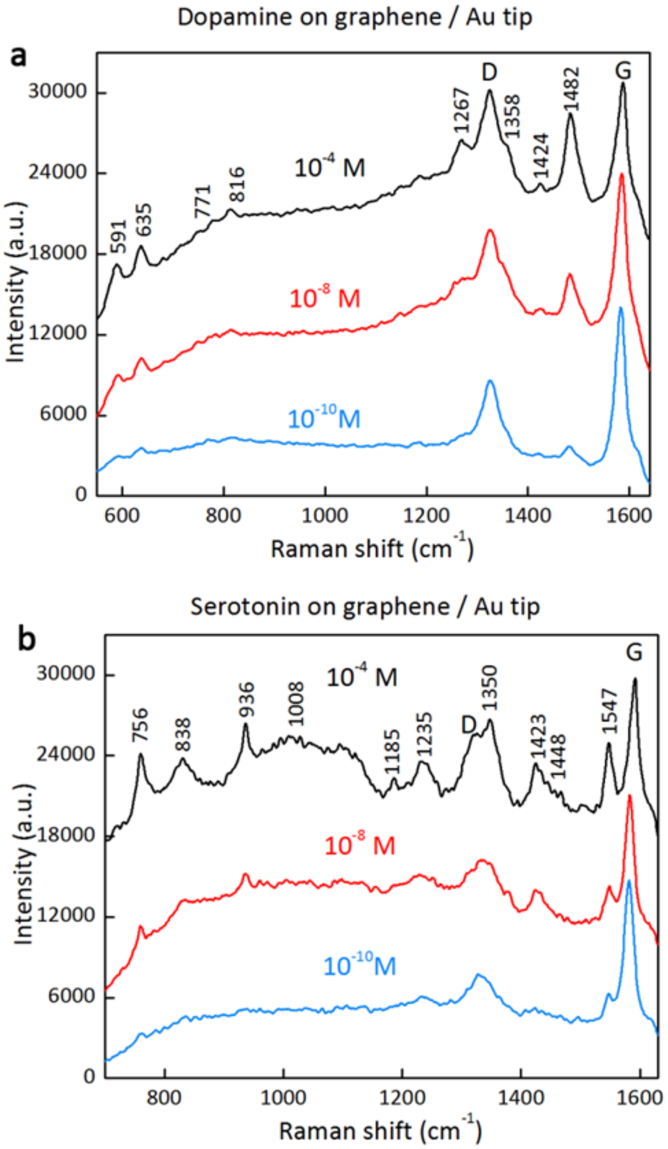

Figure 5.12: Raman spectra of neurotransmitter molecules on graphene hybrid structure with 3 different concentrations (10^{-4} M, 10^{-8} M, 10^{-10} M,) **(a),** Dopamine. **(b),** Serotonin. The laser excitation wavelength is 633 nm.

. The assignments of dopamine and serotonin SERS peaks can be found in **Table 5.3** and **Table 5.4** separately. For example, the Raman peak for dopamine locates at 1482 cm^{-1}, which is assigned to phenyl C=C stretching mode has a noticeably larger enhancement factor than the peaks assigned to other dopamine vibration modes. While for serotonin, the peaks located at 1423 cm^{-1} and 1547 cm^{-1}, which are assigned to indole ring vibrations [265] have experienced the highest enhancement. Such preferential enhancement for ring related modes is believed to stem from chemical enhancement rendered by graphene [266]. The π−π interactions between graphene and ring structures in dopamine as well as serotonin are believed to be a major contributing factor [263]. As shown in **Figure 5.14**, when the concentration is reduced to 10^{-10} M, the most easily-recognized Raman peak left are that of the 1482 cm^{-1} peak of dopamine and the 1423 cm^{-1} and 1547 cm^{-1}peaks of serotonin.

Table 5.3: Vibration mode assignment of Raman peaks in SERS spectra for dopamine [270]

SERS Peaks (cm^{-1})	**Tentative assignment**
591	C-H rocking
635	Phenol O-H op bending
771	Ring breathing
816	Aromatic C-H def op
1267	phenolic C-O stretching

1358	C-H ip bending
1424	ip CH_2 scissoring
1482	phenyl C=C stretching

Table 5.4. Vibration mode assignment of Raman peaks in SERS spectra for serotonin [271]

SERS Peaks (cm^{-1})	Tentative assignment
756	Indole ring breathing
936	O-H op deformation; C-H op deformation
1008	Benzene ring breathing
1185	C-H ip deformation
1253	C-C and C-N stretching in pyrrole
1350	C-N stretching, indole ring vibration
1423	C=C, C=N ip vibration in pyrrole
1448	Pyrrole ν(N–C=C) , benzene δ(CH)
1550	pyrrole ring stretching ν(C=C)
1620	C=C stretching

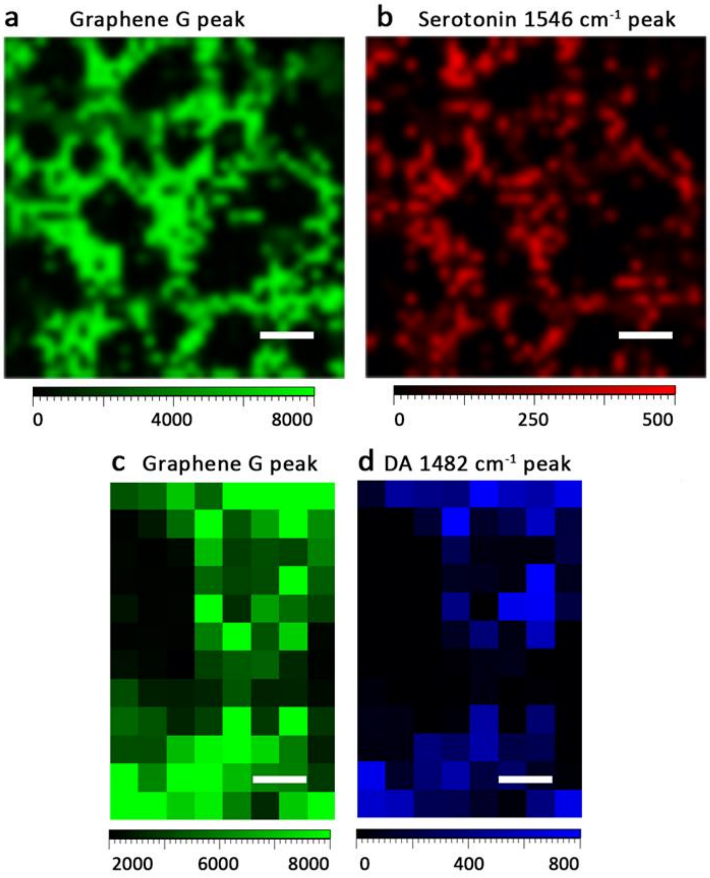

Figure 5.13: (a-b), Raman intensity mapping of graphene G band (green) and Raman intensity mapping of serotonin peak at 1546 cm^{-1}(red) of the same area, scale bar, 10 µm. **(c-d),** Raman intensity mapping of graphene G band (green) and Raman intensity mapping of dopamine peak at 1482 cm^{-1}(red), scale bar, 2 µm.

As indicated in **Figure 5.13a-b**, the hotspots for serotonin 1547 cm^{-1}peak and graphene G peak coincide with each other within the spatial resolution of micro-Raman. This feature can be appreciated by comparing their Raman intensity mappings over large area. The co-location also exists for dopamine 1482 cm^{-1} peak and graphene G peak. The direct correlation between molecule Raman peak intensity and graphene G-band intensity implies that the observed enhancements are due predominantly to EM enhancement. This observation is of special significance to the use of SERS for detecting trace amount of target molecules. Such application is hindered in practice for most plasmonic structures due mainly to difficulties in locating hotspots. Hot spots over hybrid platform can be precisely marked by graphene peak intensity mapping as discussed before thereby significantly reduce the time required during subsequent measurement of trace amount of target molecules.

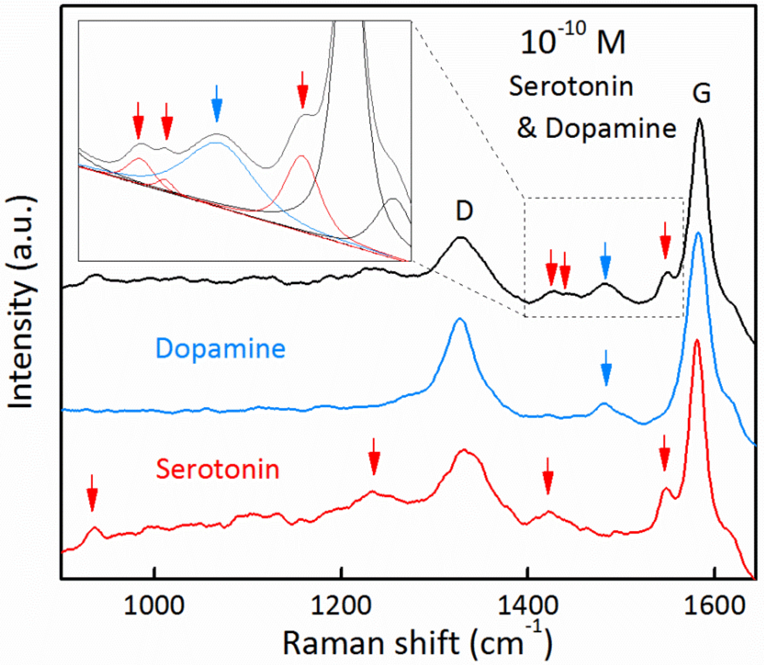

Figure 5.14: Raman spectra of 10^{-10}M serotonin and dopamine on heterostructure: Bi-analyte mixed event: black. Dopamine single molecule event: blue. Serotonin single molecule event: red.

BiASERS test of dopamine and serotonin has been conducted to establish single-molecule sensitivity of hybrid platform (**Figure 5.14**). Aqueous solutions of dopamine and serotonin respectively of the same concentration are dispersed over hybrid platform. The frequency of both dopamine and serotonin SERS spectra being present at the same hot spot decrease monotonically with decreasing concentration. At 10^{-10} M level, we observed spectral response from over 90% of SERS hot spots to be that of either dopamine or serotonin, but not both thereby firmly establishing the single-molecule detection capability of hybrid for dopamine and serotonin.

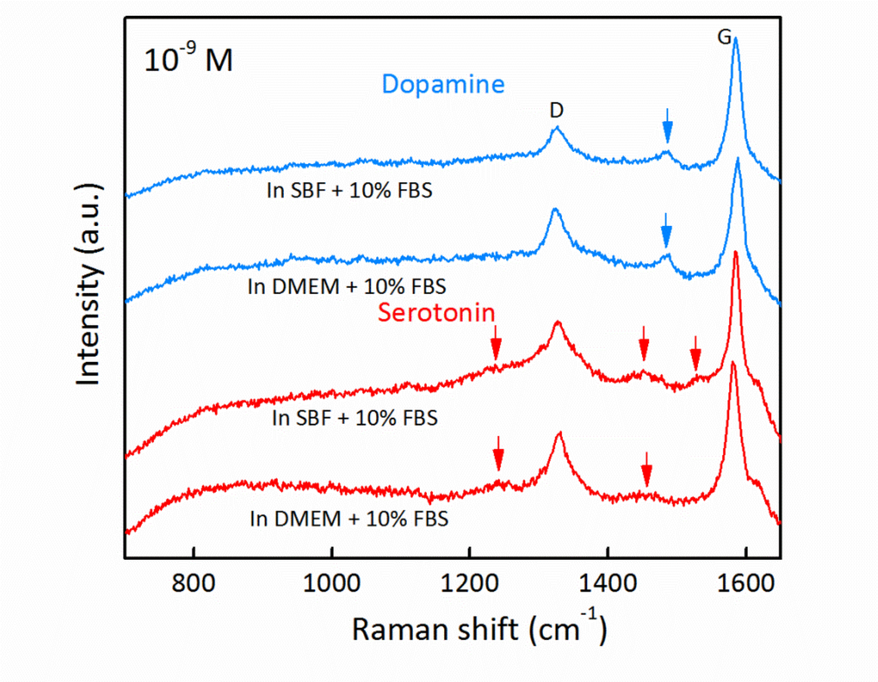

Figure 5.15: Raman spectra of 10^{-9} M dopamine (blue) and serotonin (red) dissolved in SBF supplemented with 10% FBS and DMEM supplemented with 10% FBS, respectively.

To mimic the real biological environment with the interference from a variety of biomolecules (e.g. serum proteins) in the background, we conducted SERS study of dopamine and serotonin dispersed in either cell culture medium (Dulbecco's modified Eagle's medium (DMEM) with 10% Fetal Bovine Serum (FBS)) or simulated body fluids (SBF) with 10% FBS. Interference from background molecules blocks access to the hot spots with their relatively large molecular size. Such access hindrance has been shown to lead to signal degradation [268]. In our case, the sensitivity is reduced from the 10^{-10} M in water to 10^{-9} M in DMEM or SBF for both dopamine and serotonin (**Figure 5.15**). These results show that hybrid platform enables label-free detection of highly diluted dopamine and serotonin in simulated body fluid as encountered in typical *in vivo* environment. It holds the promise of becoming a highly useful tool for monitoring synaptic processes *in vivo*.

5.4 Conclusion

In this chapter the hybrid platform enables single molecule detection and provides a reproducible and uniform response. The hybrid platform enables pre-locating hotspots to increase detection efficiency. It allows us to realize sub-10^{-12} M detection of R6G and lysozyme and to improve the detection limit of dopamine and serotonin to 10^{-9} M in simulated body fluid background. The addition of graphene also allows us to determine separately chemical enhancement (CM) and electromagnetic enhancement (EM) in a semi-quantitative fashion. The result indicates that EM is the dominant contributor with CM adding another order of magnitude to the large SERS enhancement factor.

In conclusion, the hybrid platform boasts three unique features compared to the more conventional plasmonic structures. First, the monolayer van der Waals material (vdW) such as graphene protects the metallic structure from degeneration due to the commonly encountered chemical reaction such as oxidation. It has been shown that the Raman enhancement factor of the commonly used Ag nanoparticles degrades by over 50% in a couple of weeks [269]. Second, the Raman peaks of graphene serve as a gauge of the near-field EM-field intensity allowing for quantitative measurement of target molecules to be obtained. Third, chemical interaction between graphene and target molecules results in selective enhancement and/or prohibition of certain SERS modes.

In practical applications, the option of adding graphene to SERS active metallic surfaces will broaden the utility of such platforms by offering chemically inert surface that is easily refreshed after each test and also being resistant to the degradation of the metallic nano-structures. The sensitive detection is carried out in a label-free fashion with the co-presence of both dopamine and serotonin. Such capability promises potential applications to the study of neurotransmitters in synaptic process *in vivo*, representing a step forward in enabling in-depth studies of neurological processes including those closely related to brain activity mapping (BAM).

The unique feature of bio-chemical finger-printing of Raman spectroscopy, which greatly reduces false-positive detection, combined with the capability of quantitative measurement makes the hybrid SERS platform a rare and very powerful experimental technique in clinical applications. Our approach and the results will go beyond simple single molecule detection to facilitate understanding of the basic mechanisms of SERS, and open up new opportunities in developing and revolutionizing the applications of graphene in biomedical diagnostics, analytical chemistry, as well as biological sensing and imaging.

6

SERS Quantification Using the Hybrid Platform

6.1 Introduction

6.1.1 SERS Enhancement Factor (EF)

A major goal of SERS is to apply its remarkable sensitivity and specificity in bioanalysis. Although various SERS systems have been successfully developed, SERS based quantification remains to be problematic. Determination of SERS enhancement factors (EFs) afforded by a SERS system is one of the most important issues. Current SERS EFs are obtained on the basis of comparing SERS from an analyte molecule with non-SERS Raman scattering of the same analyte molecule [273]. Quoted values of SERS EF of similar SERS systems may differ from each other by several orders of magnitude due to the ambiguous definition of parameters in SERS EF and the difficulties in retrieving the parameters correctly. The SERS EF proposed for single molecule detection ranges from 10^7 [272] to 10^{14} [24,25] using the similar SERS systems.

Theoretically SERS EF is divided into EM and CM components according to its mechanisms:

$$\text{SERS EF} = \text{EF}_{EM} \times \text{EF}_{CM} \tag{6.1}$$

To describe the EM part of SERS $|E|^4$-approximation [273] is commonly used. For simplicity we can ignore the Raman shift and consider the EM part of SERS EF as

$$\text{EF}_{EM} \approx \frac{|\mathbf{E}(\omega_L)|^4}{|\mathbf{E}_0(\omega_L)|^4} \tag{6.2}$$

where ω_L and $\mathbf{E}_0$ is frequency and electric field of the incident exciting laser, $\mathbf{E}$ is the local electric field which is strongly affected by plasmonic response and is much higher than incident field $\mathbf{E}_0$. Chemical enhancement is usually considered as an analyte specific perturbation (a factor of 10) to EM part of SERS EF.

In the practical experiments, SERS EF is defined as the ratio of SERS signal intensity to the Raman signal intensity that is obtained for exactly the same molecule in the absence of the SERS substrate, with all other conditions identical [274]. To this end we have

$$\text{EF} = \frac{I_{SERS} / c_{SERS}}{I_{RS} / c_{RS}} \tag{6.3}$$

where I_{SERS} is the SERS intensity of analyte in solution with known concentration of c_{SERS}, I_{RS} is the Raman intensity of analyte in solution with much higher concentration

c_{RS} under the same conditions (the same Raman spectroscopic setup). This is also called analytical EF. One disadvantage of the analytical EF originates from the volume concentration of analyte c_{SERS} since SERS is a surface process. To remedy this problem the SERS substrate EF is introduced as

$$\mathrm{EF} = \frac{I_{SERS} / N_{Surf}}{I_{RS} / N_{Vol}} \tag{6.4}$$

where N_{Vol} is the number of analyte molecules contributing to bulk Raman signal, N_{Surf} is the number of absorbed analyte molecules contributing to SERS Raman signal.

Two main challenges prevent researchers from obtaining accurate SERS EF. First, it is difficult to precisely determine the number of analyte molecule contributing to SERS and non-SERS respectively. Using SM-SERS the number of analyte molecule for SERS could be set as 1. However, determining the number of analyte molecule contributing to non-SERS Raman scattering remains to be challenging. Second, obtaining non-SERS Raman activity of analyte under exactly the same experimental conditions is challenging. System-to-system variations widely exist in SERS EF estimation and the EF can be inflated by several orders of magnitude when c_{SERS} and c_{RS} are determined differently. The intrinsic limitations thus make SERS EF of little significance in evaluate a SERS platform.

6.1.2 Quantifying SERS Analyte Concentration

Development of novel sensitive techniques for biomolecule detection and analysis [275-279] is crucial to the advancement of early-stage disease diagnosis. As a subdiscipline of analytical chemistry, bioanalysis covers the quantitative measurement of biotics and xenobiotics and in biological systems. It is essential to employ well-established and fully validated techniques to yield reliable results. US Food and Drug Administration (FDA) guidelines for bioanalytical method validation include requirements on specificity, precision, stability, calibration curve and quantification limit [280] (**Table 6.1**).

Table 6.1: US FDA Guidelines of Bioanalytical Method Validation

Type of Tests	Description	FDA Guidelines
Accuracy	The closeness of mean test results obtained by the analytical method to the actual concentration of the analyte.	A minimum of three concentrations in the range of expected study sample concentrations is recommended. The mean value should be within 15% of the nominal value except at LLOQ (+/-20%).
Specificity	The ability of an analytical method to differentiate and quantify the analyte in the presence of other components in the sample.	Analysis of blank samples of the appropriate biological matrix (plasma, urine, or other matrix) should be obtained from at least six sources. Ensured at LLOQ.
Precision	The closeness of individual measures of an analyte when the procedure is applied repeatedly to multiple aliquots of a single homogeneous volume of biological matrix.	A minimum of three concentrations in the range of expected study sample concentrations is recommended. The precision determined at each concentration level should not exceed 15% of the coefficient of variation (CV) except for the LLOQ, where it should not exceed 20% of the CV.
Recovery	Detector response obtained from an amount of the analyte added to and extracted from the biological matrix, compared to the detector response obtained for the true concentration of the analyte.	Recovery experiments should be performed by comparing the analytical results for extracted samples at three concentrations (low, medium, and high) with unextracted standards that represent 100% recovery.
Calibration Curve	The relationship between instrument response and known concentrations of the analyte.	Method validation experiments should include a minimum of six runs conducted over several days, with at least four concentrations (including LLOQ, low, medium, and high) analyzed in duplicate in each run.
Quantification Limit	The lowest standard on the calibration is LLOQ. The highest standard will define the Upper Limit of Quantification	The LLOQ should be established using at least five samples. The analyte response at the LLOQ should be at least five times the response compared to blank response. Analyte peak should be identifiable,

(ULOQ)	discrete, and reproducible, and the back-calculated concentration should have precision that does not exceed 20% of the CV and accuracy within 20% of the nominal concentration.

SERS, capable of single molecule detection and multiplexed analysis, holds great potentials for applications in bioanalysis [281-284]. SERS allows for the observation of subtle spectroscopic phenomena that were not hitherto accessible due to its superior fingerprint specificity and single molecule sensitivity. Nanoscience and nanotechnology have enabled extremely high SERS enhancement factors in various systems. Recent advances in nanotechnology have led to plentiful analytical applications of SERS and generated insights in analyte quantification by SERS. As shown in **Table 6.2**, detection and quantification of various analyte molecules inclusive of nicotine [285] and glucose [286] has been achieved. In these studies quantification is acquired by building the connection between analyte concentration and analyte SERS peak intensity.

Table 6.2: Summary of Current SERS Quantification Progress

Target Analyte	SERS Platform	Dynamic Range	Reference
Rhodamine 6G	Self-assembled monolayer (SAM)-coated Au colloids	0.1-5 uM	[287]
Rhodamine B	Metallic glassy nanowire arrays	1nM-10uM	[288]
Rhodamine 6G; Crystal violet	Graphene oxide and AgNP hybrids	1nM-10uM	[289]
Nicotine	Polymer-stabilized Ag colloids	0.1-10 ppm	[285]
Nicotinamide	AgNPs	0.1-1mM	[290]

Adenine	Ag sol	0.1-0.9uM	[291]
Carbohydrates (Glucose, lactose etc)	Rhodamine-based tagged Ag colloids	1 nM-5μM	[292]
DNA	Fluorophore-labeled Ag/AuNPs	1-100 nM	[293]
Glucose	AuNPs/Au colloids modified by horseradish peroxidase and glucose oxidase	0.5-32 mM	[294]
Mucin protein MUC4	Sandwich immunosorbent assay with functionalized AuNPs	0.01-10 μg/mL	[295]
C-reactive protein (CRP)	BCIP-SERRS-ELISA	0.2-100 ng/mL	[296]
Antigen (mouse IgG)	Sandwich immunosorbent assay with SERS tagged Ag colloidal	0.1-3 ng/mL	[297]

The SERS intensity observed is assumed to be proportional to the concentration of target analyte in the probed volume and thus enables a direct calibration of the absolute SERS peak intensity against concentration. However, SERS is a complex process whose mechanisms are still under debate. The pre-assumed linear dependence of SERS intensity to number analyte molecules present in probed volume may only be valid in very limited concentration range. Heterogeneity of the SERS active substrates leads to significant variation in the SERS peak. The degree of aggregation, instrumental factors as well as interaction between plasmonic structure and molecules also affect the SERS signals. Consequently SERS quantification using conventional SERS systems suffer from short quantification range, poor reproducibility, serious spot-to-spot variation, and lack of universal adaptability. A reliable SERS quantification method, leveraging the superiority of SERS in sensitivity and specificity, is in desperate need to facilitate the clinical transition of SERS.

We present an ultra-sensitive graphene-plasmonic hybrid platform for statistically reliable SERS quantification. The two-dimensional nature makes graphene a built-in hotspot marker and opens up new opportunities to extract information on exact location and enhancement of hotspots. Fine-tuned fabrication process ensures the reproducibility of the substrate. The high uniformity in both shape and distribution of the Au tips over large substrates minimizes variation in the scanning area during Raman measurement. We proposed a novel definition of SERS EF based on graphene-plasmonic system. The graphene based EF eliminates the system-to-system variation of SERS EF from 10^7 to 10^{14}. The well-established knowledge of hotspots will greatly benefit the study of SERS EM enhancement mechanisms.

Moreover, the hybrid platform enables statistically reliable quantification with linear dynamic range over three orders of magnitude using spatially resolved Raman mappings. We demonstrate quantification for both dye molecule R6G and colon cancer cell. Employing graphene as SERS internal reference provides more insights into SERS quantitative parameters. The graphene based platform exploits the full potential of SERS to be a powerful bioanalytical tool.

Chapter 6.2 demonstrates a novel graphene based SERS EF definition. Chapter 6.3 presents the accurate quantification of hotspots in terms of enhancement and distribution using SERS intensity mapping of graphene in the hybrid platform. Chapter 6.4 details the statically reliable quantification of SERS analyte using spatially resolved Raman mapping.

6.2 Graphene Based SERS EF

$|E|^4$ Approximation for EM Based EF

The $|E|^4$ approximation for SERS enhancement provides a very useful yardstick estimate for experimental SERS enhancement in a single molecule located at x_0. It is commonly used as a figure of merit to evaluate theoretical models with experiments. In our work, the EM field enhancement is ~100 at hot spots per FDTD calculation, which is in line with the consensus of the field. An EM based EF of 10^8 is expected. Considering the additional chemical enhancement factor of ~10, we have the total SERS EF estimated as ~10^9.

Concentration Based Analytical SERS EF

Using the most commonly used SERS EF definition in equation 6.3, which is called analytical EF, we estimate the SERS EF of R6G using the hybrid platform. The SERS of R6G on the hybrid platform is measured by diluting R6G solution of 10^{-12} M. A droplet of ~2μL solution is deposited on the hybrid system and it diffuses on the surface to form a blot with diameter of ~2mm. As reference, a 2μL droplet of 0.01 M R6G solution is deposited on graphene covered flat gold surface for Raman scattering (RS) measurement. 633 nm laser with a beam radius size of ~1 μm is used for measurement. To eliminate the fluctuations of EM enhancement, graphene is used as internal reference and the I_{SERS} and I_{RS} are normalized with graphene G band intensity. From the SERS and RS spectra shown in **Figure 6.1**, it could be noted that the I_{SERS} of 10^{-12} M R6G SERS and I_{RS} of 10^{-2} M R6G are comparable. So we have concentration based analytical SERS EF ~10^{11}.

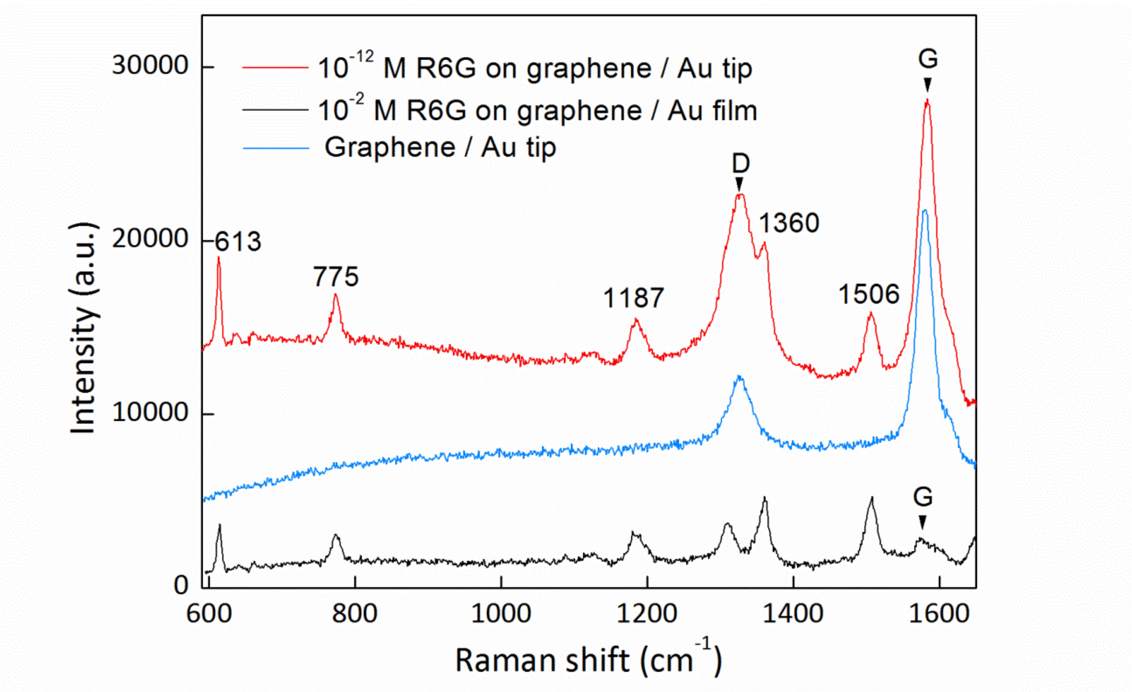

Figure 6.1: SERS of 10^{-12} M R6G on graphene-Au tip hybrid platform (red), SERS of graphene on the hybrid platform (blue) and Raman of 10^{-2} M R6G on graphene covered flat Au film.

Single Molecule SERS EF

In single molecule SERS achieved using bi-analyte method, it is statistically convincing to claim that the contribution of SERS originates from only one molecule. Using the modified SERS EF in equation 6.4, the SERS EF can be estimated by

$$\mathrm{EF} = \frac{I_{SERS} / N_{SERS}}{I_{RS} / N_{RS}} \qquad (6.5)$$

Where N_{RS} is the number of probe molecules contributing to bulk Raman signal, N_{SERS} is the number of probe molecules contributing to SERS Raman signal, which is 1 in the case of single molecule SERS, I_{SERS} and I_{RS} are the normalized intensities of selected Raman peaks in SERS and Raman spectra. In **Figure 6.2**, a single molecule SERS event of R6G is confirmed using BiASERS.

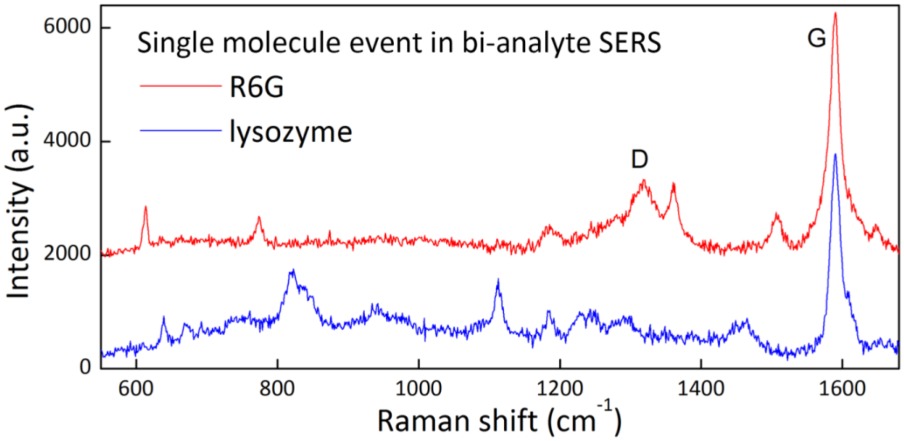

Figure 6.2: Single molecule SERS events of R6G and lysozyme in bi-analyte measurement of 10^{-12} M solution.

The probe molecules are assumed to disperse uniformly on the substrates. The specimens for SERS and RS are prepared and detected in the same conditions. The number of molecules under detection can be estimated as

$$N = N_A MV \frac{S_{laser}}{S_{sub}} \tag{6.6}$$

Where N_A is Avogadro constant, M is the molar concentration, V is the volume of solution droplet, S_{sub} is the size of the substrate and S_{laser} is the size of the laser spot. For RS event, the concentration is 10^{-2} M and the droplet volume is 2μL, thus the N_{RS} is estimated as ~10^8. The average EF is estimated as ~10^7.

Considering the SERS EFs varies from 10^7 to 10^{11}, we attribute the four orders of magnitude difference to the dimensionality difference, namely, the concentration based analytical EF estimate the analyte number in probed volume while for remedied EF the number is estimated in probed area. It could be noted that the deciding factors are highly dependent on the probe molecules, the SERS systems and the measurement setup. Consequently the error for the estimated SERS EF could be two or three orders of magnitude.

Graphene Based SERS EF

The devoid of a SERS EF estimation that can be universally applied to different SERS systems makes it impossible to compare their SERS enhancement capabilities. Graphene provides an ideal platform to quantify SERS enhancement. The graphene based SERS EF can be simply defined as

$$GEF = \mathrm{I}_{\mathrm{GSERS}} / \mathrm{I}_{\mathrm{GRS}} \tag{6.7}$$

Where $\mathrm{I}_{\mathrm{GSERS}}$ and $\mathrm{I}_{\mathrm{GRS}}$ are the intensity of graphene G or 2D peaks on substrate with SERS active nano-features and on the same substrate without any SERS structure.

The graphene based EF could be further remedied to reflect the enhancement at a hotspot. While the signal of conventional Raman spectra being derived from a probed area of several μms in size, Raman signals from plasmonic enhancement comes predominantly from electromagnetic field concentration that is extremely localized to typically nanometer region [298,299]. Thus we introduce an adjusted definition of graphene Raman enhancement factor for graphene-plasmonic composite structures:

$$\mathrm{EF} = \frac{\mathrm{I(patt)/A(hotspot)}}{\mathrm{I(unpatt)/A(excitation\ spot)}} \tag{6.8}$$

Where I(patt) is the graphene Raman peak intensity including G and 2D bands measured at hotspot on the patterned Au tip region. A(hotspot) is the area of a typical hotspot. The I(unpatt) graphene Raman peak intensity measured at Au film without patterned plasmonic features. The A(excitation spot) is the area of the excitation spot. For 633nm, we take it the as the spot with diameter of 1μm. As shown in graphene SERS intensity mappings, the hotspots are highly localized region within area of 10 nanometer scale [300, 301].

In the current study, we assume that the signal enhancement is from plasmonic resonance, which has been established to be due almost entirely to EM contribution, with the possible chemical contribution adding a factor no larger than 10. In addition, EM wave simulation has established that the "focusing effect" of EM field as electric-field hot spots is only active within a range of nanometers. Raman signal from tipped surface is composed of two parts: the non-resonant part from the entire illuminated area of 1μm x 1μm, and the resonant part from hot spot of the 5 nm x 5 nm area. Part one is assumed to be the same as that from flat Au or SiO_2 region which contribute to 1/1000 of the signal we measured. The other 99.9% of the signal comes from an area of 5 nm x 5 nm. To calculate the enhancement factor, this signal should be divided by the corresponding non-resonant signal from the same 5 nm x 5 nm area, or alternatively the typical signal intensity multiplied by a factor of (1 μm x 1 μm)/ (5 nm x 5 nm). Here is the additional 10^4 factor of enhancement. Together with the apparent intensity enhancement 10^3, we obtain SERS EF of 10^7 for total enhancement at the hotspot.

Graphene based SERS EF estimation shows tremendous benefits. First, graphene conforms to the metal nano-features closely thus its peak enhancement reflects the SERS enhancement at exactly same spot. Secondly, graphene Raman fingerprints are well established and highly reproducible. It overcomes the limitation widely existed to probe molecules that position, width and intensity of their SERS peaks changes a lot at low concentrations for detection. Thirdly, graphene eliminates the uncertainties related to deciding number of probe molecules and separating non-SERS Raman signal from SERS signal, which lead to several orders of magnitude difference in final SERS EFs estimated.

6.3 Plasmonic Hotspots Quantification by Graphene

The nature of graphene as a two-dimensional continuous membrane with prominent Raman features makes it ideal to quantify SERS hotspots when incorporated with plasmonic SERS structures. The data was represented as enhancement histograms to develop the understanding of the hotspot distribution. Unlike metal nanoparticles, the hybrid platform incorporating uniformly distributed Au tips supports reproducible SERS signals and guarantees statistically reliable SERS intensity quantification. Spatially resolved Raman has been employed to examine the distribution of hot spots as shown in **Figure 6.3**. The ratio of graphene 2D band intensity on Au tip to intensity on Au film is actually an indicator of the enhancement factor since SERS signal intensity is proportional to the local EM field. The very hot spots where the ratio I_{2D}(Au tip)/ I_{2D}(Au film) no less than 400 are marked in red. It can be noted that the density of hotspots with graphene 2D peak enhancement over 400 is as high as 20% of the total area measured in **Figure 6.4**.

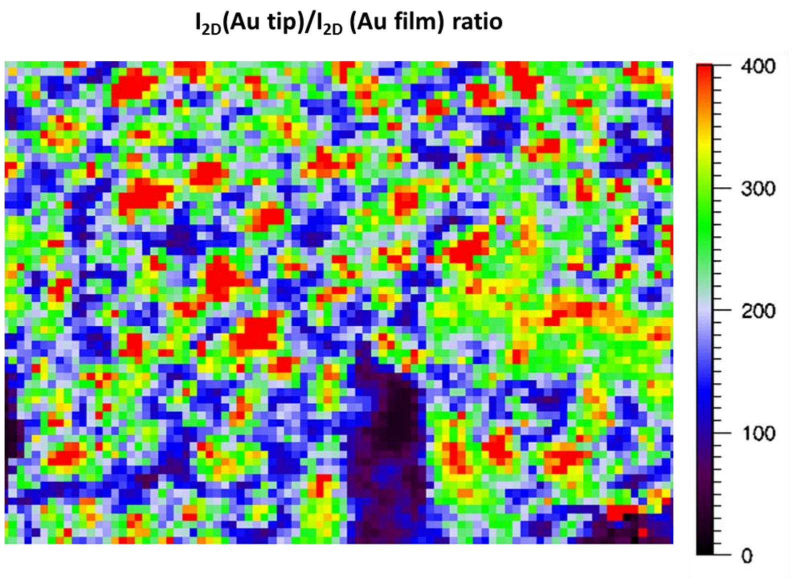

Figure 6.3: Spatially resolved Raman intensity ratio mapping of graphene 2D peak intensity on Au tip to the intensity on Au film. The step size is 1μm* 1μm and each pixel corresponds to a graphene SERS spectrum.

Figure 6.5 shows the histogram of the 2D peak enhancement indicating the distribution is a normal distribution with average enhancement above 200. The results demonstrate that the key role of the periodic Au arrays in providing reproducible hotspots over long range.

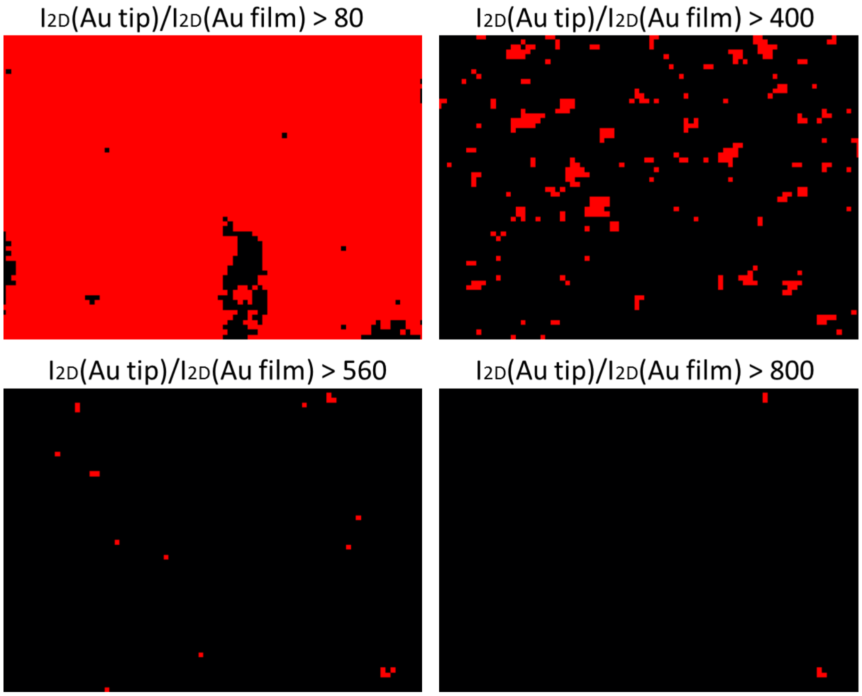

Figure 6.4: Mappings showing different hotspots of different enhancement factors indicated by ratio I_{2D}(Au tip)/ I_{2D}(Au film

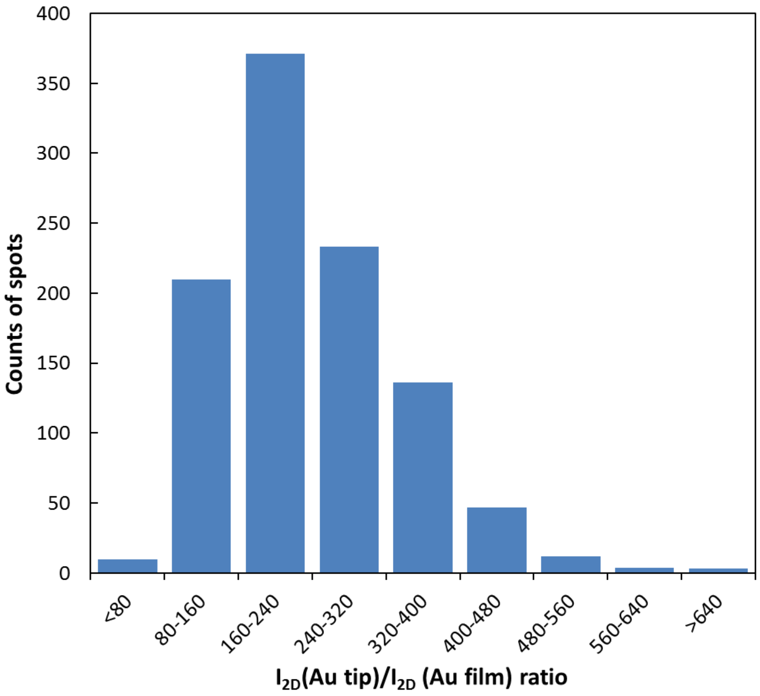

Figure 6.5: Histogram of ratio I_{2D}(Au tip)/ I_{2D}(Au film).

6.4 Quantifying SERS Analyte *via* Spatially Resolved Raman Mapping

The hybrid platform is exposed to target analyte solutions at different concentrations. The analyte molecules are immobilized on the substrate by water evaporation of solution in clean condition. The deposition of molecules on the platform is a very simple label-free process without any biomarker and binding procedure needed. The hotspots where local electromagnetic fields can be enhanced by 100 times are located in between tips. Analyte molecules trapped within the hotspots exhibit a pronounced SERS signal even with a small number of molecules.

In SERS quantification using conventional systems, the analyte concentration is calibrated with intensity of analyte SERS peaks [302]. The intensity of SERS peak is dependent on multiple factors including the number of molecules at hotspot, the hotspot EM enhancement factor and molecule-surface interaction induced chemical enhancement. To eliminate the influence of EM enhancement, the SERS internal reference molecule is introduced to mark the nanoparticles and the analyte SERS peak intensities are normalized to the internal reference peak. The biggest shortcoming is the fact that the EM enhancement of analyte molecules cannot be precisely represented by the enhancement of internal reference. More importantly, the quantification is based on the assumption that the number of analyte molecules at hotspot is linear to the analyte concentration. In practical SERS measurements the chance of such linear correspondence is very low. Consequently huge system-to-system variations exist in the quantification results using similar colloidal nanoparticle systems.

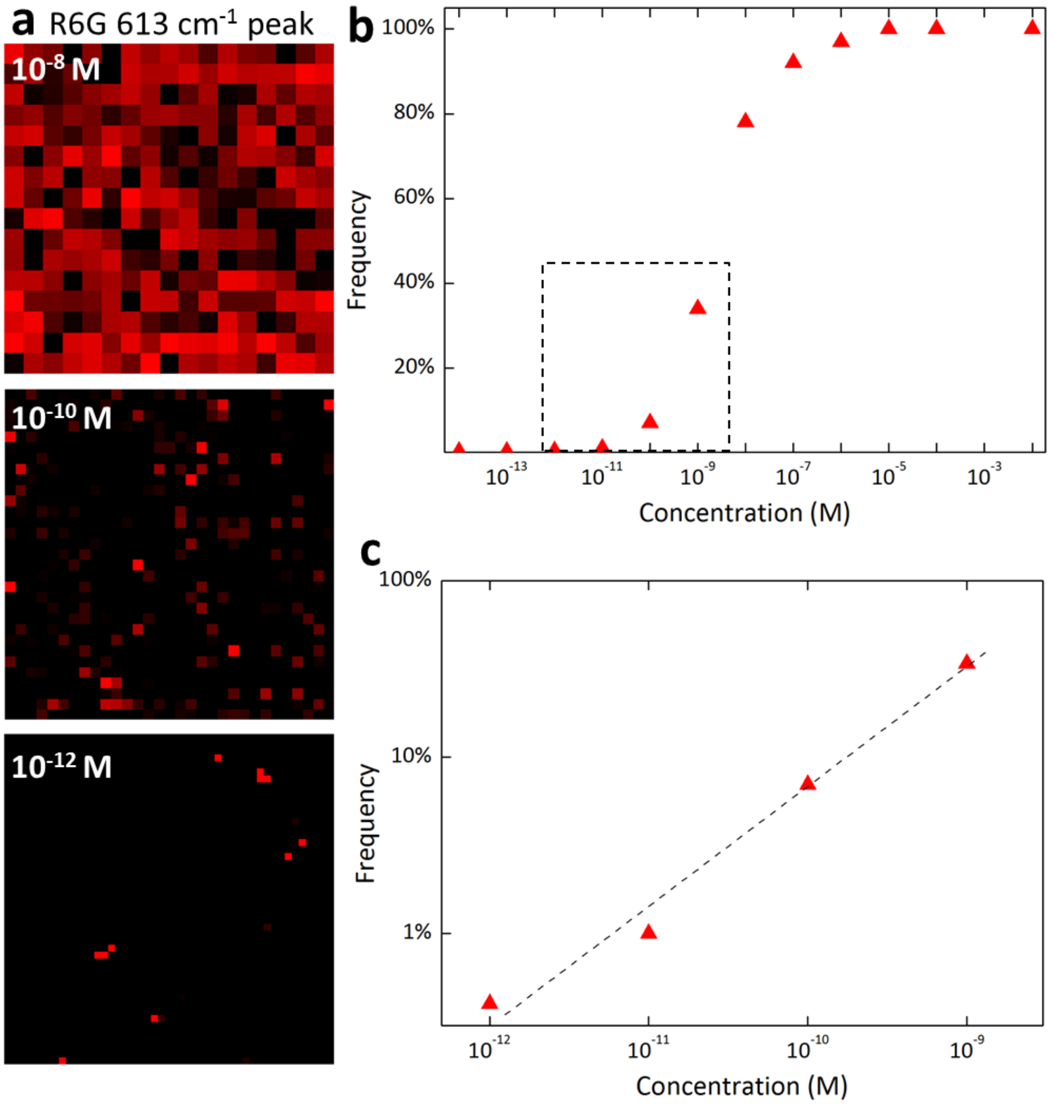

Figure 6.6: SERS quantification using spatially resolved Raman mappings. (a), The intensity mapping of R6G 613 cm^{-1} peak at concentration 10^{-8} M, 10^{-10} M and 10^{-12} M. The step size of the mappings is 1 μm *1 μm. **(b),** The concentration dependence of frequency of R6G SERS event in mappings. (**c**)**,** The log scale amplification of the area encompassed (dashed rectangle) in (**b**).

We proposed a statistically reliable SERS quantification method using spatially resolved Raman mappings. Relatively large-areas (~50 μm* 50 μm) spatially resolved Raman mappings of R6G on the platform were scanned at step size of 1μm to collect Raman spectra from each pixel 1μm* 1μm. The recorded data were displayed as heat maps rendering the Raman peak parameters including intensity, position, width, and intensity ratio by degrees of color. Mapping measurements over different areas were performed on the platform exposing to R6G solutions at concentrations varying from 10^{-2} M to 10^{-14} M. As shown in **Figure 6.6**, when the R6G solution was diluted from 10^{-8} M to 10^{-12} M, the number of spots showing R6G SERS declined accordingly. The probability of incidence that analyte molecules captured by hotspots, which is the origin of detectable SERS signals, is decreasing with analyte concentration. The average number of molecules per μm^2 deposited on the platform surface reduces from ~2500 at 10^{-8} M to ~0.25 at 10^{-12} M, thus leading to the reduction of the SERS frequency, which is defined as the percentage of spots exhibiting target molecule SERS among all spots measured in a mapping.

In **Figure 6.6b** the frequency of detectable SERS events in mappings is presented at various concentrations. **Figure 6.6c** shows the amplification of the dashed rectangle region in **Figure 6.6b** from 10^{-9} M to 10^{-12} M in log scale. The SERS quantification range is three orders of magnitude. Time frame is a constraint of the mapping of area and total number of spectra collected. In our measurement the time frame of Raman mapping at a concentration is limited in two hours with 1 s acquisition time. It could be noted that though the frequency stayed almost the same for analyte solutions with concentration below 10^{-12} M, the lower limit of quantification is far below 10^{-12} M due to the statistic nature of the method. Techniques including nano-fluidics can be integrated with the SERS platform to lower the quantification limit by trapping analyte molecules in SERS system in a more increase efficient way. Besides, the frequency of SERS events saturated at higher concentration end when the analyte molecules deposited are enough to cover the whole measured areas. The higher limit of quantification is dependent on the characteristics of analyte molecule and the SERS system as well.

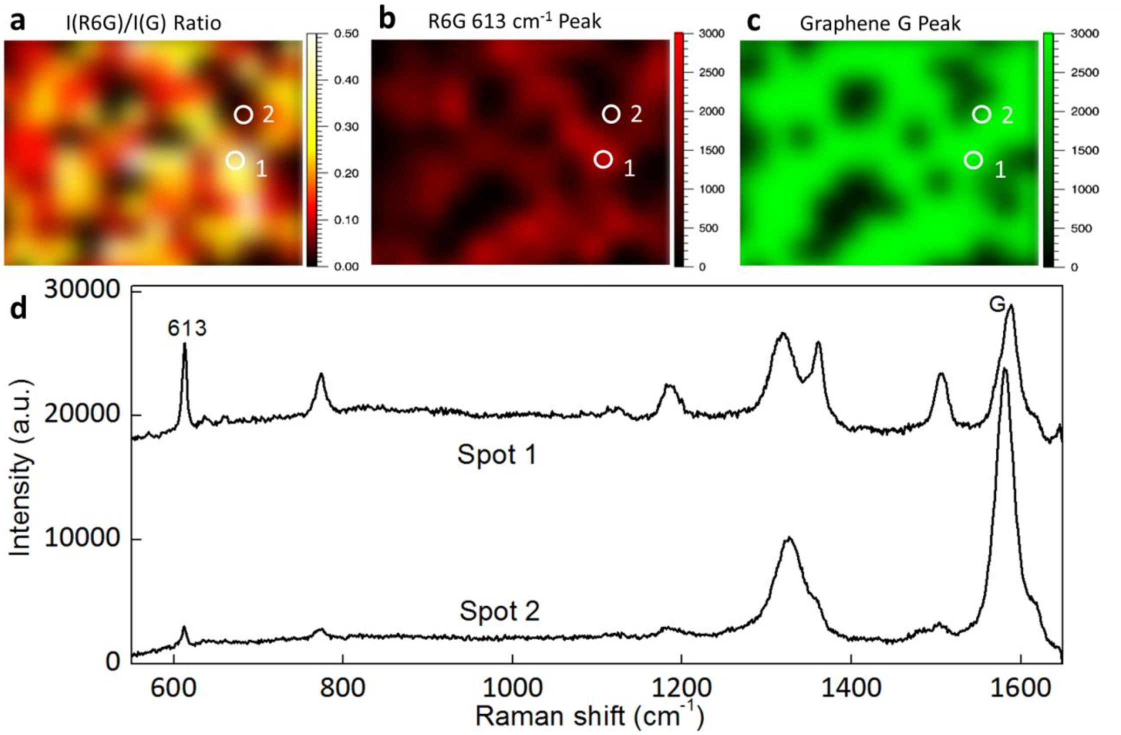

Figure 6.7: The spatially resolved mappings of 1 μM R6G deposited on the hybrid platform. (**a),** The intensity ratio mapping of R6G 613 cm^{-1} peak to graphene G peak. (**b),** The intensity mapping of R6G 613 cm^{-1} peak. (**c),** The intensity mapping of graphene G peak. (**d),** SERS spectra took at spot 1 and spot 2 indicated in the mappings.

Graphene, the built-in hotspot marker, serves as an ideal internal reference for SERS quantification applications. By normalizing analyte SERS peaks to graphene peaks, the EM enhancement can be eliminated so more information can be extracted to investigate SERS. **Figure 6.7a** shows the distribution of intensity ratio of R6G 613 cm^{-1} peak to graphene G peak at 1 μM. The variation in I(R6G)/I(G) ratio is as large as 10 times in **Figure 6.7d** (the ratio is ~1 at spot 1 and ~0.1 at spot 2). The ratio distribution could shed some light on the molecular density distribution. The signals obtained at high molecular concentration are ascribed to two components: SERS of molecules captured at hotspots and non-SERS Raman of excess molecules at non-hotspots. With the knowledge of hotspot and analyte molecule distributions via graphene SERS enhancement and graphene peak normalized analyte peak mappings, further studies could be conducted to separate and quantify the SERS contribution from non-SERS contribution.

Cell serves as good analogy with regard to the quantification. SERS of colon cancer at concentrations from 50 /mL to 10000 /mL was measured. The frequency of cell SERS events and average time frame for a successful detection are shown in **Figure 6.8.** At higher cell concentrations, our platform performs very efficiently in the time frame of seconds for a successful detection. But when the concentration reduces down below 50 cells/mL, nearly 10000 spots need to be mapped to locate one spot with cell SERS and it takes hours for a successful detection. Current micro/nano fluidic devices enable successful isolation of circulating tumor cells with concentration as low as 5 cells per mL blood. We would expect to realize the full potential of our platform when integrated with microfluidic devices as downstream analysis platform to extract detailed cellular information. The cell SERS will be detailed in Chapter 7.

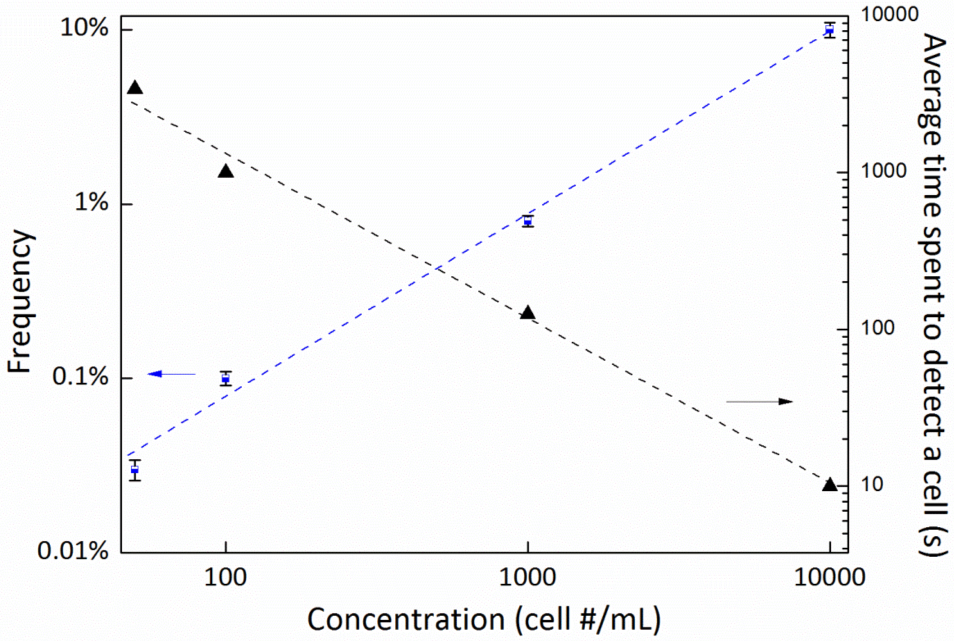

Figure 6.8: The concentration dependence of SERS event frequency and average time spent for a successful detection for colon cancer cells.

6.5 Conclusion

In this Chapter, we describe application of the reproducible and high-yield graphene-plasmonic hybrid platform to realize SERS quantification. The controversial definition of SERS enhancement factor has led to huge discrepancy in reported SERS EFs varying from 10^7 to 10^{14}. We propose a novel graphene based SERS EF (GEF) definition that is highly reproducible. The SERS EF could be directly estimated from graphene SERS without the presence of analyte molecules. The introduction of GEF significantly minimizes the influences of analyte molecules, the SERS systems and the measurement setup on the enhancement factor estimation.

The hybrid quantifies hotspots on the basis of employing graphene as built-in hotspot marker. With the platform we obtained statistically reliable SERS quantification using spatially resolved SERS mappings. The stable and reproducible approach established broad quantification dynamic range with extremely low quantification lower limit in principle.

In conclusion we demonstrate a graphene-Au tip hybrid platform to realize a novel SERS quantification method using Raman mappings. Graphene plays a crucial role in quantifying SERS hotspots and paves the path for defining SERS EF that could be universally applied to various SERS systems. Reproducible and reliable SERS quantification using the hybrid platform not only leverages the ultra-sensitivity but also minimizes the spot-to-spot variations. The platform, combined with techniques of analyte pre-concentration and multi-variate data analysis [303], can make SERS a powerful and reliable tool for biological and chemical analysis.

7

Applications of the Hybrid Platform in Biomedical Diagnostics

7.1 Introduction

7.1.1 SERS in cancer diagnostics

In 2014, about 136,830 cases of colorectal cancer are predicted to be diagnosed in the United States, and about 50,310 people are expected to die from the disease [304]. Among the colorectal cancer cases 96,830 are colon cancer. Thus cancer prevention and early detection are central to the American Cancer Society's mission and its 2015 goals [305]. Fecal occult blood test (FOBT), sigmoidoscopy and colonoscopy serve as the primary screening techniques in current medical practice in the United States [306]. Patients will undergo biopsy performed by surgery for definitive diagnosis of colon cancer when abnormality is detected. These invasive procedures are too expensive to allow for routine screening to support sufficient frequency for early detection. A non-invasive or minimally-invasive screening protocol performed at higher frequency with lower cost will lead to greatly increased overall survival rate and much reduced societal burden.

For commonly used diagnostic assay, the critical step is to selectively and sensitively recognize the target bio-specie or biomarker in a mixture of species [307,308]. Cancer biomarkers, such as tumor associated antigens, could signal the presence of cancer and predict the stage of tumor genesis as well. Biosensor is a bioanalytical device incorporating a bioreceptor and a transducer [309]. The bioreceptor of choice for protein detection is antibody. ELISA assays [310] carried out in multi-well plates (one well for a type of protein) yield picomolar detection limit. The dynamic range of ELISA is only 10^2 limited by the photobleaching and signal to noise ratio. The poor stability of antibody molecules makes long-term storage unfeasible.

Though fluorescence [311] has long been the tool of choice, SERS has been elevated as a promising contender. SERS overcomes the limitations of fluorescence in terms of broad emission spectrum and proneness to photobleaching [312]. Nanotechnology has become a prominent field of inter-disciplinary research for detection, diagnosis and treatment of cancer [313-316]. It hinges on the application of metallic, semiconductor and polymeric nanoparticles which have unique optical and structural properties absent in molecules. Consequently functionalization of nanoparticles with biological molecules is projected to lead to remarkable advances. With the development of progress has been constantly made on applying SERS in the fields of cancer imaging, diagnosis, early detection and targeted treatment.

Biomedical applications of SERS [317-319] have been widely investigated in recent few years. Raman spectroscopy provides detailed molecular fingerprints about a biological sample and thus capable of tracking the chemical changes that accompany cancer [320]. Raman spectroscopy has been used in *in vivo* skin cancer diagnosis to distinguish malignant from benign skin lesions with high diagnosis accuracy [321]. In cancer diagnostics, SERS shows the potential for clinical translation as a non-invasive tool for in vivo analysis of tumors, cancer imaging and circulating tumor cell (CTC) detection [322]. Using antigen labeled nanoparticles, a low detection limit of 50 circulating cancer cells/mL has been demonstrated [323]. Colloidal AuNPs tagged with targeting ligands and Raman reporter dye molecules have been extensively studied in cancer detection and imaging using SERS [324]. However, in such system SERS signals detected originate from the Raman reporter attached on the AuNPs instead of the cell. Cellular information provided by the indirect SERS signals is extremely limited and this may lead to false positive detection. Microfluidic devices [325] are promising in capturing CTCs but the further characterization of CTCs after isolation is still under development. Diagnosis accuracy is critical for CTC detection since blood sample from patient is limited (<10 mL) and only a few cells are available for detection. Thus downstream analysis tools to investigate and profile the isolated CTCs with high sensitivity and specificity will offer excellent opportunities to realize early-stage cancer diagnosis [326].

7.1.2 Principle components analysis (PCA) for SERS

Principle components analysis (PCA) [327] is a quantitatively reliable method used for dimension reduction to generate a new set of variables out of a large dimension of correlated data [328]. It eliminates the least contributing parts of the correlated data to reduce data redundancy. Each orthogonal principle component is a linear combination of the original variables. Principle components are the dominant eigenvectors of covariance matrix composed of combinations of original variables.

PCA has been advantageously applied to a number of spectral data-sets originated from Raman scattering, nuclear magnetic resonance (NMR), and fluorescence [329]. PCA is used to organize and classify the proteins based on their secondary structure. It is also recognized as a fundamental way to differentiate cells according to their biochemical features. The combination of SERS measurements and PCA analysis is effective in categorizing different SERS analyte on the basis of their biochemical features. PCA enables classification of SERS spectra in a more distinguishable way than visual examination of spectra.

7.1.3 Amyloid β

Alzheimer’s disease (AD) is a fatal neurological disorder with unclear cause and currently no cure. In the US, 13% of people older than 65 are afflicted, and the figure rises to 40% for those older than 85 [330]. Amyloid β peptide (Aβ) is the major constituent of the plaques, which are the diagnostic of AD [331]. The Aβ peptide, constituted of 39 to 42 amino acids, is cleaved from the C-terminal of amyloid precursor protein (APP) [332]. The most abundant Aβ fragments Aβ(1-40) and Aβ(1-42) are both neurotoxic.

The progress aggregation of Aβ protein fragments into β-sheet rich amyloid fibrils in neuron cells is one of the major hallmarks of AD [333]. It is of significant importance to investigate the detailed pathway of Aβ aggregation from monomer to β-sheet fibrils and to identify structure of various aggregation forms. Neurotoxic Aβ oligomers are loosely aggregated secondary structure in between monomer and β-sheet Aβ. The state-of-art characterization tools of protein structures are circular dichroism (CD) spectroscopy, nuclear magnetic resonance (NMR) spectroscopy and X-ray crystallography [334]. Compared with those methods, SERS has superior sensitivity and selectivity, which enable the detection and trace of structural transition of Aβ in small amounts [335].

SERS has attracted considerable attention as a non-invasive technique for cancer cell detecting and imaging due to high sensitivity and multiplexing capability. However, the commonly used anti-body labelled gold nanoparticles (AuNPs) immunoassays only support indirect SERS with very limited cellular information provided. Besides, the complex preparation process and the need of specific biomarkers hindered the clinical translation of SERS assays. In this Chapter we apply the hybrid platform as a non-destructive and label-free tool to detect and distinguish cancer cells in blood plasma background. The capabilities of the platform are demonstrated by colon cancer cell detection in simulated body fluid (SBF) with cell concentration down to 50 cells /mL. With graphene superimposed on Au tips we achieved much higher SERS yields of cells and detection sensitivities, thus realized the SERS directly from cellular biomaterials instead of indirectly from the Raman reporter tagged on SERS structures. Cancerous cells can be distinguished from non-cancerous cells on molecular level. Moreover, using peak correlation analysis we were able to classify the SERS peaks and determine peaks assigned to the same biomaterial. PCA was applied to demonstrate the high sensitivity and specificity of the platform.

Moreover, we explore the potentials of the hybrid platform in monitoring time-dependent configurational change of Aβ protein at micro-Molar concentration. The distinctive change in Aβ characteristic SERS peaks indicate the transition from Aβ monomers to oligomers. We believe the application of SERS in Aβ oligomer formation study will generate enormous insights based on the molecular vibration mode specific SERS peaks. The hybrid platform has the promise of being economical with instantaneous turnaround and thus be used as a routine screening approach. The extension of our hybrid platform to conventional SERS active systems such as ligands tagged AuNPs has potentials to facilitate clinical translation of SERS in cancer diagnosis.

Chapter 6.2 presents the sensitive diagnosis of colon cancer cells achieved by the hybrid platform, the critical role of graphene in sensing, and the PCA of cell SERS. Chapter 6.3 demonstrates the time dependent configurational change of Aβ protein at micro-Molar concentration realized by SERS.

7.2 Hybrid Platform for Cancer Cell Diagnosis by SERS

7.2.1 Distinguishing Colon Cancer Cell from Normal Cell

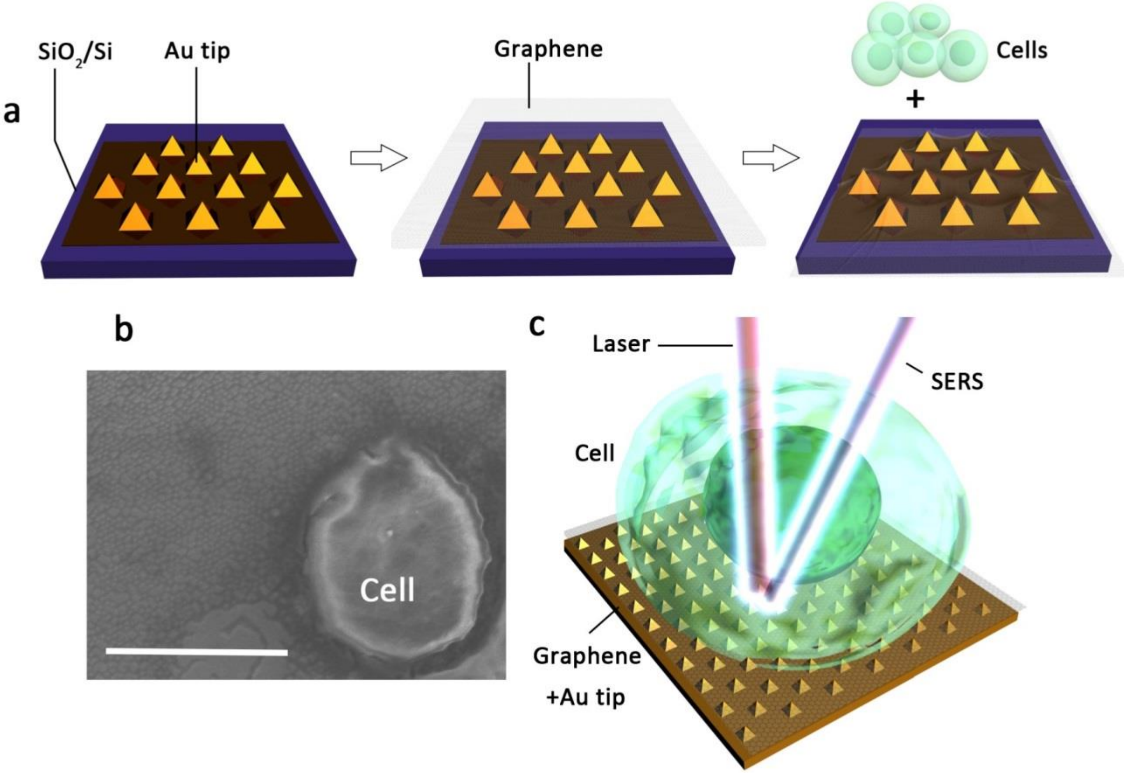

Figure 7.1: (a), Illustration of the hybrid platform for cancer cell detection; **(b),** SEM of a cancer cell on the hybrid platform, scale bar: 10um. **(c),** Illustration of cancer cell SERS.

Human colon cancer cells (P53--) and non-cancerous colon cells (P53++ wildtype) [336] cultured in simulated body fluid (SBF) were prepared at varying concentrations and deposited on the hybrid platform for SERS detection (**Figure 7.1**). **Figure 7.1b** shows SEM image of a captured cell on the substrate. Unlike previously reported SERS probes conjugated with antibodies, no labelling process is needed in this approach. Due to the ultra-sensitivity boosted by the substrate, the SERS feedback is achieved directly from the cellular content in the vicinity of the graphene/Au tip structure under detection. The laser beam used in SERS is of the size 1 μm * 1 μm, smaller than cell dimension of about 10 μm. The platform also enables spatially resolved Raman mapping to extract more cellular structural and environmental information. The G peak of monolayer graphene is used as SERS reference peak.

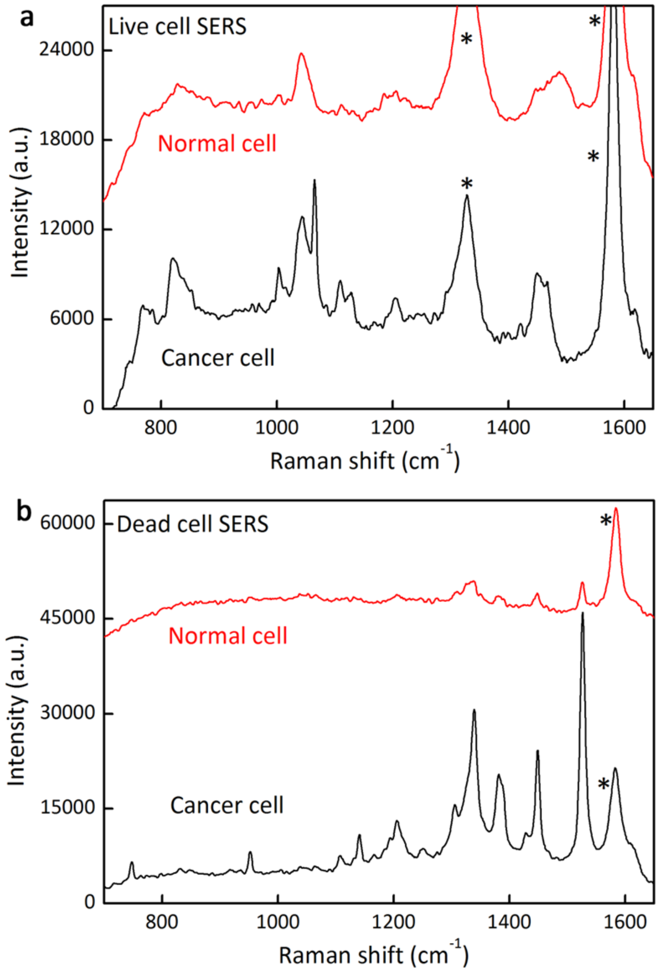

Figure 7.2: (a), Live and **(b),** dead cancer cell SERS and normal cell SERS

Table 7.1: Peak Assignments for Live Cancer Cell SERS [339]

Peak Center (cm^{-1})	Assignments
766	Proteins
820	Proteins
1004	Proteins
1041	Proteins
1066	Nucleic acids
1109	Proteins
1129	Lipids
1205	Proteins
1294	Lipids; Proteins; Nucleic acids
1450	Proteins; Nucleic acids
1468	Lipids

Table 7.2: Peak Assignments for Dead Cancer Cell SERS [340, 341]

Peak Center (cm^{-1})	Assignments
619	Proteins
747	Nucleic acids
952	Proteins
1109	Proteins
1140	Lipids
1204	Proteins
1305	Lipids
1337	Lipids; Proteins; Nucleic acids (CH_2/CH_3 mode)
1380	Lipids; Proteins; Nucleic acids (CH_3 mode)

1450	Proteins; Nucleic acids (C-H vibration)
1527	Nucleic acids

To evaluate the hybrid platform's capability to distinguish normal and cancerous cells, we investigated SERS of both live and dead cells using the graphene based hybrid platform. As illustrated in **Figure 7.2**, for both live and dead cells deposited on the platform, we observed that cancer cells show distinctive SERS spectral features and can be distinguished from normal cells. Spectral shifts identified in normal and cancerous cells reflect the biochemical changes during the cell apoptosis [337,338].

The peak assignments of cellular contents in both live and dead cells are shown in **Table 7.1** and **Table 7.2** respectively. Proteins, nucleic acids (DNA/RNA) and lipids contribute to majority of SERS peaks. For live cells, the very sharp peak located at 1066 cm^{-1} assigned to nucleic acids barely exists in normal cell SERS. Aside from the presence of the 1066 cm^{-1} peak, most peaks of cancerous live cells SERS have higher intensity than those of normal cells. Such peak intensity difference between normal and cancer cell SERS become more significant for dead cells. For cancerous dead cells, the intensity of 1527 cm^{-1} peak , which is assigned to nucleic acids, is over 10 times higher than that of normal dead cells. It has been reported that one of the most prominent changes occurs in cancer cells is increased cellular nucleic acid content [342]. However, aside from peaks assigned to nucleic acids, protein and lipids induced peaks of cancer cells also have stronger intensity. This could be originated from the difference in the cell surface structure. The cancer cells may interact with the surface in a slightly different way from the normal cells, thus leading to enhanced signals.

7.2.2 Critical Role of Graphene in Cancer Cell Sensing

To investigate the critical role graphene played in the cell SERS sensing, SERS spectra of cancer cells were obtained on the Au tips and graphene/Au tips separately (**Figure 7.3**). The SERS signals of cells deposited on Au tip surface are very weak with most peaks barely identifiable. In contrast, cells on graphene/Au tip substrate provide intensive SERS signals. We proposed several hypotheses to explain this phenomenon: first, the plasmonic enhancement is highly localized in the close vicinity of the nano-features. The adhesion of cells to Au surface is much weaker than adhesion to graphene surface [343], thus reducing the SERS enhancement significantly when cellular content failed to locate at hotspots; secondly, graphene provides biological compatible carbon surface that may interact with cell surface via π-π interaction and facilitate charge transfer, which lead to significant increase in cell SERS yield. The graphene selectively enhances SERS yield of peaks from bio-molecules 10-100 times in addition to the electromagnetic enhancement of plasmonic structure. The graphene based SERS enhancement (GERS) originates from both chemical interaction and charge transfer between graphene and target molecules.

The hypotheses have been evidenced by measurements of burst cells (**Figure 7.3 Inset**). When the cells were burst with cellular biomaterials uniformly distributed in the SBF solutions, we deposited the solution on the Au tips and graphene/Au tips separately and conducted SERS. The SERS feedback of cellular biomaterials is stronger than that of intact cells when measurements were conducted on Au tip surface without graphene. The difference between peak intensity of cellular biomaterials on Au tips and graphene/Au tips may also result from the graphene based chemical enhancement.

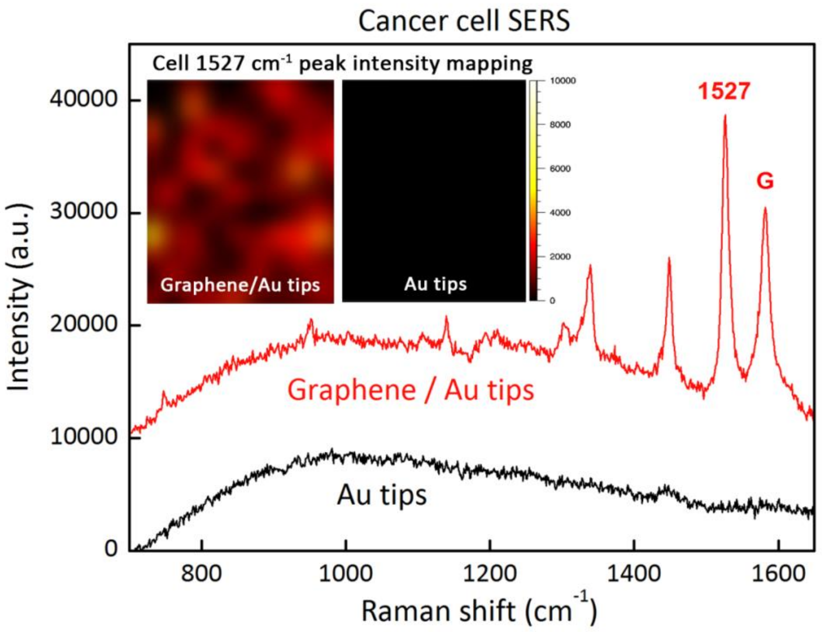

Figure 7.3: SERS of cancer cells on Au tips with and without superimposed graphene.

Imaging of a single cell can be achieved by spatially resolved Raman spectroscopy. **Figure 7.4** shows intensity mapping of peak 1527 cm^{-1} which is assigned to nucleic acids. **Figure 7.4a** and **Figure 7.44b** show respectively the mappings of normal cell and cancer cell. In **Figure 7.4c** there are the SERS spectra along the line scan across a cancer cell. In the mapping, the spots in red indicate highest intensity of nucleic acids peaks and define the nucleus of the cell. The SERS intensity of normal cells is about 10 times weaker than that of cancer cells. The shape of cancer cells is more irregular.

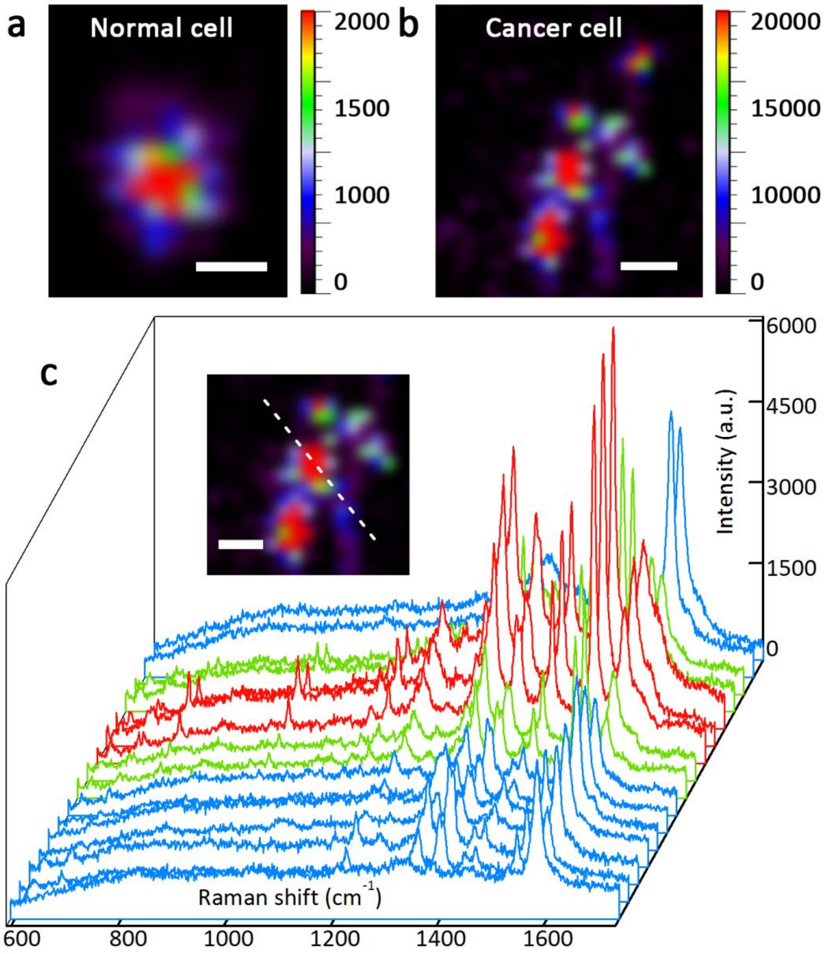

Figure 7.4: 1527cm^{-1} peak intensity mapping of **(a),** a normal cell and **(b),** cancer cells. Scale bar: 5um. **(c),** SERS spectra along the line across the cancer cell mapping. Scale bar: 5um. Raman step size 0.5um.

7.2.3 Highly Sensitive Detection of 50 Cells/mL

Efficiency is another critical factor for cancer cell diagnosis using SERS. Cell SBF solutions with concentrations varying from 10000 to 50 cells/mL are deposited on the platform for SERS. To search for a cell we began with large area mapping with map step

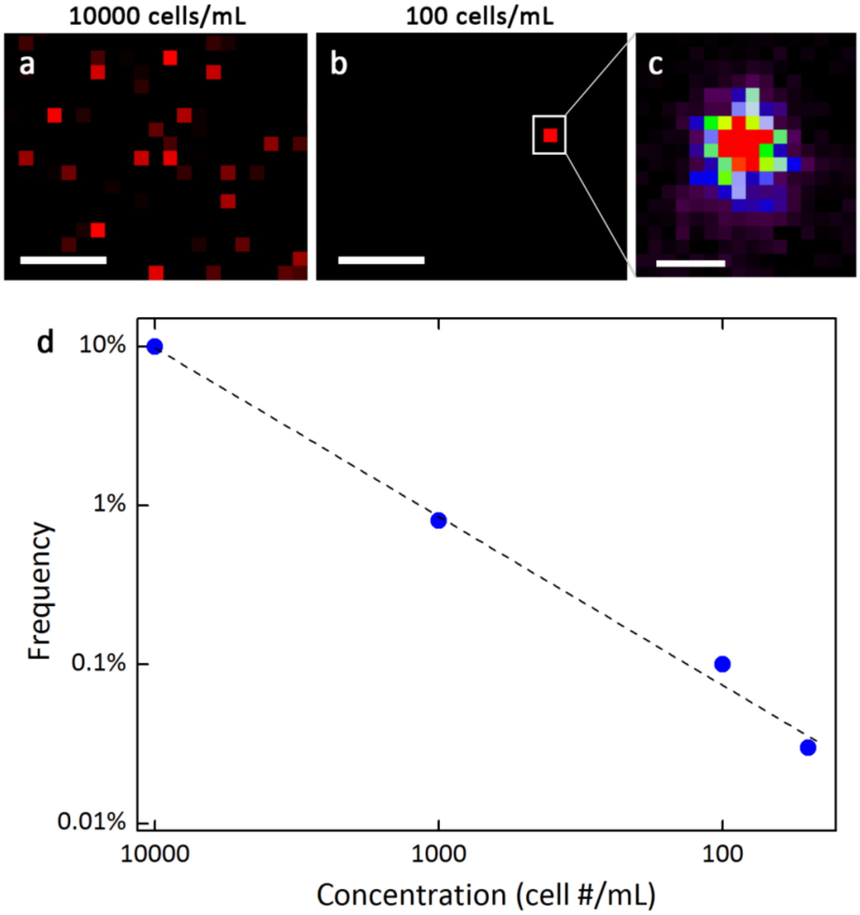

Figure 7.5: Cancer cell 1525 cm^{-1} peak intensity mapping of solutions with concentration **(a),** 10000 cells/mL and **(b),** 100 cells/mL. **(c),** The concentration dependence of SERS event frequency.

size set as 10 μm and acquisition time of a single spectrum set as 1s. The time frame for a scan of 1mm*1mm area is about 2 hours. Using a Raman setup capable of line-scan and lower spectral acquisition time could further shorten the scan time to even several minutes. The number of cell SERS incidences in a mapping is proportional to the cell solution concentration. As shown in **Figure 7.5a-b**, when the cell concentration dropped to 100 cells/mL, on average only several spots show cell SERS signals out of thousands of spots in a large area scan. When a spot has been identified with cell signal, we focus on the cell area and conduct a mapping with much smaller step (<1 μm) to obtain the profile of the cell (**Figure 7.5c**). **Figure 7.5d** shows the average frequency of a cell SERS incidence in a large area scan versus the concentration of cell solution. Here the frequency is defined the ratio of the number of cell spectra to the total number of spectra scanned in a Raman mapping. At higher cell concentrations, our platform performs very efficiently in the time frame of seconds for a successful detection. But when the concentration reduces down below 50 cells/mL, nearly 10000 spots need to be mapped to locate one spot with cell SERS and it takes hours for a successful detection. Current micro/nano fluidic devices enable successful isolation of CTCs with concentration as low as 5 cells per mL blood. We would expect to realize the full potential of our platform when integrated with microfluidic devices as downstream analysis platform to extract detailed cellular information.

7.2.4 PCA and Peak Correlation of the Cell SERS

Principal component analysis (PCA), a powerful multivariate analytical tool, was employed to demonstrate spectroscopic variations and peak correlations. PCA is a statistical method for finding the components in a multivariate data set that has the largest variance. It serves to reduce the dimension of the data to a few key components by orthogonal transformation, which best explain the variance across data entries. Hence, PCA is capable of identifying characteristics that relates to classification and discrimination of two groups of data. **Figure 7.6** illustrates the PCA analysis (PC1 vs

PC2) of cell SERS and the plot can be subdivided into two areas with the cancer cells (red dots) find their location at the lower right corner. Having processed thousands of cell SERS data, we achieved the sensitivity of 95% and specificity of 91% for our platform, which is among the best performance of SERS structures for cancer diagnosis.

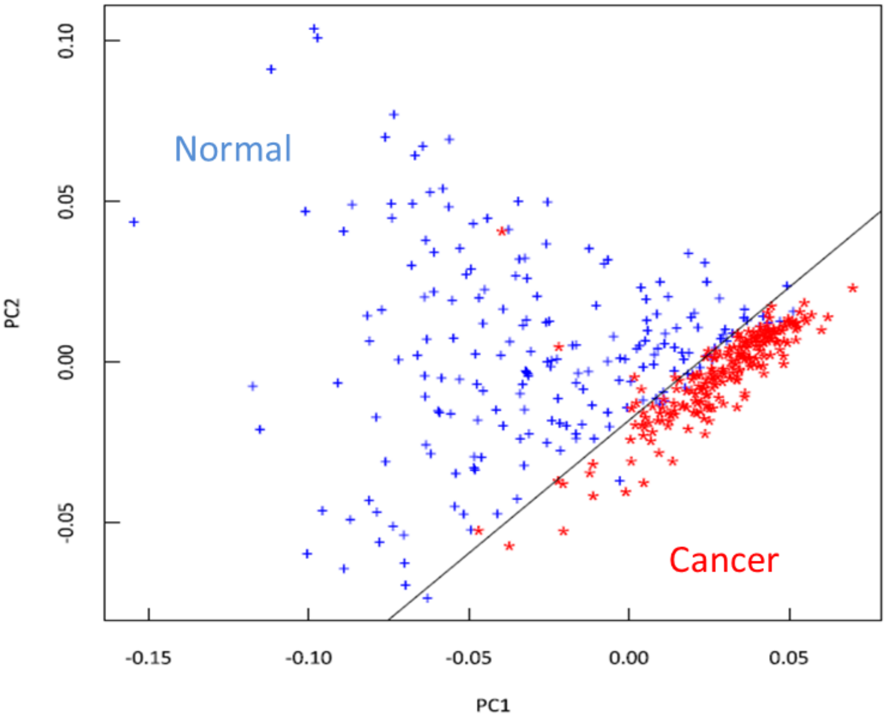

Figure 7.6: PCA of normal and cancer cell SERS spectra.

Apart from achieving automated classification of cancer and normal samples with PCA and pocket algorithm, we performed peak intensity correlation analysis to gain more insight into the biochemical difference in cell content that was revealed in the SERS spectra. We took the area under each major peak in each spectrum to be the intensity of the peak. The intensities from two different peaks were plotted against each other, and all such scatterplots were collected in a scatterplot matrix. If two peaks in the SERS spectra are either from the same or closely related biochemical constituent, the scatterplot of intensities of one peak against another peak would approximately lie on a straight line. Otherwise, the scatterplot would be random. Calculation of correlation between peak intensities gave a quantitative measure of the possible common sources of SERS peaks.

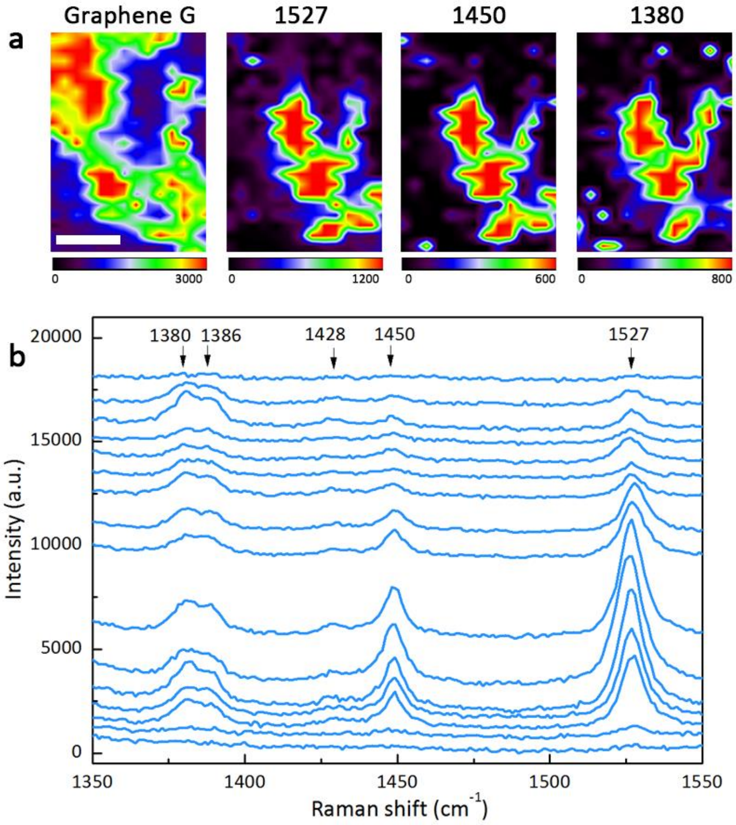

Figure 7.7: (a) SERS intensity mappings of graphene G band, cancer cell 1527 cm^{-1} peak, 1450 cm^{-1} peak and 1380 cm^{-1} peak. (b) A set of SERS spectra along the line across the cancer cell.

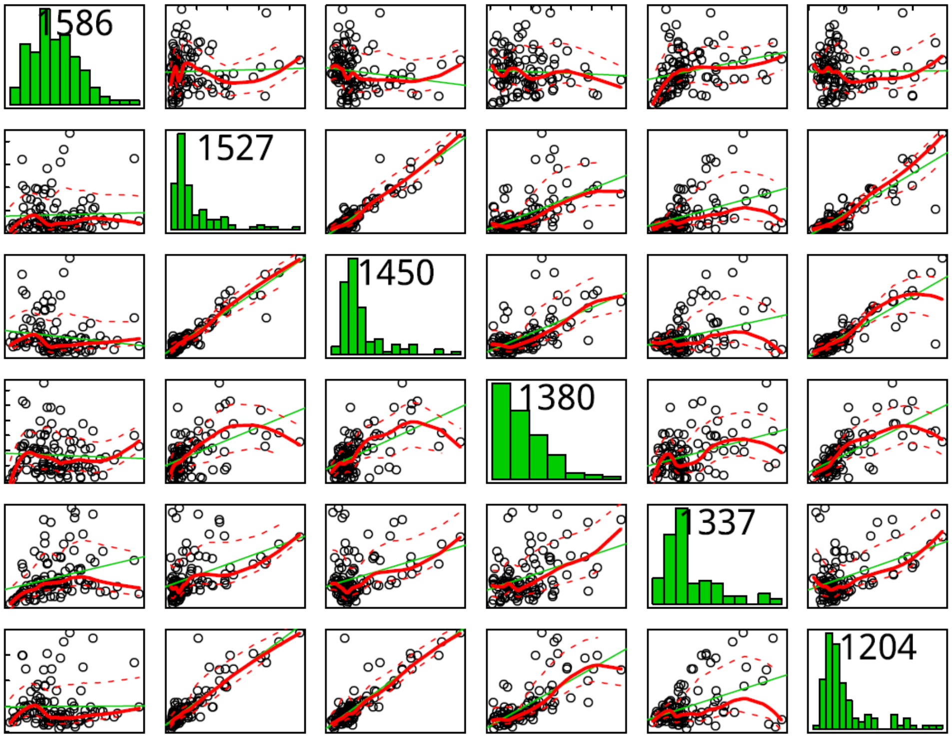

Figure 7.8: Peak correlation analysis of cancer cell SERS peaks.

Figure 7.7a show the SERS intensity of mappings of graphene G band, cancer cell 1527 cm^{-1} peak, 1450 cm^{-1} peak and 1380 cm^{-1} peak from a cancer cell. The distribution of 1527 cm^{-1} peak intensity is almost identical to the 1450 cm^{-1} peak intensity, while the 1380 cm^{-1} peak intensity distribution is slightly different. **Figure 7.7b** shows a series of SERS spectra took along the line scanning across the cancer cell. It could be noted that the intensity of 1527 cm^{-1} peak is proportional to the 1450 cm^{-1} peak intensity, but the pair of 1380 and 1386 cm^{-1} peaks are less likely to be correlated with the 1527 cm^{-1} and 1450 cm^{-1} peaks. The peak correlation analysis in **Figure 7.8** presents the statistical correlation between two peaks. The peaks that are linearly correlated are more likely to originate from the same intracellular component. The 1586 cm^{-1} graphene G peak is not correlated to any cancer SERS peaks. The 1527 cm^{-1}, 1450 cm^{-1} and 1204 cm^{-1} peaks, all assigned to C-H bond related vibrations, are highly correlated. The peak correlation analysis opens up new opportunities to determine the assignments of Raman peaks.

7.3 Monitoring Structural Change of Amyloid β Protein

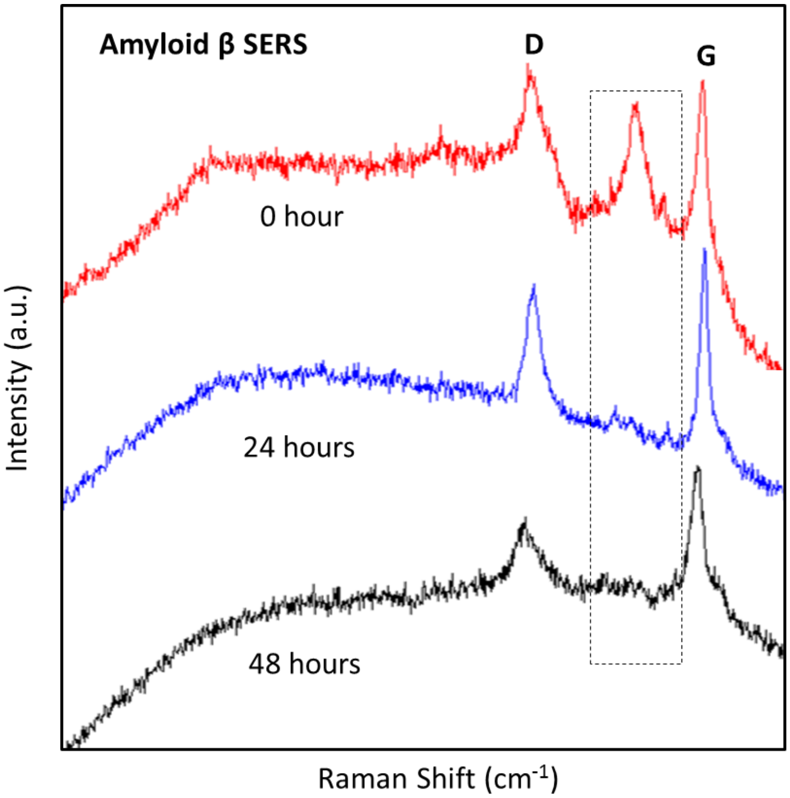

Figure 7.9: Time dependent SERS of Amyloid β (1-40) protein.

Amyloid β protein fragment 1-40 (Aβ(1-40)) was diluted in phosphate buffer saline (PBS) solution to 1 μM. The SERS measurements were carried out after sampling from Aβ protein solutions incubated in vitro. Aβ aggregation formed in free solution at room temperature and samples were taken periodically (every hour in first 5 hrs, 24hr, 48hr) for SERS. The measurements were carried out immediately after a minuscule droplet of Aβ solution was deposited to the hybrid platform. The mapping took 10 minutes with single acquisition time of 1 second. Considering the operation and analysis time much shorter than the aggregation process, no further significant aggregation on the platform is expected.

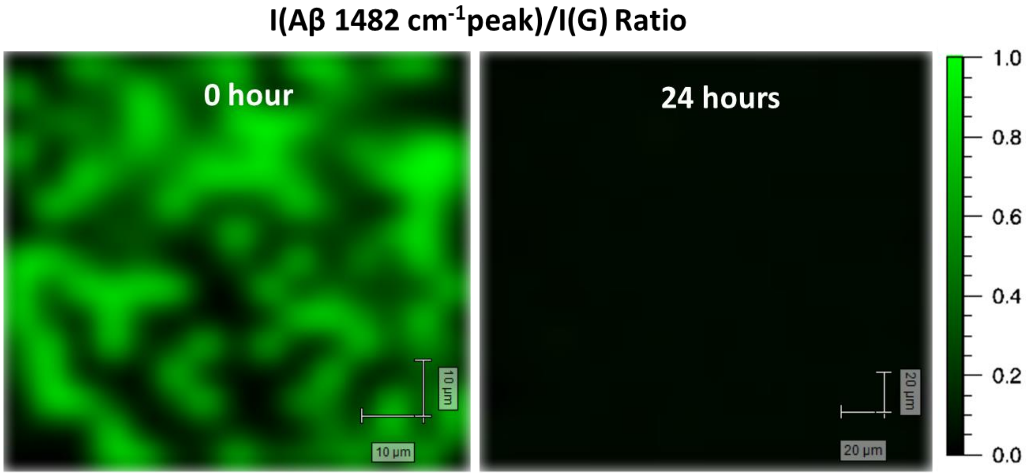

Figure 7.10: Time dependent SERS mapping of I(Aβ 1482 cm^{-1}peak)/I(G) Ratio for Amyloid β (1-40) protein.

The Aβ aggregation is investigated as a function of incubation time using our platform (**Figure 7.9**). At 1 μM, prominent Aβ peaks are identified at around 1480 cm^{-1} pertaining to amino acids. Decomposition of the Aβ peaks indicates the existence of at least four major components: 1482 cm^{-1} peak and 1492 cm^{-1} peak assigned to histidine; 1445 cm^{-1} peak assigned to CH$_2$ bending mode and 1528 cm^{-1} peak assigned to Amide II.

Raman spectra are highly sensitive to the extent of protein configurational change and its resulting conformation. As shown in **Figure 7.10**, the intensity of Aβ 1482 cm^{-1} and 1492 cm^{-1} peak assigned to histidine decreases dramatically in the first 24 hrs. Though the multiple conformations during Aβ aggregation are not clearly demonstrated, the variations of the histidine peaks possibly results from the Aβ conformational change from initially monomers to oligomers.

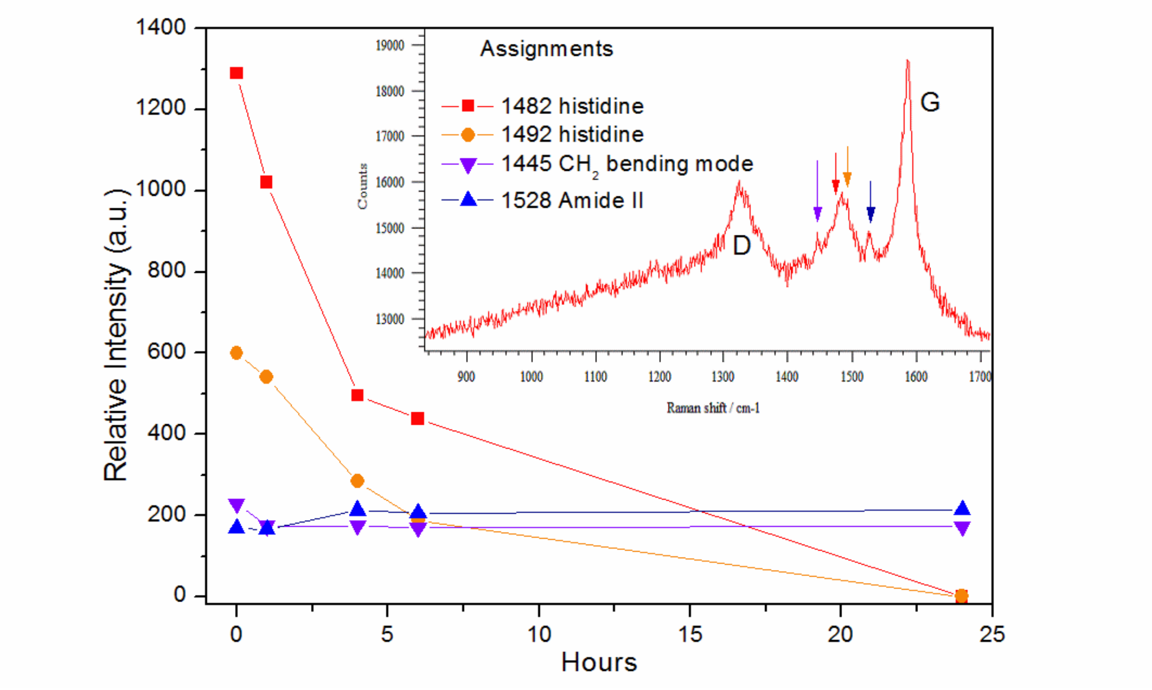

Figure 7.11: Time dependent SERS intensity change of four Amyloid β characteristic peaks.

We obtain an evolution profile of the Aβ SERS peaks (**Figure 11**) in an attempt to attribute the SERS spectral change to different Aβ aggregation stages. In early aggregation stage (first 0-5 hrs) intensity of 1482 cm^{-1} peak and 1492 cm^{-1} peak assigned to histidine drops significantly, however, intensity of 1445 cm^{-1} peak assigned to CH_2 bending mode and 1528 cm^{-1} peak assigned to Amide II remains unchanged. Though the Aβ(1-40) oligomer structure is still unsolved, our results indicate histidine in Aβ may play a role in the formation of oligomers.

7.4 Conclusion

In this Chapter we used the hybrid platform as a non-destructive and label-free tool to detect and profile colon cancer cell in blood plasma. The hybrid platform not only boosts SERS directly from the cell but also enables the assignment of molecular differences between normal and cancer cells. Principal component analysis (PCA) was used to classify the cell SERS spectra and it demonstrated the sensitivity of 95% and specificity of 91% for the hybrid platform in cancer diagnosis. Moreover, the application of peak correlation analysis offers opportunities to determine the SERS peak assignments in a more accurate way. On a separate issue, the observation of time dependent change of Aβ(1-40) protein SERS characteristic peaks presents the great potentials of applying SERS to study the progress aggregation of Aβ protein monomers into oligomers.

The hybrid platform allowed detection limit of 50 cells/mL using a small sample size of 100 µL. For further study, the integration of our platform with filter-based microfluidic devices will realize downstream analysis of isolated CTCs to facilitate early-stage cancer diagnosis. Furthermore, the ease of integration into a probe and the capability of spatially-resolved SERS mapping indicate the huge potential of the graphene hybrid platform in early-stage cancer diagnosis. An SERS probe based on the hybrid platform will be useful for applications of in vivo diagnosis of cancerous tissues. Although future work is needed to unveil the nature of interaction between graphene and cell from chemical and biological perspectives, the extension of our hybrid platform to traditional SERS active systems has potentials for clinical translation of SERS in cancer diagnosis.

8

Summary and Future Study

8.1 Summary

This thesis discusses a novel graphene-Au nano-pyramid hybrid platform and its applications in diverse studies of SERS. The structure with tips of sub-nanometer radius of curvature is fabricated using top-down approach and is amenable to mass production. The structure's potential in bio-sensing is significantly improved by superimposing a monolayer of graphene on Au tips. The hybrid platform not only overcomes the limitations of conventional nanoparticle SERS systems, but also realizes new features to facilitate the research field of SERS.

In the thesis, we have investigated the benefits of introducing graphene to the SERS platform; demonstrated the ultra-high sensitivity evidenced by single molecule detection; presented statistically reliable quantification method for hotspots and analyte concentration; and exploited the applications of platform in biomedical diagnosis of neurotransmitters, protein and cancer cell. The following is a summary of the resulting work presented herein:

(1) In Chapter 2, Chapter 3 and Chapter 4, the graphene-plasmonic platform has been proven to be an ideal platform for SERS in terms of reproducibility, chemically inertness, biological compatibility and easiness of fabrication at the scale of manufacturing. Both FDTD simulation and experimental results suggested that the bio-compatiable graphene hybrid system boosts a high density of hot spots with local SERS enhancement factor of over 10^{10}. The precise location of the SERS hot spots relative to the location and the orientation of the nano-pyramids are studied both experimentally and theoretically. Strong field enhancement appears in between two individual tips and is expected to be the dominant contributor to the detected Raman signal. The hot spot profile of the structure can be achieved by spatially resolved Raman mapping of graphene G or 2D band intensity as a flection of local field enhancement.

(2) In Chapter 5, single molecule sensitivity has been demonstrated for label-free sub-nanomolar sensing of R6G, lysozyme, and neurotransmitters. Detection efficiency has been significantly enhanced since the hot spots can be located for the hybrid platform. It saves up the time spent on randomly searching for a hot spot using the conventional metal nanoparticles. The possibility of placing graphene over nanostructured metal surfaces could also serve as a way to tailor the bio-chemical properties of a plasmonic surface from the conventional metallic ones to the bio-compatible carbon (graphitic)

surfaces. The addition of graphene allows us to determine separately chemical enhancement (CM) and electromagnetic enhancement (EM) in a semi-quantitative fashion. We have reported experimental observation of molecular spectral selectivity as a signal of molecule-graphene interaction (ref. 8). These properties make it possible to modulate SERS effects to extract more spectral information.

(3) In Chapter 6, a versatile quantification method was demonstrated With the platform we obtained statistically reliable SERS quantification using spatially resolved SERS mappings. The stable and reproducible approach established broad quantification dynamic range with extremely low quantification lower limit in principle. . Graphene plays a crucial role in quantifying SERS hotspots and paves the path for investigation of different SERS quantitative parameters. Reproducible and reliable SERS quantification using the hybrid platform not only leverages the ultra-sensitivity but also minimizes the spot-to-spot variations. The platform, combined with techniques of analyte pre-concentration and multi-variate data analysis, can make SERS a powerful and reliable tool for biological and chemical analysis.

(4) In Chapter 7, the SERS applications of hybrid platform was explored beyond sensitivity. The SERS yields of cells and detection sensitivities were much higher than the state-of-art platforms. We were able to distinguish and identify colon cancer cells from normal colon cells in SBF solution with concentration as low as 50 cells/mL. PCA we obtained sensitivity of 95% and specificity of 91% for the hybrid platform. Moreover,

the application of peak correlation analysis offers opportunities to determine the SERS peak assignments in a more accurate way.

8.2 Direction of Future Study

The potential future improvements on the graphene based hybrid platform could focus on two aspects: (1) Assemble the hybrid platform in micro-fluidic and nano-fluidic devices to increase detection efficiency; (2) Integration of the hybrid platform to the optical fiber probe for *in vivo* SERS detection.

8.2.1 Integration of the Platform with Microfluidics

Though detection efficiency has been increased using the hybrid platform by pre-locating hotspots, the rarity of coincidence of hotspots with analyte molecules, especially at low concentrations, makes a successful detection rather time-consuming. Sensitive SERS detection of analyte in solution remains challenging due to the distance dependence of the localized surface plasmon resonance. The analyte of interest must be located in the vicinity of the SERS enhancing surface to gain any signal, and the signal intensity decays rapidly when analyte diffuses away from the surface.

To address this issue, a combined use of SERS and micro-fluidic devices enables sample manipulation and separation to increase the efficiency and reduce the time frame of SERS detection. Microfluidic and nano-fluidic based devices [344,345] have been increasingly applied for biological and chemical analysis. Micrometer scale dimensions result in numerous advantages concerning multiplex detection, small sample volumes, and high throughput detection in aqueous condition. There is also a need for the integration of sensitive detection techniques into these microfluidic devices. The lab-on-a-chip system allows for the integration of processes including sample preparation, separation as well as the implementation of sensitive detection methods.

8.2.2 Optical Fiber Probe for in vivo SERS

The development of a portable SERS instrument using single-channel detection could make *in vivo* SERS of biological samples available. Optical fiber serves as an attractive platform for SERS sensing since it overcomes problems related to free-space beams and optical alignment [346]. Besides, optical fiber is easily obtainable and relatively cheap. There have been many previous attempts [347] on integrating SERS surfaces onto the distal tips of optical fibers. In such way both the excitation laser beam and the scattered light are guided within the same fiber. The works generally rely on metal-island or silver nanoparticle deposition to produce nanoscale roughness for SERS detection. Introducing the graphene based hybrid platform will overcome the fundamental problems of poor reproducibility, chemical stability and bio-compatibility that limit the performance of fiber SERS.

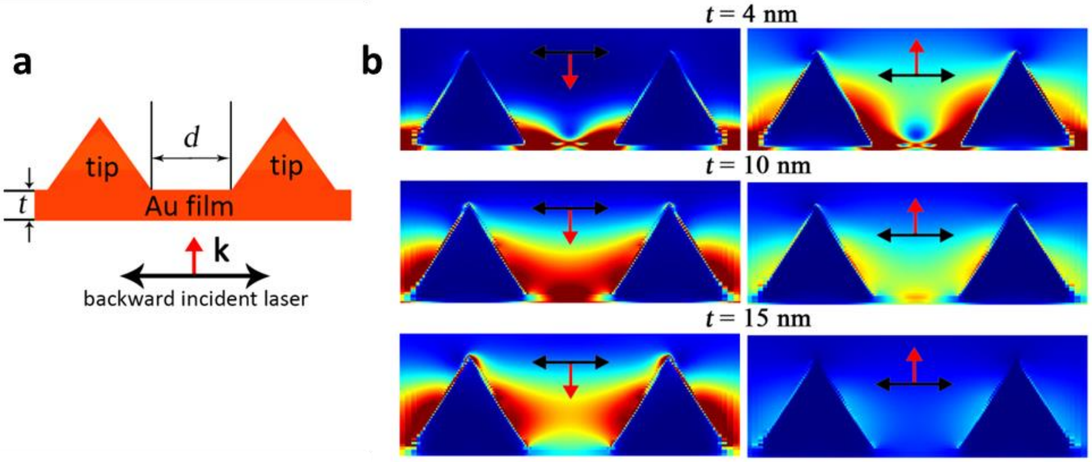

Figure 8.1: (a), Illustration of the FDTD model setup for backward incident laser to simulate fiber SERS. **(b),** E-field intensity distribution with both forward and backward incident light at various underneath Au film thickness.

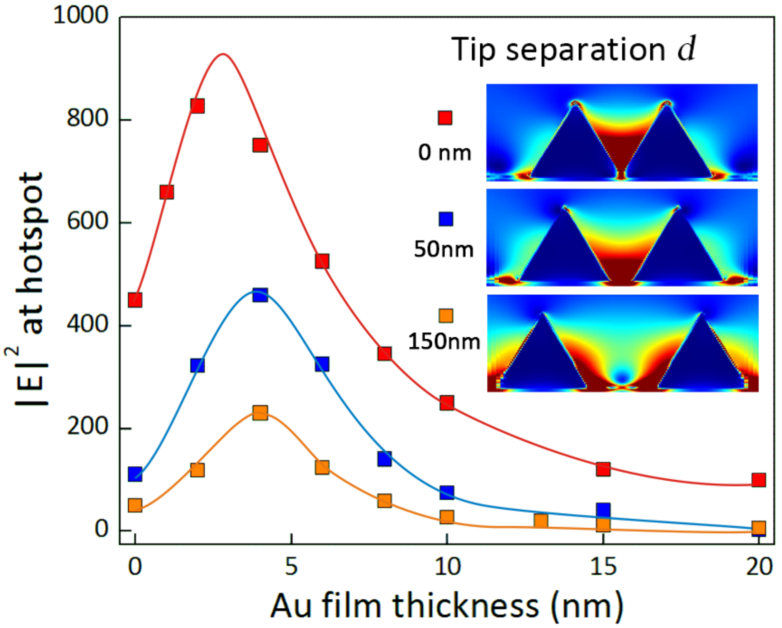

Figure 8.2: The hotspot enhancement as a function of underneath Au film thickness. **Inset:** E-field intensity distribution with backward incident light at tip separation d=0, 50, 150 nm (underneath Au film thickness t= 4nm).

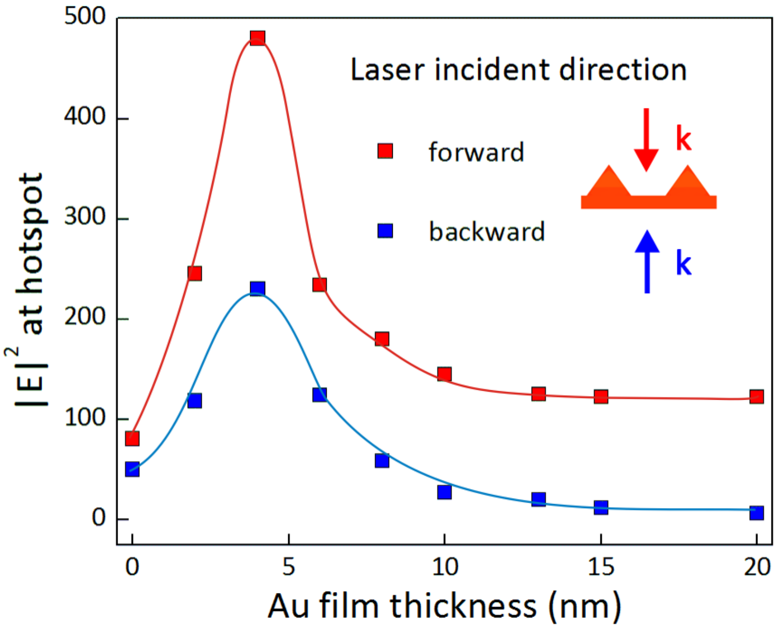

Figure 8.3: The hotspot enhancement as a function of underneath Au film thickness at tip separation d=150 nm with both forward and backward incident light.

To explore the potentially very important allocations including *in vivo* spatial and time-resolve sensing, we studied the delicate dependence of the plasmon resonance behavior on various structural factors. Due to the fabrication method, there is an additional Au thin film with tunable thickness under the Au tip structure. In the case of fiber-based SERS device, the laser beam incidents from the backward direction to the nanostructures covering the fiber probe end (**Figure 8.1a**). The FDTD results indicate that adding a very thin Au layer closely underneath Au tips would modify the electromagnetic field distribution (**Figure 8.1b).** When the underneath Au film is too thick with thickness larger than 15nm, about 100% of the backward incident laser energy will be absorbed by the film, thus the plasmon resonant intensity of Au tips is dramatically reduced. However, when the film thickness is lower than 10nm, very strong EM field enhancement can be achieved between tips with hot spot intensity and effective volume comparable to the forward incident case. In **Figure 8.2** and **Figure 8.3**, the Au film thickness dependence of hot spot enhancement factor is further explored. First, for both forward and backward incident laser directions, when the underneath Au thin film thickness is of ~4nm, the hot spots between Au tips have the largest |E| enhancement. The separation between tips also plays an important role in the |E| enhancement at hot spots. With the tip separation decreasing to 0nm, the hot spot |E| enhancement reaches the maximum.

The theoretical results via FDTD indicates that adding a very thin Au layer closely underneath Au tips would modify the electromagnetic field distribution, and the EM field at hot spots could be even higher if the Au film is of certain thickness. Such extra enhancement induced by adding a Au film exists for both forward and backward incident laser, providing guidance on designing fiber-based SERS probe.

Bibliography

[1]. Fleischmann, M., Hendra, P. J. & McQuillan, A. J. Raman spectra of pyridine adsorbed at a silver electrode. *Chem. Phys. Lett.* **26,** 163–166 (1974).

[2]. Alvarez-Puebla, R. A. & Liz-Marzán, L. M. SERS-based diagnosis and biodetection. *Small* **6,** 604–610 (2010).

[3]. Sharma, B., Frontiera, R. R., Henry, A.-I., Ringe, E. & Van Duyne, R. P. SERS: Materials, applications, and the future. *Mater. Today* **15,** 16–25 (2012).

[4]. Kneipp, J., Kneipp, H. & Kneipp, K. SERS--a single-molecule and nanoscale tool for bioanalytics. *Chem. Soc. Rev.* **37,** 1052–60 (2008).

[5]. Luo, S.-C., Sivashanmugan, K., Liao, J.-D., Yao, C.-K. & Peng, H.-C. Nanofabricated SERS-active substrates for single-molecule to virus detection in vitro: a review. *Biosens. Bioelectron.* **61,** 232–40 (2014).

[6]. Qian, X.-M. & Nie, S. M. Single-molecule and single-nanoparticle SERS: from fundamental mechanisms to biomedical applications. *Chem. Soc. Rev.* **37,** 912–20 (2008).

[7]. Hering, K. *et al.* SERS: a versatile tool in chemical and biochemical diagnostics. *Anal. Bioanal. Chem.* **390,** 113–124 (2007).

[8]. Kahl, M., Voges, E., Kostrewa, S., Viets, C. & Hill, W. Periodically structured metallic substrates for SERS. *Sensors and Actuators B: Chemical* **51,** 285–291 (1998).

[9]. Tong, L., Zhu, T. & Liu, Z. Approaching the electromagnetic mechanism of surface-enhanced Raman scattering: from self-assembled arrays to individual gold nanoparticles. *Chem. Soc. Rev.* **40,** 1296–1304 (2011).

[10]. Betz, J. F., Yu, W. W., Cheng, Y., White, I. M. & Rubloff, G. W. Simple SERS substrates: powerful, portable, and full of potential. *Phys. Chem. Chem. Phys.* **16,** 2224–39 (2014).

[11]. Freeman, R. G. *et al.* Self-Assembled Metal Colloid Monolayers: An Approach to SERS Substrates. *Science* **267,** 1629–1632 (1995).

[12]. Jackson, J. B. & Halas, N. J. Surface-enhanced Raman scattering on tunable plasmonic nanoparticle substrates. *Proc. Natl. Acad. Sci. U. S. A.* **101,** 17930–17935 (2004).

[13]. Ko, H., Singamaneni, S. & Tsukruk, V. V. Nanostructured surfaces and assemblies as SERS media. *Small* **4,** 1576–1599 (2008).

[14]. Yoon, I. *et al.* Single nanowire on a film as an efficient SERS-active platform. *J. Am. Chem. Soc.* **131,** 758–762 (2009).

[15]. Ansar, S. M., Li, X., Zou, S. & Zhang, D. Quantitative comparison of Raman activities, SERS activities, and SERS enhancement factors of organothiols: Implication to chemical enhancement. *J. Phys. Chem. Lett.* **3,** 560–565 (2012).

[16]. Le Ru, E. C., Blackie, E. J., Meyer, M. & Etchegoin, P. G. Surface Enhanced Raman Scattering Enhancement Factors: A Comprehensive Study. *J. Phys. Chem. C* **111,** 13794–13803 (2007).

[17]. Novoselov, K. S. *et al.* Electric field effect in atomically thin carbon films. *Science* **306,** 666–669 (2004).

[18]. Novoselov, K. S. *et al.* Two-dimensional atomic crystals. *Proc. Natl. Acad. Sci. U. S. A.* **102,** 10451–10453 (2005).

[19]. Novoselov, K. S. *et al.* Two-dimensional gas of massless Dirac fermions in graphene. *Nature* **438,** 197–200 (2005).

[20]. Novoselov, K. S. *et al.* Room-Temperature Quantum Hall. *Science (80-.).* **315,** 2007 (2007).

[21]. Raman, C. V. A Change of Wave-length in Light Scattering. *Nature* **121,** 619–619 (1928).

[22]. Moskovits, M. Surface-enhanced spectroscopy. *Rev. Mod. Phys.* **57,** 783–826 (1985).

[23]. Cialla, D. *et al.* Surface-enhanced Raman spectroscopy (SERS): Progress and trends. *Analytical and Bioanalytical Chemistry* **403,** 27–54 (2012).

[24]. Nie, S. Probing Single Molecules and Single Nanoparticles by Surface-Enhanced Raman Scattering. *Science (80-.).* **275,** 1102–1106 (1997).

[25]. Kneipp, K. *et al.* Single Molecule Detection Using Surface-Enhanced Raman Scattering (SERS). *Phys. Rev. Lett.* **78,** 1667–1670 (1997).

[26]. Wildenberg, S. M. J. L. Van Den, Prevo, B., Peterman, E. J. G. & Ferrand, P. Single Molecule Analysis. *Methods Cell Biol.* **783,** 81–99 (2011).

[27]. Weiss, S. Fluorescence Spectroscopy of Single Biomolecules. *Science* **283,** 1676–1683 (1999).

[28]. Brown, R. J. C. & Milton, M. J. T. Nanostructures and nanostructured substrates for surface-enhanced Raman scattering (SERS). *Journal of Raman Spectroscopy* **39,** 1313–1326 (2008).

[29]. Cho, W. J., Kim, Y. & Kim, J. K. Ultrahigh-density array of silver nanoclusters for SERS substrate with high sensitivity and excellent reproducibility. *ACS Nano* **6,** 249–255 (2012).

[30]. Tripp, R. A., Dluhy, R. A. & Zhao, Y. Novel nanostructures for SERS biosensing. *Nano Today* **3,** 31–37 (2008).

[31]. Zhang, J., Gao, Y., Alvarez-Puebla, R. A., Buriak, J. M. & Fenniri, H. Synthesis and SERS properties of nanocrystalline gold octahedra generated from thermal decomposition of HAuCl4 in block copolymers. *Adv. Mater.* **18,** 3233–3237 (2006).

[32]. Garcı, F. J. Collective Theory for Surface Enhanced Raman Scattering. 1163–1166 (1996).

[33]. Kumar, G. V. P. Plasmonic nano-architectures for surface enhanced Raman scattering: a review. *J. Nanophotonics* **6,** 064503 (2012).

[34]. Dasary, S. S. R., Singh, A. K., Senapati, D., Yu, H. & Ray, P. C. Gold nanoparticle based label-free SERS probe for ultrasensitive and selective detection of trinitrotoluene. *J. Am. Chem. Soc.* **131,** 13806–13812 (2009).

[35]. Cheng, H.-W., Huan, S.-Y., Wu, H.-L., Shen, G.-L. & Yu, R.-Q. Surface-enhanced Raman spectroscopic detection of a bacteria biomarker using gold nanoparticle immobilized substrates. *Anal. Chem.* **81,** 9902–9912 (2009).

[36]. Wells, S. M., Retterer, S. D., Oran, J. M. & Sepaniak, M. J. Controllable nanofabrication of aggregate-like nanoparticle substrates and evaluation for surface-enhanced Raman spectroscopy. *ACS Nano* **3,** 3845–3853 (2009).

[37]. Shanmukh, S. *et al.* Rapid and sensitive detection of respiratory virus molecular signatures using a silver nanorod array SERS substrate. *Nano Lett.* **6,** 2630–2636 (2006).

[38]. Gopinath, A. *et al.* Plasmonic nanogalaxies: Multiscale aperiodic arrays for surface-enhanced Raman sensing. *Nano Lett.* **9,** 3922–3929 (2009).

[39]. Hu, M. *et al.* Gold nanofingers for molecule trapping and detection. *J. Am. Chem. Soc.* **132,** 12820–12822 (2010).

[40]. Grzelczak, M., Pérez-Juste, J., Mulvaney, P. & Liz-Marzán, L. M. Shape control in gold nanoparticle synthesis. *Chem. Soc. Rev.* **37,** 1783–1791 (2008).

[41]. Tong, L., Xu, H. & Käll, M. Nanogaps for SERS applications. *MRS Bull.* **39,** 163–168 (2014).

[42]. Banholzer, M. J., Millstone, J. E., Qin, L. & Mirkin, C. A. Rationally designed nanostructures for surface-enhanced Raman spectroscopy. *Chem. Soc. Rev.* **37,** 885–897 (2008).

[43]. Zito, G., Rusciano, G., Pesce, G., Dochshanov, A. & Sasso, A. Surface-enhanced Raman imaging of cell membrane by a highly homogeneous and isotropic silver nanostructure. *Nanoscale* **7,** 8593–8606 (2015).

[44]. Zhang, L., Lang, X., Hirata, A. & Chen, M. Wrinkled nanoporous gold films with ultrahigh surface-enhanced raman scattering enhancement. *ACS Nano* **5,** 4407–4413 (2011).

[45]. Xu, J., Zhang, L., Gong, H., Homola, J. & Yu, Q. Tailoring plasmonic nanostructures for optimal SERS sensing of small molecules and large microorganisms. *Small* **7,** 371–376 (2011).

[46]. Chen, A. *et al.* Self-assembled large Au nanoparticle arrays with regular hot spots for SERS. *Small* **7,** 2365–2371 (2011).

[47]. Abu Hatab, N. A., Oran, J. M. & Sepaniak, M. J. Surface-enhanced Raman spectroscopy substrates created via electron beam lithography and nanotransfer printing. *ACS Nano* **2,** 377–385 (2008).

[48]. Alvarez-Puebla, R., Cui, B., Bravo-Vasquez, J. P., Veres, T. & Fenniri, H. Nanoimprinted SERS-active substrates with tunable surface plasmon resonances. *J. Phys. Chem. C* **111,** 6720–6723 (2007).

[49]. Halvorson, R. a. & Vikesland, P. J. Surface-Enhanced Raman Spectroscopy (SERS) for Environmental Analyses. *Environ. Sci. Technol.* **44,** 7749–7755 (2010).

[50]. Li, M. *et al.* Three-dimensional hierarchical plasmonic nano-architecture enhanced surface-enhanced Raman scattering immunosensor for cancer biomarker detection in blood plasma. *ACS Nano* **7,** 4967–4976 (2013).

[51]. Liu, G. L. & Lee, L. P. Nanowell surface enhanced Raman scattering arrays fabricated by soft-lithography for label-free biomolecular detections in integrated microfluidics. *Appl. Phys. Lett.* **87,** (2005).

[52]. Bantz, K. C. *et al.* Recent progress in SERS biosensing. *Phys. Chem. Chem. Phys.* **13,** 11551–11567 (2011).

[53]. Harper, M. M., McKeating, K. S. & Faulds, K. Recent developments and future directions in SERS for bioanalysis. *Phys. Chem. Chem. Phys.* **15,** 5312–28 (2013).

[54]. Xie, W. & Schlücker, S. Medical applications of surface-enhanced Raman scattering. *Phys. Chem. Chem. Phys.* **15,** 5329 (2013).

[55]. Guarrotxena, N. & Bazan, G. C. Antitags: SERS-encoded nanoparticle assemblies that enable single-spot multiplex protein detection. *Adv. Mater.* **26,** 1941–1946 (2014).

[56]. Han, X. X., Zhao, B. & Ozaki, Y. Surface-enhanced Raman scattering for protein detection. *Analytical and Bioanalytical Chemistry* **394,** 1719–1727 (2009).

[57]. Wang, Y. *et al.* SERS opens a new way in aptasensor for protein recognition with high sensitivity and selectivity. *Chem. Commun. (Camb).* 5220–5222 (2007). doi:10.1039/b709492b

[58]. Shafer-Peltier, K. E., Haynes, C. L., Glucksberg, M. R. & Duyne, R. P. Van. Toward a Glucose Biosensor Based on Surface-Enhanced {R}aman Scattering. *J. Amer. Chem. Soc.* **125,** 588–593 (2003).

[59]. Radziuk, D. & Moehwald, H. Prospects for plasmonic hot spots in single molecule SERS towards the chemical imaging of live cells. *Phys. Chem. Chem. Phys.* (2015). doi:10.1039/C4CP04946B

[60]. Qian, X. *et al.* In vivo tumor targeting and spectroscopic detection with surface-enhanced Raman nanoparticle tags. *Nat. Biotechnol.* **26,** 83–90 (2008).

[61]. Zhang, X., Young, M. a., Lyandres, O. & Van Duyne, R. P. Rapid detection of an anthrax biomarker by surface-enhanced Raman spectroscopy. *J. Am. Chem. Soc.* **127,** 4484–4489 (2005).

[62]. Etchegoin, P. *et al.* Electromagnetic contribution to surface enhanced Raman scattering revisited. *J. Chem. Phys.* **119,** 5281–5289 (2003).

[63]. Brown, R. J. C., Wang, J. & Milton, M. J. T. Electromagnetic modelling of Raman enhancement from nanoscale structures as a means to predict the efficacy of SERS substrates. *J. Nanomater.* **2007,** (2007).

[64]. Maitani, M. M. *et al.* Study of SERS chemical enhancement factors using buffer layer assisted growth of metal nanoparticles on self-assembled monolayers. *J. Am. Chem. Soc.* **131,** 6310–6311 (2009).

[65]. Zayak, A. T. *et al.* Chemical Raman enhancement of organic adsorbates on metal surfaces. *Phys. Rev. Lett.* **106,** (2011).

[66]. Park, W.-H. & Kim, Z. H. Charge transfer enhancement in the SERS of a single molecule. *Nano Lett.* **10,** 4040–4048 (2010).

[67]. Bell, S. E. J. & Sirimuthu, N. M. S. Quantitative surface-enhanced Raman spectroscopy. *Chem. Soc. Rev.* **37,** 1012–24 (2008).

[68]. Kasera, S., Biedermann, F., Baumberg, J. J., Scherman, O. A. & Mahajan, S. Quantitative SERS using the sequestration of small molecules inside precise plasmonic nanoconstructs. *Nano Lett.* **12,** 5924–5928 (2012).

[69]. Shaw, C. P. *et al.* Statistical Correlation Between SERS Intensity and Nanoparticle Cluster Size. *J. Phys. Chem. C* **117,** 16596–16605 (2013).

[70]. Marotta, N. E., Beavers, K. R. & Bottomley, L. a. Limitations of surface enhanced Raman scattering in sensing DNA hybridization demonstrated by label-free DNA oligos as molecular rulers of distance-dependent enhancement. *Anal. Chem.* **85,** 1440–6 (2013).

[71]. Kleinman, S. L., Frontiera, R. R., Henry, A.-I., Dieringer, J. a & Van Duyne, R. P. Creating, characterizing, and controlling chemistry with SERS hot spots. *Phys. Chem. Chem. Phys.* **15,** 21–36 (2013).

[72]. Castro Neto, A. H., Peres, N. M. R., Novoselov, K. S. & Geim, A. K. The electronic properties of graphene. *Reviews of Modern Physics* **81,** 109–162 (2009).

[73]. Novoselov, K. S. *et al.* A roadmap for graphene. *Nature* **490,** 192–200 (2012).

[74]. Mak, K. F. *et al.* Measurement of the optical conductivity of graphene. *Phys. Rev. Lett.* **101,** 196405 (2008).

[75]. Lee, C., Wei, X., Kysar, J. W. & Hone, J. Measurement of the elastic properties and intrinsic strength of monolayer graphene. *Science* **321,** 385–388 (2008).

[76]. Chen, S. *et al.* Thermal conductivity of isotopically modified graphene. *Nature Materials* **11,** 203–207 (2012).

[77]. Balandin, A. A. Thermal properties of graphene and nanostructured carbon materials. *Nat. Mater.* **10,** 569–581 (2011).

[78]. Balandin, A. A. *et al.* Superior thermal conductivity of single-layer graphene. *Nano Lett.* **8,** 902–907 (2008).

[79]. Meyer, J. C. *et al.* The structure of suspended graphene sheets. *Nature* **446,** 60–63 (2007).

[80]. Booth, T. J. *et al.* Macroscopic graphene membranes and their extraordinary stiffness. *Nano Lett.* **8,** 2442–2446 (2008).

[81]. Avouris, P. Graphene: Electronic and photonic properties and devices. *Nano Letters* **10,** 4285–4294 (2010).

[82]. Nguyen, P. & Berry, V. Graphene interfaced with biological cells: Opportunities and challenges. *J. Phys. Chem. Lett.* **3,** 1024–1029 (2012).

[83]. Shen, H., Zhang, L., Liu, M. & Zhang, Z. Biomedical applications of graphene. *Theranostics* **2,** 283–294 (2012).

[84]. Zhu, Y. *et al.* Graphene and graphene oxide: Synthesis, properties, and applications. *Adv. Mater.* **22,** 3906–3924 (2010).

[85]. Huang, X. *et al.* Graphene-based materials: Synthesis, characterization, properties, and applications. *Small* **7,** 1876–1902 (2011).

[86]. Nicolosi, V., Chhowalla, M., Kanatzidis, M. G., Strano, M. S. & Coleman, J. N. Liquid Exfoliation of Layered Materials. *Science (80-.).* **340,** 1226419 (2013).

[87]. Hernandez, Y. *et al.* High-yield production of graphene by liquid-phase exfoliation of graphite. *Nat. Nanotechnol.* **3,** 563–568 (2008).

[88]. Ciesielski, A. & Samorì, P. Graphene via sonication assisted liquid-phase exfoliation. *Chem. Soc. Rev.* **43,** 381–98 (2014).

[89]. Li, X. *et al.* Large-area synthesis of high-quality and uniform graphene films on copper foils. *Science* **324,** 1312–1314 (2009).

[90]. Park, H., Rowehl, J. A., Kim, K. K., Bulovic, V. & Kong, J. Doped graphene electrodes for organic solar cells. *Nanotechnology* **21,** 505204 (2010).

[91]. Prasai, D., Tuberquia, J. C., Harl, R. R., Jennings, G. K. & Bolotin, K. I. Graphene: Corrosion-inhibiting coating. *ACS Nano* **6,** 1102–1108 (2012).

[92]. Emtsev, K. V *et al.* Towards wafer-size graphene layers by atmospheric pressure graphitization of silicon carbide. *Nat. Mater.* **8,** 203–207 (2009).

[93]. Sutter, P. Epitaxial graphene: How silicon leaves the scene. *Nature materials* **8,** 171–172 (2009).

[94]. Bae, S. *et al.* Roll-to-roll production of 30-inch graphene films for transparent electrodes. *Nat. Nanotechnol.* **5,** 574–578 (2010).

[95]. Huang, X., Zeng, Z., Fan, Z., Liu, J. & Zhang, H. Graphene-based electrodes. *Advanced Materials* **24,** 5979–6004 (2012).

[96]. Chen, H., Müller, M. B., Gilmore, K. J., Wallace, G. G. & Li, D. Mechanically strong, electrically conductive, and biocompatible graphene paper. *Adv. Mater.* **20,** 3557–3561 (2008).

[97]. Wang, J. *et al.* Rod-coating: Towards large-area fabrication of uniform reduced graphene oxide films for flexible touch screens. *Adv. Mater.* **24,** 2874–2878 (2012).

[98]. Kim, K., Choi, J.-Y., Kim, T., Cho, S.-H. & Chung, H.-J. A role for graphene in silicon-based semiconductor devices. *Nature* **479,** 338–344 (2011).

[99]. Bao, Q. *et al.* Broadband graphene polarizer. *Nature Photonics* **5,** 411–415 (2011).

[100]. Xia, F., Mueller, T., Lin, Y.-M., Valdes-Garcia, A. & Avouris, P. Ultrafast graphene photodetector. *Nat. Nanotechnol.* **4,** 839–843 (2009).

[101]. Bao, Q. & Loh, K. P. Graphene photonics, plasmonics, and broadband optoelectronic devices. *ACS Nano* **6,** 3677–3694 (2012).

[102]. Fang, Z. *et al.* Graphene-antenna sandwich photodetector. *Nano Lett.* **12,** 3808–3813 (2012).

[103]. Schwierz, F. Graphene transistors. *Nat. Nanotechnol.* **5,** 487–496 (2010).

[104]. Han, T.-H. *et al.* Extremely efficient flexible organic light-emitting diodes with modified graphene anode. *Nature Photonics* **6,** 105–110 (2012).

[105]. Stoller, M. D., Park, S., Yanwu, Z., An, J. & Ruoff, R. S. Graphene-Based ultracapacitors. *Nano Lett.* **8,** 3498–3502 (2008).

[106]. Wang, Y., Li, Z., Wang, J., Li, J. & Lin, Y. Graphene and graphene oxide: Biofunctionalization and applications in biotechnology. *Trends in Biotechnology* **29,** 205–212 (2011).

[107]. Liu, Y., Dong, X. & Chen, P. Biological and chemical sensors based on graphene materials. *Chemical Society Reviews* **41,** 2283 (2012).

[108]. Liu, Z., Robinson, J. T., Sun, X. & Dai, H. PEGylated nanographene oxide for delivery of water-insoluble cancer drugs. *J. Am. Chem. Soc.* **130,** 10876–10877 (2008).

[109]. Hong, H. *et al.* In vivo targeting and imaging of tumor vasculature with radiolabeled, antibody-conjugated nanographene. *ACS Nano* **6,** 2361–2370 (2012).

[110]. Jung, H. S. *et al.* Nanographene oxide-hyaluronic acid conjugate for photothermal ablation therapy of skin cancer. *ACS Nano* **8,** 260–268 (2014).

[111]. Ferrari, a. C. *et al.* Raman spectrum of graphene and graphene layers. *Phys. Rev. Lett.* **97,** 1–4 (2006).

[112]. Ferrari, A. C. *et al.* Raman spectrum of graphene and graphene layers. *Phys. Rev. Lett.* **97,** (2006).

[113]. Ferrari, A. C. & Basko, D. M. Raman spectroscopy as a versatile tool for studying the properties of graphene. *Nat. Nanotechnol.* **8,** 235–46 (2013).

[114]. Ni, Z., Wang, Y., Yu, T. & Shen, Z. Raman spectroscopy and imaging of graphene. *Nano Res.* **1,** 273–291 (2010).

[115]. Casiraghi, C., Pisana, S., Novoselov, K. S., Geim, A. K. & Ferrari, A. C. Raman fingerprint of charged impurities in graphene. *Appl. Phys. Lett.* **91,** (2007).

[116]. Casiraghi, C. *et al.* Raman spectroscopy of graphene edges. *Nano Lett.* **9,** 1433–1441 (2009).

[117]. Das, A. *et al.* Monitoring dopants by Raman scattering in an electrochemically top-gated graphene transistor. *Nat. Nanotechnol.* **3,** 210–215 (2008).

[118]. Luo, S. C., Sivashanmugan, K., Liao, J. Der, Yao, C. K. & Peng, H. C. Nanofabricated SERS-active substrates for single-molecule to virus detection in vitro: A review. *Biosens. Bioelectron.* **61,** 232–240 (2014).

[119]. Sun, K. *et al.* Fabrication and field emission study of atomically sharp high-density tungsten nanotip arrays. *J. Appl. Phys.* **108,** 1–4 (2010).

[120]. Li, X. *et al.* Transfer of large-area graphene films for high-performance transparent conductive electrodes. *Nano Lett.* **9,** 4359–4363 (2009).

[121]. Gao, L. *et al.* Face-to-face transfer of wafer-scale graphene films. *Nature* **505,** 190–4 (2014).

[122]. Kim, H. H., Chung, Y., Lee, E., Lee, S. K. & Cho, K. Water-free transfer method for CVD-grown graphene and its application to flexible air-stable graphene transistors. *Adv. Mater.* **26,** 3213–3217 (2014).

[123]. Liang, X. *et al.* Toward clean and crackless transfer of graphene. *ACS Nano* **5,** 9144–9153 (2011).

[124]. Lin, Y. C. *et al.* Clean transfer of graphene for isolation and suspension. *ACS Nano* **5,** 2362–2368 (2011).

[125]. Lock, E. H. *et al.* High-quality uniform dry transfer of graphene to polymers. *Nano Lett.* **12,** 102–107 (2012).

[126]. Regan, W. *et al.* A direct transfer of layer-area graphene. *Appl. Phys. Lett.* **96,** (2010).

[127]. Reina, A. *et al.* Large area, few-layer graphene films on arbitrary substrates by chemical vapor deposition. *Nano Lett.* **9,** 30–35 (2009).

[128]. Suk, J. W. *et al.* Transfer of CVD-grown monolayer graphene onto arbitrary substrates. *ACS Nano* **5,** 6916–6924 (2011).

[129]. Wang, D. Y. *et al.* Clean-lifting transfer of large-area residual-free graphene films. *Adv. Mater.* **25,** 4521–4526 (2013).

[130]. Chen, S. *et al.* Oxidation resistance of graphene-coated Cu and Cu/Ni alloy. *ACS Nano* **5,** 1321–1327 (2011).

[131]. Singh Raman, R. K. *et al.* Protecting copper from electrochemical degradation by graphene coating. *Carbon N. Y.* **50,** 4040–4045 (2012).

[132]. Rafiee, J. *et al.* Wetting transparency of graphene. *Nature Materials* **11,** 217–222 (2012).

[133]. Wang, S., Zhang, Y., Abidi, N. & Cabrales, L. Wettability and surface free energy of graphene films. *Langmuir* **25,** 11078–11081 (2009).

[134]. Bendali, A. *et al.* Purified Neurons can Survive on Peptide-Free Graphene Layers. *Adv. Healthc. Mater.* **2,** 929–933 (2013).

[135]. Sun, K. *et al.* Fabrication and field emission study of atomically sharp high-density tungsten nanotip arrays. *J. Appl. Phys.* **108,** 1–4 (2010).

[136]. Lee, J. Y. *et al.* A method to fabricate a template with a long range ordered dense array of true nanometer scale pits. *IEEE Trans. Nanotechnol.* **10,** 256–259 (2011).

[137]. Li, X., Cai, W., Colombo, L. & Ruoff, R. S. Evolution of graphene growth on Ni and Cu by carbon isotope labeling. *Nano Lett.* **9,** 4268–4272 (2009).

[138]. Yu, Q. *et al.* Graphene segregated on Ni surfaces and transferred to insulators. *Appl. Phys. Lett.* **93,** (2008).

[139]. Losurdo, M., Giangregorio, M. M., Capezzuto, P. & Bruno, G. Graphene CVD growth on copper and nickel: role of hydrogen in kinetics and structure. *Physical Chemistry Chemical Physics* **13,** 20836 (2011).

[140]. Wofford, J. M., Nie, S., McCarty, K. F., Bartelt, N. C. & Dubon, O. D. Graphene islands on Cu foils: The interplay between shape, orientation, and defects. *Nano Lett.* **10,** 4890–4896 (2010).

[141]. Yan, Z. *et al.* Toward the synthesis of wafer-scale single-crystal graphene on copper foils. *ACS Nano* **6,** 9110–9117 (2012).

[142]. Blake, P. *et al.* Making graphene visible. *Appl. Phys. Lett.* **91,** (2007).

[143]. Barnes, W. L., Dereux, A. & Ebbesen, T. W. Surface plasmon subwavelength optics. *Nature* **424,** 824–830 (2003).

[144]. Maier, S. A. *et al.* Plasmonics - A route to nanoscale optical devices. *Adv. Mater.* **13,** 1501–1505 (2001).

[145]. Mulvaney, P. Surface Plasmon Spectroscopy of Nanosized Metal Particles. *Langmuir* **12,** 788–800 (1996).

[146]. Halas, N. J., Lal, S., Chang, W. S., Link, S. & Nordlander, P. Plasmons in strongly coupled metallic nanostructures. *Chem. Rev.* **111,** 3913–3961 (2011).

[147]. Atwater, H. A. & Polman, A. Plasmonics for improved photovoltaic devices. *Nat. Mater.* **9,** 205–213 (2010).

[148]. Johnston, M. B. Plasmonics: Superfocusing of terahertz waves. *Nature Photonics* **1,** 14–15 (2007).

[149]. Brongersma, M. L. Plasmonics: Engineering optical nanoantennas. *Nature Photonics* **2,** 270–272 (2008).

[150]. Willets, K. A., Van Duyne, R. P. & Duyne, R. P. Van. Localized surface plasmon resonance spectroscopy and sensing. *Annu. Rev. Phys. Chem.* **58,** 267–97 (2007).

[151]. Mittleman, D. M. Frontiers in terahertz sources and plasmonics. *Nat. Photonics* **7,** 666–669 (2013).

[152]. Ozbay, E. Plasmonics: merging photonics and electronics at nanoscale dimensions. *Science* **311,** 189–193 (2006).

[153]. Green, M. A. & Pillai, S. Harnessing plasmonics for solar cells. *Nature Photonics* **6,** 130–132 (2012).

[154]. Anker, J. N. *et al.* Biosensing with plasmonic nanosensors. *Nat. Mater.* **7,** 442–453 (2008).

[155]. Brolo, A. Plasmonics for future biosensors. *Nat. Photonics* **6,** 709–713 (2012).

[156]. Zhao, J., Zhang, X., Yonzon, C. R., Haes, A. J. & Van Duyne, R. P. Localized surface plasmon resonance biosensors. *Nanomedicine (Lond).* **1,** 219–228 (2006).

[157]. Cao, L. & Brongersma, M. L. Active Plasmonics: Ultrafast developments. *Nature Photonics* **3,** 12–13 (2009).

[158]. Liu, M. *et al.* A graphene-based broadband optical modulator. *Nature* **474,** 64–67 (2011).

[159]. Gramotnev, D. K. & Bozhevolnyi, S. I. Plasmonics beyond the diffraction limit. *Nature Photonics* **4,** 83–91 (2010).

[160]. Heber, J. Plasmonics: Surfing the wave. *Nature* **461,** 720–722 (2009).

[161]. Ozbay, E. Plasmonics: merging photonics and electronics at nanoscale dimensions. *Science* **311,** 189–193 (2006).

[162]. Fang, Z. & Zhu, X. Plasmonics in nanostructures. *Adv. Mater.* **25,** 3840–3856 (2013).

[163]. Link, S. & El-Sayed, M. A. Size and Temperature Dependence of the Plasmon Absorption of Colloidal Gold Nanoparticles. *J. Phys. Chem. B* **103,** 4212–4217 (1999).

[164]. Lang, X., Qian, L., Guan, P., Zi, J. & Chen, M. Localized surface plasmon resonance of nanoporous gold. *Appl. Phys. Lett.* **98,** (2011).

[165]. Mock, J. J. *et al.* Distance-dependent plasmon resonant coupling between a gold nanoparticle and gold film. *Nano Lett.* **8,** 2245–2252 (2008).

[166]. Hao, F., Nehl, C. L., Hafner, J. H. & Nordlander, P. Plasmon resonances of a gold nanostar. *Nano Lett.* **7,** 729–732 (2007).

[167]. Sanders, A. W. *et al.* Observation of plasmon propagation, redirection, and fan-out in silver nanowires. *Nano Lett.* **6,** 1822–1826 (2006).

[168]. Gao, C. *et al.* Highly stable silver nanoplates for surface plasmon resonance biosensing. *Angew. Chemie - Int. Ed.* **51,** 5629–5633 (2012).

[169]. Ditlbacher, H. *et al.* Silver nanowires as surface plasmon resonators. *Phys. Rev. Lett.* **95,** (2005).

[170]. Saito, Y., Wang, J. J., Smith, D. A. & Batchelder, D. N. A simple chemical method for the preparation of silver surfaces for efficient SERS. *Langmuir* **18,** 2959–2961 (2002).

[171]. Rice, K. P., Walker, E. J., Stoykovich, M. P. & Saunders, A. E. Solvent-dependent surface plasmon response and oxidation of copper nanocrystals. *J. Phys. Chem. C* **115,** 1793–1799 (2011).

[172]. Previte, M. J. R., Zhang, Y., Aslan, K. & Geddes, C. D. Surface plasmon coupled fluorescence from copper substrates. *Appl. Phys. Lett.* **91,** (2007).

[173]. Robusto, P. F. & Braunstein, R. Optical measurements of the surface plasmon of copper. *Phys. status solidi* **107,** 443–449 (1981).

[174]. Pastoriza-Santos, I., Sánchez-Iglesias, A., Rodríguez-González, B. & Liz-Marzán, L. M. Aerobic synthesis of Cu nanoplates with intense plasmon resonances. *Small* **5,** 440–443 (2009).

[175]. Ekinci, Y., Solak, H. H. & Löffler, J. F. Plasmon resonances of aluminum nanoparticles and nanorods. *J. Appl. Phys.* **104,** (2008).

[176]. Knight, M. W. *et al.* Aluminum for plasmonics. *ACS Nano* **8,** 834–840 (2014).

[177]. Langhammer, C., Schwind, M., Kasemo, B. & Zorić, I. Localized surface plasmon resonances in aluminum nanodisks. *Nano Lett.* **8,** 1461–1471 (2008).

[178]. Hutter, E. & Fendler, J. H. Exploitation of Localized Surface Plasmon Resonance. *Adv. Mater.* **16,** 1685–1706 (2004).

[179]. Luther, J. M., Jain, P. K., Ewers, T. & Alivisatos, A. P. Localized surface plasmon resonances arising from free carriers in doped quantum dots. *Nat. Mater.* **10,** 361–366 (2011).

[180]. Lal, S. *et al.* Tailoring plasmonic substrates for surface enhanced spectroscopies. *Chem. Soc. Rev.* **37,** 898–911 (2008).

[181]. Pinkhasova, P., Yang, L., Zhang, Y., Sukhishvili, S. & Du, H. Differential SERS activity of gold and silver nanostructures enabled by adsorbed poly(vinylpyrrolidone). *Langmuir* **28,** 2529–2535 (2012).

[182]. Funston, A. M., Novo, C., Davis, T. J. & Mulvaney, P. Plasmon coupling of gold nanorods at short distances and in different geometries. *Nano Lett.* **9,** 1651–1658 (2009).

[183]. Wu, S. *et al.* Enhanced optical transmission: Role of the localized surface plasmon. *Appl. Phys. Lett.* **93,** 101113 (2008).

[184]. Eustis, S. & el-Sayed, M. A. Why gold nanoparticles are more precious than pretty gold: noble metal surface plasmon resonance and its enhancement of the radiative and nonradiative properties of nanocrystals of different shapes. *Chem. Soc. Rev.* **35,** 209–217 (2006).

[185]. Koppens, F. H. L., Chang, D. E. & García De Abajo, F. J. Graphene plasmonics: A platform for strong light-matter interactions. *Nano Lett.* **11,** 3370–3377 (2011).

[186]. Zhou, W. *et al.* Atomically localized plasmon enhancement in monolayer graphene. *Nature Nanotechnology* **7,** 161–165 (2012).

[187]. Chen, J. *et al.* Optical nano-imaging of gate-tunable graphene plasmons. *Nature* (2012). doi:10.1038/nature11254

[188]. Tassin, P., Koschny, T., Kafesaki, M. & Soukoulis, C. M. A comparison of graphene, superconductors and metals as conductors for metamaterials and plasmonics. *Nature Photonics* **6,** 259–264 (2012).

[189]. Yang, Z. L. *et al.* FDTD for plasmonics: Applications in enhanced Raman spectroscopy. *Chinese Sci. Bull.* **55,** 2635–2642 (2010).

[190]. Wu, Y. & Nordlander, P. Finite-Difference Time-Domain Modeling of the Optical Properties of Nanoparticles near Dielectric Substrates. *J. Phys. Chem. C* **114,** 7302–7307 (2010).

[191]. Buil, S. *et al.* FDTD simulations of localization and enhancements on fractal plasmonics nanostructures. *Opt. Express* **20,** 11968 (2012).

[192]. Berenger, J.-P. A perfectly matched layer for the absorption of electromagnetic waves. *J. Comput. Phys.* **114,** 185–200 (1994).

[193]. Berenger, J.-P. Three-Dimensional Perfectly Matched Layer for the Absorption of Electromagnetic Waves. *J. Comput. Phys.* **127,** 363–379 (1996).

[194]. Taflove, A. Review of the formulation and applications of the finite-difference time-domain method for numerical modeling of electromagnetic wave interactions with arbitrary structures. *Wave Motion* **10,** 547–582 (1988).

[195]. Liu, J. *et al.* Generalization of the FDTD algorithm for simulations of hydrodynamic nonlinear Drude model. *J. Comput. Phys.* **229,** 5921–5932 (2010).

[196]. Oubre, C. & Nordlander, P. Finite-difference time-domain studies of the optical properties of nanoshell dimers. *J. Phys. Chem. B* **109,** 10042–10051 (2005).

[197]. Hao, F. & Nordlander, P. Efficient dielectric function for FDTD simulation of the optical properties of silver and gold nanoparticles. *Chem. Phys. Lett.* **446,** 115–118 (2007).

[198]. Heavens, O. S. Handbook of Optical Constants of Solids II. *Journal of Modern Optics* **39,** 189–189 (1992).

[199]. Graf, D. *et al.* Spatially resolved raman spectroscopy of single- and few-layer graphene. *Nano Lett.* **7,** 238–242 (2007).

[200]. Schedin, F. *et al.* Surface-enhanced Raman spectroscopy of graphene. *ACS Nano* **4,** 5617–5626 (2010).

[201]. Yao, Y. *et al.* High-responsivity mid-infrared graphene detectors with antenna-enhanced photocarrier generation and collection. *Nano Lett.* **14,** 3749–3754 (2014).

[202]. Fang, Z. *et al.* Graphene-antenna sandwich photodetector. *Nano Lett.* **12,** 3808–3813 (2012).

[203]. Echtermeyer, T. J. *et al.* Strong plasmonic enhancement of photovoltage in graphene. *Nat. Commun.* **2,** 458 (2011).

[204]. Sood, A. K., Gupta, R. & Asher, S. A. Origin of the unusual dependence of Raman D band on excitation wavelength in graphite-like materials. *J. Appl. Phys.* **90,** 4494–4497 (2001).

[205]. Cançado, L. G. *et al.* Quantifying defects in graphene via Raman spectroscopy at different excitation energies. *Nano Lett.* **11,** 3190–3196 (2011).

[206]. Willets, K. a. Super-resolution imaging of SERS hot spots. *Chem. Soc. Rev.* **43,** 3854–64 (2014).

[207]. Zhao, L. *et al.* The extinction spectra of silver nanoparticle arrays: Influence of array structure on plasmon resonance wavelength and width. *J. Phys. Chem. B* **107,** 7343–7350 (2003).

[208]. Gilbertson, A. M. *et al.* Plasmon-induced optical anisotropy in hybrid graphene-metal nanoparticle systems. *Nano Lett.* 150427105435003 (2015). doi:10.1021/acs.nanolett.5b00789

[209]. Fang, Z. *et al.* Plasmon-induced doping of graphene. *ACS Nano* **6,** 10222–10228 (2012).

[210]. Muszynski, R., Seger, B. & Kamat, P. V. Decorating graphene sheets with gold nanoparticles. *J. Phys. Chem. C* **112,** 5263–5266 (2008).

[211]. Sundaram, R. S. *et al.* The graphene-gold interface and its implications for nanoelectronics. *Nano Lett.* **11,** 3833–3837 (2011).

[212]. Zhu, X. *et al.* Enhanced light-matter interactions in graphene-covered gold nanovoid arrays. *Nano Lett.* **13,** 4690–4696 (2013).

[213]. Gupta, A. K., Nisoli, C., Lammert, P. E., Crespi, V. H. & Eklund, P. C. Curvature-induced D-band Raman scattering in folded graphene. *J. Phys. Condens. Matter* **22,** 334205 (2010).

[214]. Gupta, A. K., Russin, T. J., Gutiérrez, H. R. & Eklund, P. C. Probing graphene edges via raman scattering. *ACS Nano* **3,** 45–52 (2009).

[215]. Nakada, K., Fujita, M., Dresselhaus, G. & Dresselhaus, M. Edge state in graphene ribbons: Nanometer size effect and edge shape dependence. *Physical Review B* **54,** 17954–17961 (1996).

[216]. Wang, P. *et al.* Giant optical response from graphene-plasmonic system. *ACS Nano* **6,** 6244–6249 (2012).

[217]. Holzmeister, P., Acuna, G. P., Grohmann, D. & Tinnefeld, P. Breaking the concentration limit of optical single-molecule detection. *Chem. Soc. Rev.* **43,** 1014–28 (2014).

[218]. Etchegoin, P. G. & Le Ru, E. C. A perspective on single molecule SERS: current status and future challenges. *Phys. Chem. Chem. Phys.* **10,** 6079–6089 (2008).

[219]. Kneipp, K. *et al.* Single Molecule Detection Using Surface-Enhanced Raman Scattering (SERS). *Physical Review Letters* **78,** 1667–1670 (1997).

[220]. Pieczonka, N. P. W. & Aroca, R. F. Single molecule analysis by surfaced-enhanced Raman scattering. *Chem. Soc. Rev.* **37,** 946–954 (2008).

[221]. Liu, H. *et al.* Single molecule detection from a large-scale SERS-active $Au_{79}Ag_{21}$ substrate. *Sci. Rep.* **1,** 112 (2011).

[222]. Dieringer, J. A. *et al.* Surface-enhanced Raman excitation spectroscopy of a single rhodamine 6G molecule. *J. Am. Chem. Soc.* **131,** 849–854 (2009).

[223]. Porter, M. D., Lipert, R. J., Siperko, L. M., Wang, G. & Narayanan, R. SERS as a bioassay platform: fundamentals, design, and applications. *Chem. Soc. Rev.* **37,** 1001–1011 (2008).

[224]. Le Ru, E. C., Meyer, M. & Etchegoin, P. G. Proof of single-molecule sensitivity in Surface Enhanced Raman Scattering (SERS) by means of a two-analyte technique. *J. Phys. Chem. B* **110,** 1944–1948 (2006).

[225]. Etchegoin, P. G., Le Ru, E. C. & Fainstein, A. Bi-analyte single molecule SERS technique with simultaneous spatial resolution. *Phys. Chem. Chem. Phys.* **13,** 4500–4506 (2011).

[226]. Le Ru, E. C. & Etchegoin, P. G. Single-Molecule Surface-Enhanced Raman Spectroscopy. *Annual Review of Physical Chemistry* **63,** 65–87 (2012).

[227]. Blackie, E. J., Le Ru, E. C. & Etchegoin, P. G. Single-molecule surface-enhanced raman spectroscopy of nonresonant molecules. *J. Am. Chem. Soc.* **131,** 14466–14472 (2009).

[228]. Le Ru, E. C. *et al.* A scheme for detecting every single target molecule with surface-enhanced raman spectroscopy. *Nano Lett.* **11,** 5013–5019 (2011).

[229]. Kerker, M. Electromagnetic model for surface-enhanced Raman scattering (SERS) on metal colloids. *Acc. Chem. Res.* **17,** 271–277 (1984).

[230]. Jensen, L., Aikens, C. M. & Schatz, G. C. Electronic structure methods for studying surface-enhanced Raman scattering. *Chem. Soc. Rev.* **37,** 1061–1073 (2008).

[231]. Wu, D.-Y., Li, J.-F., Ren, B. & Tian, Z.-Q. Electrochemical surface-enhanced Raman spectroscopy of nanostructures. *Chem. Soc. Rev.* **37,** 1025–1041 (2008).

[232]. Doering, W. E. & Nie, S. Single-molecule and single-nanoparticle SERS: Examining the roles of surface active sites and chemical enhancement. *J. Phys. Chem. B* **106,** 311–317 (2002).

[233]. Huang, S. *et al.* Molecular Selectivity of Graphene-Enhanced Raman Scattering. *Nano Lett.* 150402122617005 (2015). doi:10.1021/nl5045988

[234]. Ling, X. *et al.* Can graphene be used as a substrate for Raman enhancement? *Nano Lett.* **10,** 553–561 (2010).

[235]. Barros, E. B. & Dresselhaus, M. S. Theory of Raman enhancement by two-dimensional materials: Applications for graphene-enhanced Raman spectroscopy. *Phys. Rev. B - Condens. Matter Mater. Phys.* **90,** (2014).

[236]. Xu, W., Mao, N. & Zhang, J. Graphene: A platform for surface-enhanced Raman spectroscopy. *Small* **9,** 1206–1224 (2013).

[237]. Ling, X., Moura, L. G., Pimenta, M. a. & Zhang, J. Charge-transfer mechanism in graphene-enhanced Raman scattering. *J. Phys. Chem. C* **116,** 25112–25118 (2012).

[238]. Shin, Y. J. *et al.* Surface-energy engineering of graphene. *Langmuir* **26,** 3798–3802 (2010).

[239]. Alwarappan, S., Erdem, A., Liu, C. & Li, C.-Z. Probing the Electrochemical Properties of Graphene Nanosheets for Biosensing Applications. *J. Phys. Chem. C* **113,** 8853–8857 (2009).

[240]. Ling, X. *et al.* Raman enhancement effect on two-dimensional layered materials: Graphene, h-BN and MoS2. *Nano Lett.* **14,** 3033–3040 (2014).

[241]. Alivisatos, A. P. *et al.* The Brain Activity Map Project and the Challenge of Functional Connectomics. *Neuron* **74,** 970–974 (2012).

[242]. Zhang, A., Neumeyer, J. L. & Baldessarini, R. J. Recent progress in development of dopamine receptor subtype-selective agents: Potential therapeutics for neurological and psychiatric disorders. *Chem. Rev.* **107,** 274–302 (2007).

[243]. Berger, M., Gray, J. a & Roth, B. L. The expanded biology of serotonin. *Annu. Rev. Med.* **60,** 355–366 (2009).

[244]. Wise, R. A. Dopamine, learning and motivation. *Nat. Rev. Neurosci.* **5,** 483–494 (2004).

[245]. Iversen, S. D. & Iversen, L. L. Dopamine: 50 years in perspective. *Trends in Neurosciences* **30,** 188–193 (2007).

[246]. Boyer, E. W. & Shannon, M. The serotonin syndrome. *N. Engl. J. Med.* **352,** 1112–1120 (2005).

[247]. Carlsson, T. *et al.* Impact of grafted serotonin and dopamine neurons on development of L-DOPA-induced dyskinesias in parkinsonian rats is determined by the extent of dopamine neuron degeneration. *Brain* **132,** 319–335 (2009).

[248]. Kish, S. J. *et al.* Preferential loss of serotonin markers in caudate versus putamen in Parkinson's disease. *Brain* **131,** 120–131 (2008).

[249]. Politis, M. *et al.* Serotonergic neurons mediate dyskinesia side effects in Parkinson's patients with neural transplants. *Sci. Transl. Med.* **2,** 38ra46 (2010).

[250]. Esposito, E., Di Matteo, V. & Di Giovanni, G. Serotonin-dopamine interaction: an overview. *Progress in Brain Research* **172,** 3–6 (2008).

[251]. Anastassiou, C. a. *et al.* Subsecond voltammetric separation between dopamine and serotonin in the presence of ascorbate. *Anal. Chem.* **78,** 6990–6998 (2006).

[252]. Fang, H., Pajski, M. L., Ross, A. E. & Venton, B. J. Quantitation of dopamine, serotonin and adenosine content in a tissue punch from a brain slice using capillary electrophoresis with fast-scan cyclic voltammetry detection. *Anal. Methods* **5,** 2704–2711 (2013).

[253]. Patel, A. N., Tan, S. Y., Miller, T. S., MacPherson, J. V. & Unwin, P. R. Comparison and reappraisal of carbon electrodes for the voltammetric detection of dopamine. *Anal. Chem.* **85,** 11755–11764 (2013).

[254]. Liang, W., He, S. & Fang, J. Self-assembly of J-aggregate nanotubes and their applications for sensing dopamine. *Langmuir* **30,** 805–811 (2014).

[255]. Bu, Y. & Lee, S. Influence of dopamine concentration and surface coverage of Au shell on the optical properties of Au, Ag, and Ag coreAu shell nanoparticles. *ACS Appl. Mater. Interfaces* **4,** 3923–3931 (2012).

[256]. Song, P. *et al.* SERS and in situ SERS spectroelectrochemical investigations of serotonin monolayers at a silver electrode. *J. Electroanal. Chem.* **688,** 384–391 (2013).

[257]. Wang, P., Liang, O., Zhang, W., Schroeder, T. & Xie, Y. H. Ultra-sensitive graphene-plasmonic hybrid platform for label-free detection. *Adv. Mater.* **25,** 4918–4924 (2013).

[258]. Zhao, J. *et al.* Interaction of plasmon and molecular resonances for rhodamine 6G adsorbed on silver nanoparticles. *J. Am. Chem. Soc.* **129,** 7647–7656 (2007).

[259]. Michaels, A. M. & Brus, L. Ag Nanocrystal Junctions as the Site for Surface-Enhanced Raman Scattering of Single Rhodamine 6G Molecules. *J. Phys. Chem. B* **104,** 11965–11971 (2000).

[260]. Dick, L. A., Haes, A. J. & Van Duyne, R. P. Distance and Orientation Dependence of Heterogeneous Electron Transfer: A Surface-Enhanced Resonance Raman Scattering Study of Cytochrome c Bound to Carboxylic Acid Terminated Alkanethiols Adsorbed on Silver Electrodes. *J. Phys. Chem. B* **104,** 11752–11762 (2000).

[261]. Jun, H., Rong, S. S., Zhi, S. X. & Zeno, Y. Surface enhanced Raman spectroscopy of lysozyme. *Spectrochim. Acta* **51A,** 1087–1096 (1995).

[262]. Sang Kyu, K., Myung Soo, K. & Se Won, S. Surface-enhanced Raman scattering (SERS) of aromatic amino acids and their glycyl dipeptides in silver sol. *J. Raman Spectrosc.* **18,** 171–175 (1987).

[263]. Rochefort, A. & Wuest, J. D. Interaction of substituted aromatic compounds with graphene. *Langmuir* **25,** 210–215 (2009).

[264]. Persson, B. N. J., Zhao, K. & Zhang, Z. Chemical contribution to surface-enhanced Raman scattering. *Phys. Rev. Lett.* **96,** (2006).

[265]. Tu, Q., Eisen, J. & Chang, C. Surface-enhanced Raman spectroscopy study of indolic molecules adsorbed on gold colloids. *J. Biomed. Opt.* **15,** 020512 (2015).

[266]. Xu, W. *et al.* Surface enhanced Raman spectroscopy on a flat graphene surface. *Proceedings of the National Academy of Sciences* **109,** 9281–9286 (2012).

[267]. Sikirzhytski, V., Sikirzhytskaya, A. & Lednev, I. K. Multidimensional Raman spectroscopic signatures as a tool for forensic identification of body fluid traces: A review. *Appl. Spectrosc.* **65,** 1223–1232 (2011).

[268]. Sikirzhytski, V., Virkler, K. & Lednev, I. K. Discriminant analysis of Raman spectra for body fluid identification for forensic purposes. *Sensors* **10,** 2869–2884 (2010).

[269]. Kaya, M. & Volkan, M. New approach for the surface enhanced resonance Raman scattering (SERRS) detection of dopamine at picomolar (pM) levels in the presence of ascorbic acid. *Anal. Chem.* **84,** 7729–7735 (2012).

[270]. Lagutschenkov, A., Langer, J., Berden, G., Oomens, J. & Dopfer, O. Infrared spectra of protonated neurotransmitters: dopamine, *Phys. Chem. Chem. Phys*., **13**, 2815–2823 (2011).

[271]. Lagutschenkov, A., Langer, J., Berden, G., Oomens, J. & Dopfer, O. Infrared spectra of protonated neurotransmitters: Serotonin. *J. Phys. Chem. A* **114,** 13268–13276 (2010).

[272]. Le Ru, E. C. & Etchegoin, P. G. Quantifying SERS enhancements. *MRS Bull.* **38,** 631–640 (2013).

[273]. Le Ru, E. C. & Etchegoin, P. G. Rigorous justification of the |E|4 enhancement factor in Surface Enhanced Raman Spectroscopy. *Chem. Phys. Lett.* **423,** 63–66 (2006).

[274]. Le Ru, E. C., Blackie, E. J., Meyer, M. & Etchegoin, P. G. Surface Enhanced Raman Scattering Enhancement Factors: A Comprehensive Study. *J. Phys. Chem. C* **111,** 13794–13803 (2007).

[275]. Navratil, M., Mabbott, G. a & Arriaga, E. a. Chemical microscopy applied to biological systems. *Anal. Chem.* **78,** 4005–20 (2006).

[276]. Hayashi, Y. *et al.* Precision, limit of detection and range of quantitation in competitive ELISA. *Anal. Chem.* **76,** 1295–301 (2004).

[277]. Wani, T. A. Highly sensitive ultra-performance liquid chromatography–tandem mass spectrometry method for the determination of abiraterone in human plasma. *Anal. Methods* **5,** 3693 (2013).

[278]. Pitt, J. J. Principles and applications of liquid chromatography-mass spectrometry in clinical biochemistry. *Clin. Biochem. Rev.* **30,** 19–34 (2009).

[279]. Coffman, V. C. & Wu, J.-Q. Counting protein molecules using quantitative fluorescence microscopy. *Trends Biochem. Sci.* **37,** 499–506 (2012).

[280]. Tiwari, G. & Tiwari, R. Bioanalytical method validation: An updated review. *Pharm. Methods* **2,** 25 (2010).

[281]. Antonio, K. a & Schultz, Z. D. Advances in biomedical Raman microscopy. *Anal. Chem.* **86,** 30–46 (2014).

[282]. Kneipp, K., Kneipp, H., Itzkan, I., Dasari, R. R. & Feld, M. S. Surface-enhanced Raman scattering and biophysics. *J. Phys. Condens. Matter* **14,** R597–R624 (2002).

[283]. Xie, W. & Schlücker, S. Medical applications of surface-enhanced Raman scattering. *Phys. Chem. Chem. Phys.* **15,** 5329–44 (2013).

[284]. Hudson, S. D. & Chumanov, G. Bioanalytical applications of SERS (surface-enhanced Raman spectroscopy). *Anal. Bioanal. Chem.* **394,** 679–686 (2009).

[285]. Bell, S. E. J. & Sirimuthu, N. M. S. Rapid, quantitative analysis of ppm/ppb nicotine using surface-enhanced Raman scattering from polymer-encapsulated Ag nanoparticles (gel-colls). *Analyst* **129,** 1032–6 (2004).

[286]. Stuart, D. a *et al.* In vivo glucose measurement by surface-enhanced Raman spectroscopy. *Anal. Chem.* **78,** 7211–5 (2006).

[287]. Engelbrektsson, J. *et al.* Internal Standard in Surface-Enhanced Raman. *Anal. Chem.* **76,** 7391–7395 (2004).

[288]. Liu, X., Shao, Y., Tang, Y. & Yao, K.-F. Highly Uniform and Reproducible Surface Enhanced Raman Scattering on Air-stable Metallic Glassy Nanowire Array. *Sci. Rep.* **4,** 5835 (2014).

[289]. Fan, W. *et al.* Graphene oxide and shape-controlled silver nanoparticle hybrids for ultrasensitive single-particle surface-enhanced Raman scattering (SERS) sensing. *Nanoscale* **6,** 4843–51 (2014).

[290]. Sallum, L. F., Soares, F. L. F., Ardila, J. A. & Carneiro, R. L. Optimization of SERS scattering by Ag-NPs-coated filter paper for quantification of nicotinamide in a cosmetic formulation. *Talanta* **118,** 353–358 (2014).

[291]. Sackmann, M. & Materny, a. Surface enhanced Raman scattering (SERS)—a quantitative analytical tool? *J. Raman Spectrosc.* **37,** 305–310 (2006).

[292]. Vangala, K. *et al.* Sensitive carbohydrate detection using surface enhanced Raman tagging. *Anal. Chem.* **82,** 10164–10171 (2010).

[293]. Stokes, R. J. *et al.* Quantitative enhanced Raman scattering of labeled DNA from gold and silver nanoparticles. *Small* **3,** 1593–601 (2007).

[294]. Wu, Z.-S., Zhou, G.-Z., Jiang, J.-H., Shen, G.-L. & Yu, R.-Q. Gold colloid-bienzyme conjugates for glucose detection utilizing surface-enhanced Raman scattering. *Talanta* **70,** 533–9 (2006).

[295]. Wang, G. *et al.* Detection of the potential pancreatic cancer marker MUC4 in serum using surface-enhanced Raman scattering. *Anal. Chem.* **83,** 2554–61 (2011).

[296]. Jarvis, R. M. *et al.* Towards quantitatively reproducible substrates for SERS. *Analyst* **133,** 1449–1452 (2008).

[297]. Dou, X., Takama, T., Yamaguchi, Y., Yamamoto, H. & Ozaki, Y. Enzyme Immunoassay Utilizing Surface-Enhanced Raman Scattering of the Enzyme Reaction Product. *Anal. Chem.* **69,** 1492–1495 (1997).

[298]. Stranahan, S. M. & Willets, K. a. Super-resolution optical imaging of single-molecule SERS hot spots. *Nano Lett.* **10,** 3777–3784 (2010).

[299]. Wang, H., Levin, C. S. & Halas, N. J. Nanosphere arrays with controlled sub-10-nm gaps as surface-enhanced raman spectroscopy substrates. *J. Am. Chem. Soc.* **127,** 14992–3 (2005).

[300]. Willets, K. a., Stranahan, S. M. & Weber, M. L. Shedding Light on Surface-Enhanced Raman Scattering Hot Spots through Single-Molecule Super-Resolution Imaging. *J. Phys. Chem. Lett.* **3,** 1286–1294 (2012).

[301]. McMahon, J. M., Li, S., Ausman, L. K. & Schatz, G. C. Modeling the Effect of Small Gaps in Surface-Enhanced Raman Spectroscopy. *J. Phys. Chem. C* **116,** 1627–1637 (2012).

[302]. Bell, S. E. J. & Stewart, A. Quantitative SERS Methods. *Surf. Enhanc. Raman Spectrosc. Anal. Biophys. Life Sci. Appl.* 71–86 (2010). doi:10.1002/9783527632756.ch3

[303]. Harper, M. M., McKeating, K. S. & Faulds, K. Recent developments and future directions in SERS for bioanalysis. *Phys. Chem. Chem. Phys.* **15,** 5312–28 (2013).

[304]. American Cancer Society. *Colorectal Cancer Facts & Figures 2014* Atlanta, Ga: American Cancer Society; 2014.

[305]. Smith, R. a *et al.* Cancer screening in the United States, 2014: a review of current American Cancer Society guidelines and current issues in cancer screening. *CA. Cancer J. Clin.* **64,** 30–51 (2014).

[306]. Smith, R. a, Cokkinides, V. & Eyre, H. J. American Cancer Society guidelines for the early detection of cancer, 2006. *CA. Cancer J. Clin.* **56,** 11–25; quiz 49–50 (2003).

[307]. Li, Y., Qi, X., Lei, C., Yue, Q. & Zhang, S. Simultaneous SERS detection and imaging of two biomarkers on the cancer cell surface by self-assembly of branched DNA-gold nanoaggregates. *Chem. Commun.* **50,** 9907–9909 (2014).

[308]. Aksoy, C. & Severcan, F. Role of Vibrational Spectroscopy in Stem Cell Research. *Spectrosc. An Int. J.* **27,** 167–184 (2012).

[309]. Arya, S. K. & Bhansali, S. Lung cancer and its early detection using biomarker-based biosensors. *Chem. Rev.* **111,** 6783–809 (2011).

[310]. Soussi, T. p53 Antibodies in the sera of patients with various types of cancer: a review. *Cancer Res.* **60,** 1777–88 (2000).

[311]. Manoharan, R. *et al.* Raman spectroscopy and fluorescence photon migration for breast cancer diagnosis and imaging. *Photochem. Photobiol.* **67,** 15–22 (1998).

[312]. Calin, M. A., Parasca, S. V., Savastru, R., Calin, M. R. & Dontu, S. Optical techniques for the noninvasive diagnosis of skin cancer. *J. Cancer Res. Clin. Oncol.* **139,** 1083–1104 (2013).

[313]. Lim, Z.-Z. J., Li, J.-E. J., Ng, C.-T., Yung, L.-Y. L. & Bay, B.-H. Gold nanoparticles in cancer therapy. *Acta Pharmacol. Sin.* **32,** 983–90 (2011).

[314]. Alivisatos, P. The use of nanocrystals in biological detection. *Nat. Biotechnol.* **22,** 47–52 (2004).

[315]. Fortina, P. *et al.* Applications of nanoparticles to diagnostics and therapeutics in colorectal cancer. *Trends Biotechnol.* **25,** 145–52 (2007).

[316]. Lu, W. *et al.* Gold nano-popcorn-based targeted diagnosis, nanotherapy treatment, and in situ monitoring of photothermal therapy response of prostate cancer cells using surface-enhanced raman spectroscopy. *J. Am. Chem. Soc.* **132,** 18103–18114 (2010).

[317]. Vitol, E. a., Orynbayeva, Z., Friedman, G. & Gogotsi, Y. Nanoprobes for intracellular and single cell surface-enhanced Raman spectroscopy (SERS). *J. Raman Spectrosc.* **43,** 817–827 (2012).

[318]. Jokerst, J. V., Cole, A. J., Van De Sompel, D. & Gambhir, S. S. Gold nanorods for ovarian cancer detection with photoacoustic imaging and resection guidance via Raman imaging in living mice. *ACS Nano* **6,** 10366–10377 (2012).

[319]. Chourpa, I., Lei, F. H., Dubois, P., Manfait, M. & Sockalingum, G. D. Intracellular applications of analytical SERS spectroscopy and multispectral imaging. *Chem. Soc. Rev.* **37,** 993–1000 (2008).

[320]. Frank, C. J., McCreery, R. L. & Redd, D. C. Raman spectroscopy of normal and diseased human breast tissues. *Anal. Chem.* **67,** 777–783 (1995).

[321]. Lui, H., Zhao, J., McLean, D. & Zeng, H. Real-time raman spectroscopy for in vivo skin cancer diagnosis. *Cancer Res.* **72,** 2491–2500 (2012).

[322]. Abramczyk, H. & Brozek-Pluska, B. Raman imaging in biochemical and biomedical applications. Diagnosis and treatment of breast cancer. *Chem. Rev.* **113,** 5766–81 (2013).

[323]. Sha, M. Y., Xu, H., Natan, M. J. & Cromer, R. Surface-enhanced Raman scattering tags for rapid and homogeneous detection of circulating tumor cells

in the presence of human whole blood. *J. Am. Chem. Soc.* **130,** 17214–5 (2008).

[324]. Vendrell, M., Maiti, K. K., Dhaliwal, K. & Chang, Y.-T. Surface-enhanced Raman scattering in cancer detection and imaging. *Trends Biotechnol.* **31,** 249–57 (2013).

[325]. Karabacak, N. M. *et al.* Microfluidic, marker-free isolation of circulating tumor cells from blood samples. *Nat. Protoc.* **9,** 694–710 (2014).

[326]. Plaks, V., Koopman, C. D. & Werb, Z. Circulating tumor cells. *Science* **341,** 1186–8 (2013).

[327]. Ringnér, M. What is principal component analysis? *Nat. Biotechnol.* **26,** 303–4 (2008).

[328]. Das, G. *et al.* Principal component analysis based methodology to distinguish protein SERS spectra. *J. Mol. Struct.* **993,** 500–505 (2011).

[329]. Bonnier, F. & Byrne, H. J. Understanding the molecular information contained in principal component analysis of vibrational spectra of biological systems. *Analyst* **137,** 322–32 (2012).

[330]. Das, G. *et al.* Principal component analysis based methodology to distinguish protein SERS spectra. *J. Mol. Struct.* **993,** 500–505 (2011).

[331]. LaFerla, F. M., Green, K. N. & Oddo, S. Intracellular amyloid-beta in Alzheimer’s disease. *Nat. Rev. Neurosci.* **8,** 499–509 (2007).

[332]. Lee, J., Culyba, E. K., Powers, E. T. & Kelly, J. W. Amyloid-β forms fibrils by nucleated conformational conversion of oligomers. *Nat. Chem. Biol.* **7,** 602–609 (2011).

[333]. Cheng, P.-N., Liu, C., Zhao, M., Eisenberg, D. & Nowick, J. S. Amyloid β-sheet mimics that antagonize protein aggregation and reduce amyloid toxicity. *Nat. Chem.* **4,** 927–933 (2012).

[334]. Hamley, I. W. The amyloid beta peptide: A chemist’s perspective. role in Alzheimer's and fibrillization. *Chem. Rev.* **112,** 5147–5192 (2012).

[335]. Chou, I.-H. *et al.* Nanofluidic biosensing for beta-amyloid detection using surface enhanced Raman spectroscopy. *Nano Lett.* **8,** 1729–1735 (2008).

[336]. Chène, P. Inhibiting the p53-MDM2 interaction: an important target for cancer therapy. *Nat. Rev. Cancer* **3,** 102–9 (2003).

[337]. Buckmaster, R., Asphahani, F., Thein, M., Xu, J. & Zhang, M. Detection of drug-induced cellular changes using confocal Raman spectroscopy on patterned single-cell biosensors. *Analyst* **134,** 1440–6 (2009).

[338]. Palonpon, A. F. *et al.* Raman and SERS microscopy for molecular imaging of live cells. *Nat. Protoc.* **8,** 677–92 (2013).

[339]. Movasaghi, Z., Rehman, S. & Rehman, I. U. Raman Spectroscopy of Biological Tissues. *Appl. Spectrosc. Rev.* **42,** 493–541 (2007).

[340]. Surmacki, J., Musial, J., Kordek, R. & Abramczyk, H. Raman imaging at biological interfaces: applications in breast cancer diagnosis. *Mol. Cancer* **12,** 48 (2013).

[341]. Nemecek, D., Stepanek, J. & Thomas, G. J. *Raman spectroscopy of proteins and nucleoproteins. Current protocols in protein science / editorial board, John E. Coligan ... [et al.]* **Chapter 17,** (2013).

[342]. Chaffer, C. L. & Weinberg, R. A. A perspective on cancer cell metastasis. *Science* **331,** 1559–1564 (2011).

[343]. Yan, Z. Q. & Zhang, W. The development of graphene-based devices for cell biology research. *Front. Mater. Sci.* **8,** 107–122 (2014).

[344]. Liu, a Q., Huang, H. J., Chin, L. K., Yu, Y. F. & Li, X. C. Label-free detection with micro optical fluidic systems (MOFS): a review. *Anal. Bioanal. Chem.* **391,** 2443–52 (2008).

[345]. Motz, J. T. *et al.* Optical fiber probe for biomedical Raman spectroscopy. *Appl. Opt.* **43,** 542–554 (2004).

[346]. Andrade, G. F. S., Fan, M. & Brolo, A. G. Multilayer silver nanoparticles-modified optical fiber tip for high performance SERS remote sensing. *Biosens. Bioelectron.* **25,** 2270–2275 (2010).

[347]. Gessner, R. *et al.* The application of a SERS fiber probe for the investigation of sensitive biological samples. *Analyst* **129,** 1193–1199 (2004).